Summer 8-2021

Voltage-Controlled Magnetization in Chromia-based Magnetic Heterostructures

William Echtenkamp
University of Nebraska-Lincoln, will.echtenkamp@huskers.unl.edu

Echtenkamp, William, "Voltage-Controlled Magnetization in Chromia-based Magnetic Heterostructures" (2021). *Theses, Dissertations, and Student Research: Department of Physics and Astronomy*. 54.
https://digitalcommons.unl.edu/physicsdiss/54

VOLTAGE-CONTROLLED MAGNETIZATION IN CHROMIA-BASED MAGNETIC HETEROSTRUCTURES

by

William Echtenkamp

A DISSERTATION

Presented to the Faculty of

The Graduate College at the University of Nebraska

In Partial Fulfillment of Requirements

For the Degree of Doctor of Philosophy

Major: Physics and Astronomy

Under the Supervision of Professor Christian Binek

Lincoln, Nebraska

August 2021

VOLTAGE-CONTROLLED MAGNETIZATION IN CHROMIA-BASED MAGNETIC HETEROSTRUCTURES

William Echtenkamp, Ph.D.

University of Nebraska, 2021

Advisor: Christian Binek

Spin-electronics or “spintronics” promises a new generation of low-power, high-speed, non-volatile memory and logic devices. Almost all existing and planned spintronic devices operate on controlling magnetization, preferably by electrical means alone. In this context, Cr_2O_3 (chromia) based heterostructures have emerged as a promising candidate. Chromia is magnetoelectric, which provides a direct coupling between an applied electric field and an induced magnetic moment. Moreover, chromia has an uncompensated moment at its interface, known as boundary magnetization. This magnetization is closely associated with the antiferromagnetic domain state of the chromia which can be electrically switched. The boundary magnetization can therefore be used as a logical bit in spintronic devices.

While the equilibrium boundary magnetization of chromia is strictly tied to its domain state, non-equilibrium states may be created. For example, in the presence of an adjacent ferromagnet, exchange coupling at the interface may stabilize the interfacial domain state of the chromia against the rotation of the bulk of the crystal when it is subjected to critical magnetoelectrical switching fields. This results in an

antiferromagnetic interface in a nonequilibrium state which is incommensurate with the underlying bulk. Upon magnetically cycling the ferromagnet, the antiferromagnet then relaxes, which in turn is reflected in the exchange bias of the ferromagnetic hysteresis loop. In other cases, the interfacial exchange locks the antiferromagnetic interface to rotate along with the ferromagnet. This causes a competition between the exchange energy at the interface and the anisotropy energy of the crystal. At the crossover point between these two mechanisms there occurs a simultaneous disappearance of exchange bias with a more than twofold increase in coercivity of the ferromagnetic hysteresis loop.

Due to its relatively high Néel temperature, chromia has the advantage of potential operation at room temperature, nevertheless, further increasing the Néel temperature would provide more flexibility in applications. It is shown that by boron doping, the Néel temperature of chromia can be controllably tuned from the undoped temperature of $T_N = 307$ K, up to at least 400 K. In addition, boron doped chromia exhibits voltage-controlled and non-volatile Néel vector reorientation in the absence of an applied magnetic field, further expanding its functionality.

Acknowledgements

I would like to express my sincere gratitude to my advisor Professor Christian Binek. With his deep knowledge of the field, he has guided and supported me though every step in my graduate career. It has been a great pleasure to be a part of his group.

I would also like to thank the rest of my committee: Professor Shireen Adenwalla, Professor Alexey Kovalev, and Professor Jeffrey Shield for their invaluable time invested in supporting my Ph.D work and their critical reading of this dissertation.

Furthermore, I would like to express my appreciation to my group members throughout the years: Dr. Ather Mahmood, Prakash Giri, Syed Qamar Abbas Shah, Dr. Michael Street, Dr. Junlei Wang, Dr. Xi He, Dr. Srinivas Polisetty. and Dr. Tathagata Mukherjee, all of whom were invaluable in their support and hard work. I would also like to thank Dr. Uday Singh, Christopher Keck, Dr. Ning Wu, Dr. Shi Cao for their collaboration.

I would like to thank the staff of the NCMN central facilities especially Dr. Steve Michalski, Dr. Shah Vallopilly, Dr. Andrei Sokolov, and Dr. Lanping Yue, all of whom enabled the fabrication and characterization used throughout this work.

For their emotional support and guidance throughout the years, thank you to my parents Lee and Shirley Echtenkamp and all of my brothers and sisters. You all made me who I am.

Lastly, I would like to thank my wife Jessica Brauer Echtenkamp for everything.

Table of Contents

List of Figures

Chapter 1: Introduction

Modern electronics utilizing integrated circuits, microprocessors, microcontrollers, random access memory, digital logic circuits and the like, largely rely on the technology of the complementary metal-oxide-semiconductor (CMOS). CMOS technology has increased computing efficiency over the past five decades by shrinking the circuit area, lowering the supply voltage, and reducing individual transistor cost. These trends are characterized by two well-known laws, the first of which is Moore's law, which states that the number of transistors on integrated circuits approximately doubles every two years. The second is Dennard's trend which states that as transistors get smaller, their power density remains constant; that is, both the current and voltage required decrease as area decreases. However, in the last 15 years, scaling has deviated from Dennard's trend. The cause of this breakdown is explained by the minimum gate voltage swing necessary to switch a conventional transistor from an "on" state to an "off" state.[1] One result of a minimum voltage requirement is that any further increase of the clock frequency for CMOS-based devices would result in unsupportable increases in power dissipation and heat generation. As the fundamental limitations of CMOS-based devices become more restrictive to progress of the microelectronics industry, new solutions are being sought which reduce area, power consumption and increase processing speed for the next generation of electronic devices.

The field of spintronics offers many potential CMOS replacements or supplements which have advantages over the electronics of today. One such suggestion involves using a tunneling magnetoresistance device in conjunction with a magnetoelectric film to create a “magnetoelectric magnetic tunnel junction” (ME-MTJ).[2] It has been shown that such a device could serve as the fundamental building block for a wide variety of low energy, non-volatile memory and logic devices.[3] An understanding of the operation of such a device will provide a background to the new physics presented in this thesis. As such, chapter 1 is organized to break down the critical physics of each part of the ME-MTJ. Starting with a background into spintronics, tunneling magnetoresistance is introduced in section 1.1. Exchange bias, an emergent magnetic anisotropy which arises from the interaction between the magnetoelectric and magnetic tunnel junction portions of the ME-MTJ, is introduced in section 1.2. The magnetoelectric effect which of course provides the functionality of the device is introduced in 1.3. Boundary magnetization is a symmetry driven consequence of the magnetoelectric effect in antiferromagnets. The boundary magnetization is the underlying physical mechanism which causes the exchange bias to manifest in the ME-MTJ and it is addressed in section 1.4. Voltage control of exchange bias is the confluence of effects caused by the magnetoelectric effect, boundary magnetization and exchange bias. It is the mechanism that will allow the electric control of magnetization in the magnetic tunnel junction. Voltage control of exchange bias is discussed in section 1.5. Finally, all this is put together in section 1.6 which will briefly explain the operation of the ME-MTJ. After this introduction, the body of the thesis should be well motivated and the reader will be familiar with much of the underlying physics.

Chapters 2 and 3 outline the sample fabrication and measurement techniques used in this thesis. While this will be useful to give the reader a deeper understanding of the work and is essential if the goal is to reproduce any results, these chapters can be considered optional for the understanding of the rest of the thesis.

The body of the thesis, in large part, is dedicated to new physics which has been discovered in the simple ferromagnetic/antiferromagnetic magnetoelectric heterostructures which can be considered the foundation of the ME-MTJ. Chapter 4 introduces a magnetic aging effect known as exchange bias training. Although not a new effect, in the heterostructures under study here, novel, previously unknown properties manifest. In particular, the exchange bias training examined here is electrically controllable and can be turned off or on by setting the domain state of the antiferromagnet with voltage. In addition, contrary to most other instances of exchange bias training, in these heterostructures the training can serve to increase the magnitude of the exchange bias. The training itself is modeled with a discretized version of the Landau-Khalatnikov equation and the underlying mechanisms are explained. The ability to set the state of a device anywhere along a continuum between two states, as demonstrated here, can add functionality to spintronic devices. For example, the gradual switching between levels is the key to all neuromorphic computing applications.[4]

In Chapter 5, the abrupt disappearance of exchange bias with a simultaneous increase in coercivity which is sometimes observed in these heterostructures at a particular temperature is explained. This behavior is interpreted as switchover in behavior resulting from a competition between the anisotropy of the antiferromagnet and the exchange field between the ferromagnet and antiferromagnet. This behavior is modeled in a Meiklejohn-Bean type approach which not only accounts for the jumps in exchange bias and coercivity, but also predicts the asymmetric evolution of the loop and the jump in the observed saturation magnetizations, both of which are also observed.

While the ME-MTJ looks like a promising technology, there are a few aspects of it which would need to be improved for any commercial applications. In chapter 6, the critical temperature under which the ME-MTJ can function is increased, allowing for integration into today's technology at and above room temperature without need for strict temperature control. This is done by doping the functional layer of the device with boron.

Having addressed some of the challenges intrinsic to the ME-MTJ, a new device structure with reduced complexity as compared to the ME-MTJ is demonstrated in chapter 7. This new device structure utilizes boron doping and does not rely on exchange bias, removing the associated difficulties. The operating principles of such a device are discussed including a new switching mechanism.

Finally, in chapter 8 one open question is addressed and the key results are summarized.

1.1 Spintronics

Spintronics is a conglomeration of emerging and existing technologies which could replace or supplement CMOS in the future. Spintronics is a portmanteau of "spin" and "electronics", the name is chosen because unlike conventional electronics which exploits the charge of the electron as its functional mechanism, spintronics uses the spin. In charge-based digital devices, to switch from a logical '1' to '0' some charge must be transferred because it is that charge which determines the state of the bit, thus some resistive losses are inevitable. On the other hand, by using a quantum mechanical spin, one can take advantage of the pair of eigenstates a spin can occupy in an external magnetic field to encode the logical '1' or '0'. Moreover, the minimum energy consumed to switch a spin from up to down is of the order of $g\mu_B B$, where g is the Landé factor, μ_B is the Bohr magneton, and B is an external magnetic field.[5] While this minimum energy is not zero, it is expected spintronic-based devices will have a smaller energy requirements than conventional electronics. While single electron spintronics have made some remarkable advances in the past few years,[6, 7] efforts for scalable energy-efficient devices for the near future have focused on collective state switching devices.[8, 9] Manipatruni et. al. recently restated the concept of a beyond-CMOS switch as a collective switch that reverses a material's order parameter.[8] In particular the following figure of merit was proposed: $\lambda = E_{SW}/\Delta E(\eta)$. Here $\Delta E(\eta)$ is the energy barrier between states, η is the order parameter and E_{SW} is the total energy dissipated in switching. λ therefore, functions as a measure of switching efficiency. Lower values of λ enable switches to operate at lower energy for a given energy barrier. The energy barrier is set by the stability of the logic state needed and will depend on application. Disparate candidate spintronic technologies can then be fairly assessed by comparing their λ values. For example, the lower limit for capacitive, magnetoelectric and ferroelectric spintronic devices is $\lambda > 2$ while for spin torque devices $\lambda > 10^4$.[8] In addition to highly efficient switching, the energy barrier between the states can be reduced, while highly scaled CMOS transistors can operate at $\sim 10^4 k_B T$, it is estimated that for practical switching speeds and retention times $\sim 100\ k_B T$ will suffice, drastically reducing the total energy used.[8] Candidate spintronic devices are expected to be able to achieve ultralow switching energy (1 aJ per switch) at ultralow switching voltages (< 100 mV).[8]

Unsurprisingly the foundations of spintronics were built using ferromagnetic materials. The defining characteristic of ferromagnets is the presence of a spontaneous magnetization. This magnetization can be directly manipulated using an external magnetic field, and has measurable, quantifiable effects on the spin state of an electric current passing through it (and vice versa). Thus, ferromagnets provide a rich sandbox in which to begin to understand spintronics. The beginnings of spintronics can be traced back to the pioneering experiments of Mott, studying the conduction of electrons in metals.[10] Mott described the conduction of electrons as the sum of two parts; that of spin up and spin down electrons. It was shown that at sufficiently low temperatures the electrons in each group do not interact and thus can be thought of as independent. Moreover, in ferromagnetic materials the conduction of each component depends on whether the spin of the electron is either parallel or anti-parallel to the magnetization of the material through which it traverses, and therefore can be manipulated by setting the magnetization by use of an external magnetic field.

The so-called "two-current model" of Mott, eventually became the physical basis of one of the first spintronic device, the spin valve. The spin valve is typically composed of two ferromagnetic electrodes, typically separated by some non-magnetic tunnel barrier. Typically, in a spin valve the magnetization of one of the ferromagnetic layers is pinned by exchange coupling with an adjacent antiferromagnetic layer, whereas the other is free to rotate with the application of an external magnetic field. As explained by Maekawa and Gäfvert the conductance of such a device can be understood in the following way:[11]

When the magnetizations of both ferromagnetic electrodes A and B are parallel, and assuming the spin polarization of the electrons are conserved during tunneling, the conductance $G_{\uparrow\uparrow}$, is given by

$$G_{\uparrow\uparrow} = \alpha(\rho_+^A \rho_+^B + \rho_-^A \rho_-^B) \tag{1.1.1}$$

where $\rho_{+}^{A,B}$and $\rho_{-}^{A,B}$are the tunneling density of states of the majority and minority spin electrons in metals A and B and α is some constant. Likewise, if the magnetic moment of electrode A is reversed then the conductance $G_{\uparrow\downarrow}$ is given by

$$G_{\uparrow\downarrow} = \alpha(\rho_{+}^{A}\rho_{-}^{B} + \rho_{-}^{A}\rho_{+}^{B}) \tag{1.1.2}$$

The relative conductance is defined as

$$\frac{\Delta G}{G} = \frac{G_{\uparrow\uparrow} - G_{\uparrow\downarrow}}{(G_{\uparrow\uparrow} + G_{\uparrow\downarrow})/2} = \frac{2(R_{\uparrow\downarrow} - R_{\uparrow\uparrow})}{(R_{\uparrow\downarrow} + R_{\uparrow\uparrow})} \tag{1.1.3}$$

Where the more commonly measured resistance is given by $R \equiv 1/G$. Therefore, it is seen that the resistance of a spin valve composed of a ferromagnetic bilayer can be manipulated by changing the relative orientation of magnetizations of the layers. Since the magnetizations of each ferromagnet can be preserved even in the absence of a magnetic field, the state of the spin valve device is non-volatile and can be useful in, for example, memory technologies.

1.2 Exchange Bias

When a ferromagnet material is in sufficiently close proximity to an adjacent magnetically ordered material, the electrons of the ferromagnet are subject to the quantum exchange interaction and an emergent type of magnetic anisotropy called exchange bias may arise. Exchange bias is the unidirectional shift along the applied field axis of a ferromagnetic hysteresis loop. Exchange bias requires a soft ferromagnetic material (here soft (hard) refers to the relatively high (low) magnetic responsiveness to an external field) and a hard magnetically ordered material. The different responsiveness of the materials allows the soft material to reverse in an external magnetic field while the hard material remains fixed. For exchange bias to arise the two materials must be in intimate contact to allow for quantum exchange interaction to act. The geometry most common for exchange bias systems is that of a thin film heterostructure of a few nanometers thickness. In these systems no part of the heterostructure is outside of the adjacent film by more than a few nanometers which allows quantum effects to manifest.[12, 13] Another common geometry which allows this is a soft magnetic nano-core inside a hard magnetic shell (or vice versa).[14-19] In either geometry, the volume of the soft ferromagnetic material within the range of exchange interaction of the interface is significant. Finally, there must be a temperature at which both the soft and hard layer are simultaneously magnetically ordered.

Exchange bias was first discovered by Meiklejohn and Bean in 1956 while studying fine particles of cobalt within a cobalt oxide shell.[14, 19] The cobalt oxide used as a hard magnetic layer in this experiment is antiferromagnetic and since then ferromagnetic-antiferromagnetic exchange bias systems have been the most common type of exchange bias heterostructures. These structures are favored due to improved control over the interface and favorable properties for creating devices such as magnetic recording media and read/write heads.[12] The discovery of giant magnetoresistance (GMR) has triggered a renewed interest in exchange bias phenomenon. GMR arises in alternately layered ferromagnetic/non-ferromagnetic film stacks. It has been found that when the nearest neighbor ferromagnetic films are oppositely magnetized the electrical resistance of the film is higher than when those films are magnetized in the same direction.[20, 21] Exchange bias enables the control of the magnetization of part of the structure via exchange, thus allowing operation of spin valves at low fields.[13]

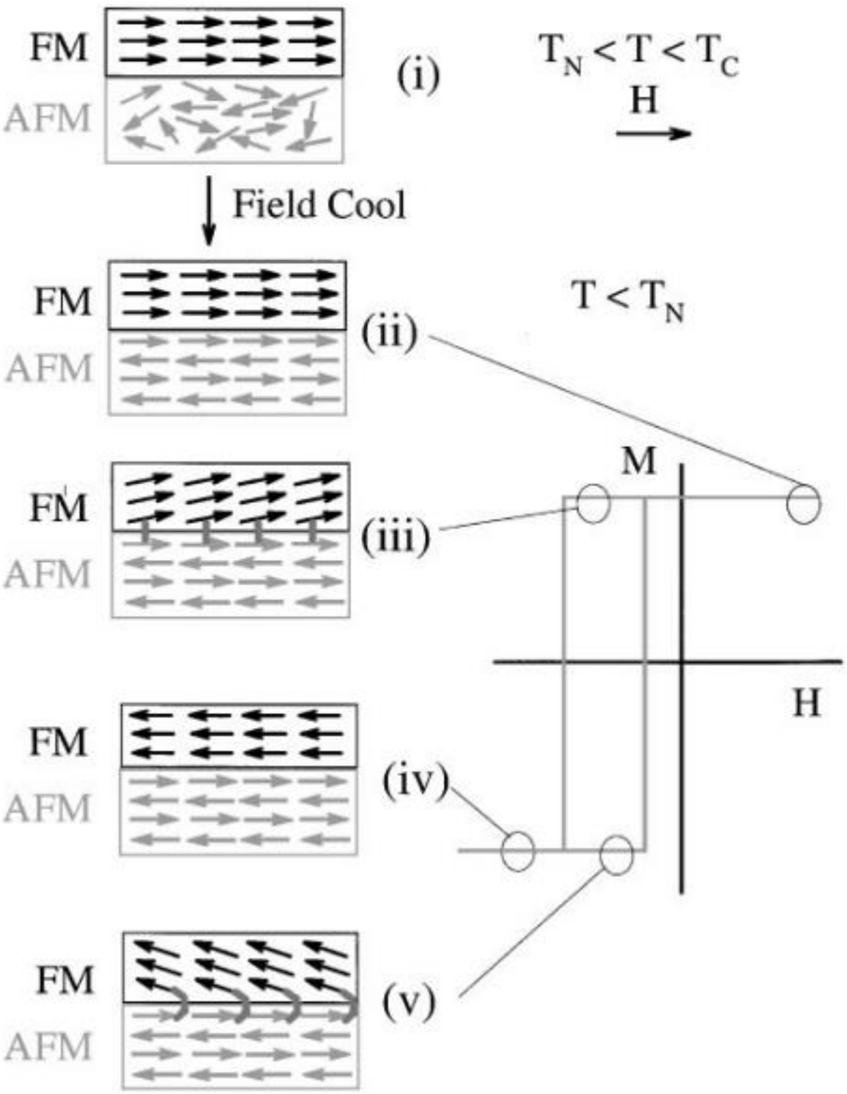

Figure 1.2.1: Spin Configurations of a ferromagnetic/antiferromagnetic heterostructures (i) above the Néel temperature and (ii)-(v) below the Néel temperature at various stages of applied field $\vec{H}$.[12]

The intuitive picture behind exchange bias is explained by Nogués and Schuller and is shown in Figure 1.2.1.[12] At a temperature above the Néel temperature of the antiferromagnet, but below the Curie temperature of the ferromagnet, an applied magnetic field will align the moments of the ferromagnetic film (i). If the temperature is lowered while the ferromagnet is in the saturated state, when the Néel temperature is crossed the antiferromagnet will begin to order. The antiferromagnetic spins at the interface of the ferromagnet will align according to the magnetization of the ferromagnetic layer and the exchange between the ferromagnet and antiferromagnetic spins, the remaining bulk of the antiferromagnet will follow this order to produce a net zero magnetization (ii). At a fixed temperature, a reversed magnetic field will reverse the ferromagnetic layer but the exchange between the antiferromagnetic spins and the ferromagnet will induce a torque which reinforces the magnetic configuration of the system, requiring a larger in magnitude magnetic field to change from state (iii) to state (iv). After reversing the direction of the magnetic field sweep, this same torque between the ferromagnet and antiferromagnet will allow the ferromagnet in a disfavored magnetic configuration (v) to return to the favored magnetic configuration (ii) at a lower applied magnetic field.

Meiklejohn and Bean were able to simply formalize this intuitive picture by considering the free energy of a magnet in an external field.[14, 19] The free energy equation for a simple magnet is

$$F = -mB\cos(\beta) + K_{FM}\sin^2(\beta) \tag{1.2.1}$$

Here, a single-domain ferromagnetic particle with uniaxial anisotropy of $K_{FM}\sin^2(\beta)$ and total magnetic moment $\boldsymbol{m}$ is considered where β is the angle between the easy direction of magnetization and the direction of magnetization and $\boldsymbol{B}$ is the magnetic field in the direction of the easy axis of magnetization. A unidirectional anisotropy caused by the exchange interaction across the interface can be introduced to the free energy as

$$F = -mB\cos(\beta) + K_{FM}\sin^2(\beta) - J\cos(\beta) \tag{1.2.2}$$

Such an anisotropy term could be caused as above by an adjacent antiferromagnet. The free energy can then be rearranged as

$$F = -m(B - J/m)\cos(\beta) + K_{FM}\sin^2(\beta) \tag{1.2.3}$$

It is then immediately obvious that the system will behave identically as the previous case, just with an effective field shifted in one direction. This of course leads to the shifted hysteresis loops as shown in Figure 1.2.1.

Although this simple phenomenological model captures the essentials of exchange bias, quantitatively the model falls short in many ways. For example, this model will typically overestimate the exchange bias effect by two orders of magnitude.[22] Moreover, using only the Meiklejohn Bean model one would expect negative exchange bias (with respect to the set field), uncompensated interfaces having the largest exchange bias (as opposed to compensated), and the roughness of compensated interfaces having the effect of increasing exchange bias.[23] None of these expectations are universally met. In part, the trouble arises from the fact that the model does not take into account roughness between interfaces, or domain wall formation both of which do play a large role in exchange bias physics. While it could be argued that other models more accurately capture the underlying physics of exchange bias, the Meiklejohn Bean model remains popular, especially among experimentalist, for its simplicity and ability to model the most important aspects of exchange bias phenomenon, namely how the interface magnetizations interact through exchange to cause the ferromagnetic loop shift.

1.3 Magnetoelectric Effect

The magnetoelectric effect is a coupling between an applied electric field and the magnetization in a medium or an applied magnetic field and the electric polarization in a medium, known as the electrically induced magnetoelectric effect and the magnetically induced magnetoelectric effect respectively. The most straight forward way to understand the origins of the magnetoelectric effect is to examine an expansion of the free energy of a material with respect to the electric ($\vec{E}$) and magnetic fields ($\vec{H}$).[24-26]

$$F(\vec{E},\vec{H}) = F_0 - P_{0i}E_i - M_{0i}H_i \\ - \frac{1}{2}\epsilon_0\varepsilon_{ij}E_iE_j - \frac{1}{2}\mu_0\mu_{ij}H_iH_j - \alpha_{ij}E_iH_j \\ - \frac{1}{2}\mathrm{\beta_{ijk}}E_iH_jH_k - \frac{1}{2}\gamma_{ijk}H_iE_jE_k + \cdots \tag{1.4.1}$$

The electric polarization of the material is given by the thermodynamic definition

$$P_i(\vec{E},\vec{H}) = -\frac{\partial F}{\partial E_i} \\ = P_{0i} + \epsilon_0\varepsilon_{ij}E_j + \alpha_{ij}H_j + \frac{1}{2}\beta_{ijk}H_jH_k + \frac{1}{2}\gamma_{ijk}H_jE_k \\ + \cdots \tag{1.4.2}$$

While the magnetization of the material is given by

$$M_i(\vec{E},\vec{H}) = \frac{\partial F}{\partial H_i} \\ = M_{0i} + \mu_0\mu_{ij}H_j + \alpha_{ij}E_j + \beta_{ijk}E_jH_k + \frac{1}{2}\gamma_{ijk}E_jE_k \\ + \cdots \tag{1.4.3}$$

Where M_0 and P_0 are the spontaneous magnetization and polarization, μ_0 and ϵ_0 are the permeability and permittivity of free space, μ and ε are the magnetic and electric susceptibilities, α is the linear magnetoelectric susceptibility and β and γ are the higher order magnetoelectric susceptibilities. This expansion shows that the magnetization and the polarization are at least potentially cross correlated with the electric and magnetic fields.

Landau and Lifshitz were the first to show that the magnetoelectric effect is intimately connected with the magnetic symmetry of a substance. It was pointed out that the magnetoelectric effect may arise in spin-oriented materials, but will only be possible for certain magnetic symmetry classes.[27] From equation 1.4.1, the magnetoelectric contribution to the free energy in a crystal, in lowest order is $F_{ME} = -\alpha_{ij} E_i H_j$. Neumann's principle states that no symmetry can manifest itself in the form of a property tensor which does not already exist in the symmetry of the crystal which exhibits the property.[28] This principle can be applied to narrow the crystal symmetry classes which can support a linear magnetoelectric response. If it is assumed that the magnetoelectric crystal is symmetric under spatial inversion, then α must also be invariant under spatial inversion because of Neumann's principle. But $\boldsymbol{E}$ is odd under spatial inversion while $\boldsymbol{H}$ is even. Since the free energy is a scalar and therefore unaffected by spatial inversion, by assuming the linear magnetoelectric has inversion symmetry the contradiction is reached that each side of the equation $F_{ME} = -\alpha_{ij} E_i H_j$ has a different symmetry, thus the linear magnetoelectric must have broken inversion symmetry to avoid this contradiction. Likewise, assuming the magnetoelectric have time inversion symmetry leads similarly to a contradiction, since $\boldsymbol{E}$ is symmetric under time inversion, while $\boldsymbol{H}$ is antisymmetric, therefore the linear magnetoelectric crystal must have time inversion symmetry broken. Due to the symmetry requirements it is found that the linear magnetoelectric effect can exist in only 58 of the 122 magnetic point groups.[29] Dzyaloshinski first predicted that crystalline antiferromagnet chromia (Cr_2O_3) has the appropriate symmetries and thus should display a magnetoelectric effect.[30] Shortly thereafter, electric field induced magnetization in chromia[31] and magnetic field induced polarization[32] were experimentally confirmed.

A considerable amount of excitement followed the experimental confirmation of the magnetoelectric effect in chromia, but it was soon realized that the small magnitude of the linear magnetoelectric susceptibility in chromia is too small to be directly useful for devices. At its maximum the magnetoelectric susceptibility of chromia was shown be a mere 4.13 ps/m, which yields the same magnetic response as reversing only five of every 10^6 spins under an electric field of 10^6 V/m.[24] It was shown more generally that the magnetoelectric susceptibility for any crystal has an upper bound given by,[33]

$$\alpha_{ij}^2 < \epsilon_0 \varepsilon_{ij} \mu_0 \mu_{ij} \tag{1.4.4}$$

Therefore, to have a much larger magnetoelectric response it is expected that a material must at least have a high electric susceptibility (for example a ferroelectric), or a high magnetic susceptibility (for example a ferromagnet), or ideally both. In addition, these susceptibilities should be simultaneously high at one single temperature. There are a relatively small number of intrinsically multiferroic materials due to the simultaneous requirements for two order parameters and of those that do exist many either have weak coupling between the mechanisms of magnetism and ferroelectricity or a low critical temperature for one or more of the orderings.

In light of these limits, the intrinsic magnetoelectric effect in single phase materials is often not as promising a route as alternatives. One alternative is engineering a multiferroic heterostructures using both magnetic and ferroelectric material, by coupling the order parameters of two dissimilar materials across an interface, the net result can be a large magnetoelectric effect. Likewise, a large magnetoelectric effect can be accomplished by combining, for example, a magnetostrictive element with a piezoelastic element. An applied magnetic field causes a strain in the magnetostrictive layer which is passed on to the piezoelastic layer, resulting in an electric polarization.[24, 34] Such composite systems have the advantage that each individual element can be tailored to optimize the desired properties of the device, but at the expense of increase complexity[34-36].

Recently, the magnetoelectric effect has been harnessed to give electric control of exchange bias in a composite system of magnetoelectric chromia coupled to an adjacent ferromagnetic layer.[37] In this system the desired magnetoelectric properties are all contained within a pure chromia layer. An applied electric field writes the domain state of the chromia while the ferromagnetic layer makes it easy to read this state. The operation of such devices relies on the symmetry driven interface properties of antiferromagnetic magnetoelectrics.

1.4 Boundary Magnetization

Landau and Lifshitz identified that the symmetry properties of certain magnetic crystals gave rise to a magnetization in response to an applied electric field, such crystals were called magnetoelectric. It was later realized that these same symmetry properties also created a magnetization at the boundary of an antiferromagnetic magnetoelectric. The boundary of the crystal can be characterized by the polar vector $\vec{n}$, which reduces the symmetry in a similar way as an applied electric field. As a result, a roughness insensitive net magnetic moment arises at the interface of a magnetoelectric antiferromagnet.[38, 39] It was further shown that all mechanisms which produce the linear magnetoelectric effect in the bulk can also generate boundary magnetization, including modification of the g tensor, the single-ion anisotropy tensor, the intrasublattice symmetric coupling, and the Dzyaloshinskii-Moriya interaction induced by $\vec{E}$ or $\vec{n}$. Of these mechanisms the boundary magnetization may be particularly large if the boundary breaks the equivalence of the antiferromagnetic sublattices, potentially creating magnetizations up to a few Bohr magnetons per boundary site.

The boundary magnetization, in the absence of any external forces, is strictly tied to the antiferromagnetic domain state. In single crystalline chromia there are two degenerate stable antiferromagnetic ground states which are related by a 180˚ rotation. These two domain states have opposite magnetoelectric susceptibilities and thus surface magnetizations of opposite sign. If the degeneracy between the states is not lifted, it can be expected that each type of domain will form in roughly equal parts. However, the degeneracy can be lifted by a process called magnetoelectric annealing.[31, 40, 41] In magnetoelectric annealing, the temperature of the chromia is elevated above its Néel temperature (307 K) where there is no magnetic order, then a particular electric and magnetic field is applied. With the fields applied the temperature is lowered to below the Néel temperature. Magnetoelectric annealing allows for preferential selection of one domain type by exploiting the free energy gain $\Delta F = 2\alpha EH$ which manifests below the Néel temperature of the chromia. As the crystal crosses the Néel temperature, the applied fields lift the degeneracy between the two domain states just as magnetic order begins to set in, causing one domain to form preferentially. With sufficiently high electric and magnetic fields a single domain state is (very nearly) achieved by using this annealing procedure.

One of the first direct observations of the symmetry driven antiferromagnetic boundary magnetization was taken on chromia.[42] Spatially resolved observations of the boundary magnetization was imaged with photo-emission electron microcopy (PEEM) combined with x-ray magnetic circular dichroism (XMCD). The XMCD-PEEM method is a surface sensitive detection of the projection of the magnetization on the x-ray polarization direction. Thus images of the boundary magnetization can be formed with a few tens of nanometers of lateral resolution.

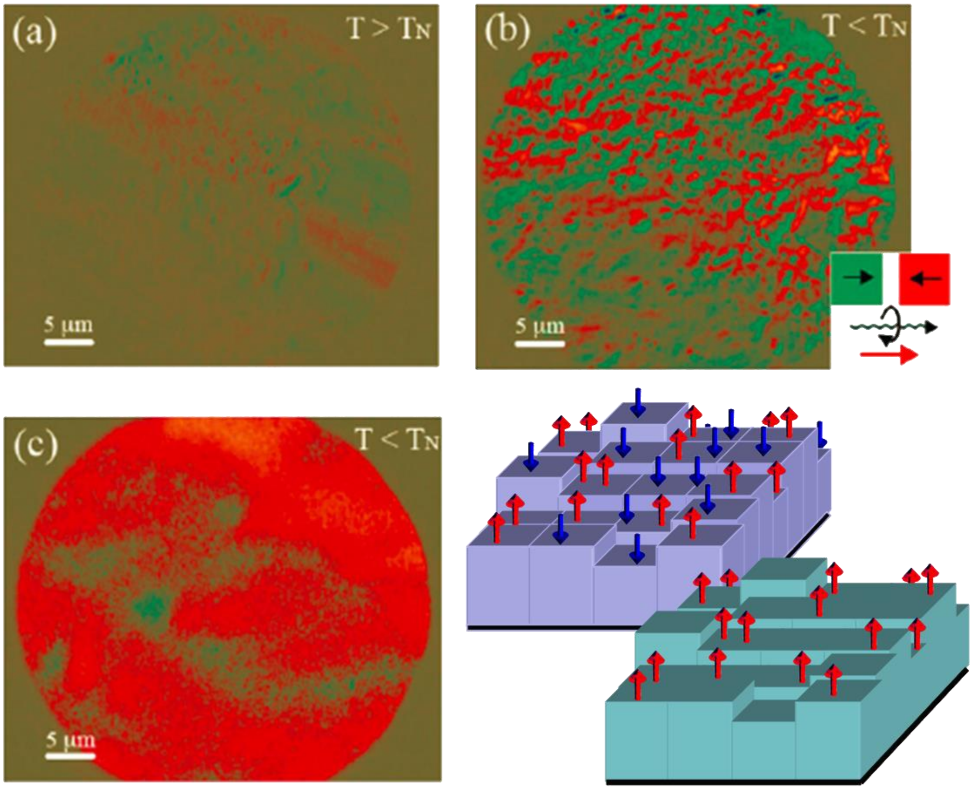

Figure 1.4.1: (a)-(c) The surface of chromia imaged by XMCD-PEEM. (a) At $T>T_N$ there is no contrast. (b) After zero field cooling both types of boundary magnetization is visible. (c) After magnetoelectric annealing only one type of boundary magnetization is visible. (d) Diagram of the roughness insensitive boundary magnetization in a (i) multidomain state, (ii) single domain state.

XMCD-PEEM images were taken at various temperatures and after various magnetoelectric annealing conditions. The results are shown in Figure 1.4.1. In panel (a), the image was taken at 584 K which is above the Néel temperature. Since no long-range magnetic order is present, no boundary magnetization is either, this results in no contrast in the XMCD-PEEM image. In panel (b) the image was taken below the Néel temperature after zero-field cooling from above the Néel temperature. Since the degeneracy between the two ground states of chromia was not lifted during the annealing process, both types of antiferromagnetic domains manifest as evidenced by the contrast between regions in the image. The inset in panel (b) shows that in the green areas the projection of the boundary magnetization along the x-ray polarization is parallel and the red areas are regions of antiparallel orientation. Panel (c) shows an image of the chromia below the Néel temperature after a magnetoelectric annealing process. The applied electric field was 13.3 kV/mm while the magnetic field was provided by the earth. After this annealing process, a uniform boundary magnetization forms according to the relative signs of the annealing fields.

Since the initial observations, the boundary magnetization in chromia has been imaged using single-spin magnetic imaging using a nanoscale nitrogen vacancy technique which has produced, sub-100 nm spatially resolved images.[43] In addition, zero-offset Hall magnetometry has measured the spin Hall magnetoresistance the boundary magnetization causes in an adjacent Pt film, giving a precise readout of the averaged relative boundary magnetization.[43-45]

1.5 Voltage-Controlled Exchange Bias

Due to its magnetoelectric nature, a particular antiferromagnetic domain state for chromia can be selected by annealing in the presence of electric and magnetic fields. Moreover, any particular domain state corresponds to a particular boundary magnetization. For chromia, the boundary magnetization along the (0001) interface is oriented maximally out of the plane. It was first demonstrated that by exchange coupling a perpendicular ferromagnet to this chromia interface the resulting ferromagnetic loop is exchange biased after a magnetoelectric annealing procedure.[46] By reversing the direction of the electric field during annealing, while maintaining the direction of the magnetic field, the subsequent exchange bias is reversed, thus demonstrating voltage control of exchange bias.

Because this protocol requires cooling of the sample from above to below the Néel temperature, the term magnetoelectric control rather than voltage control of exchange bias was coined.

As the temperature is further reduced below the Néel temperature, the antiferromagnetic order of the chromia becomes more stabilized. Nevertheless, the magnetoelectric contribution to the free energy remains, so by applying simultaneous electric and magnetic field one antiferromagnetic domain is energetically favored while the other is disfavored. If the electric and magnetic fields are increased past a certain threshold (at a given temperature) the increase in magnetoelectric energy will overcome the crystal anisotropy and the entire spin structure of the chromia will reverse into the more favorable state.[40] The boundary magnetization will follow the antiferromagnetic order, and if the boundary magnetization is exchange coupled to an adjacent ferromagnet, the exchange bias will also reverse. Importantly, this process can be performed isothermally and is completely reversible. The first demonstration of isothermal electric control of exchange bias in a chromia-based heterostructure was done by He et. al. using a Co/Pd perpendicularly anisotropic ferromagnet exchange coupled with a chromia (0001) sample, the results are shown in Fig 1.5.1.[37]

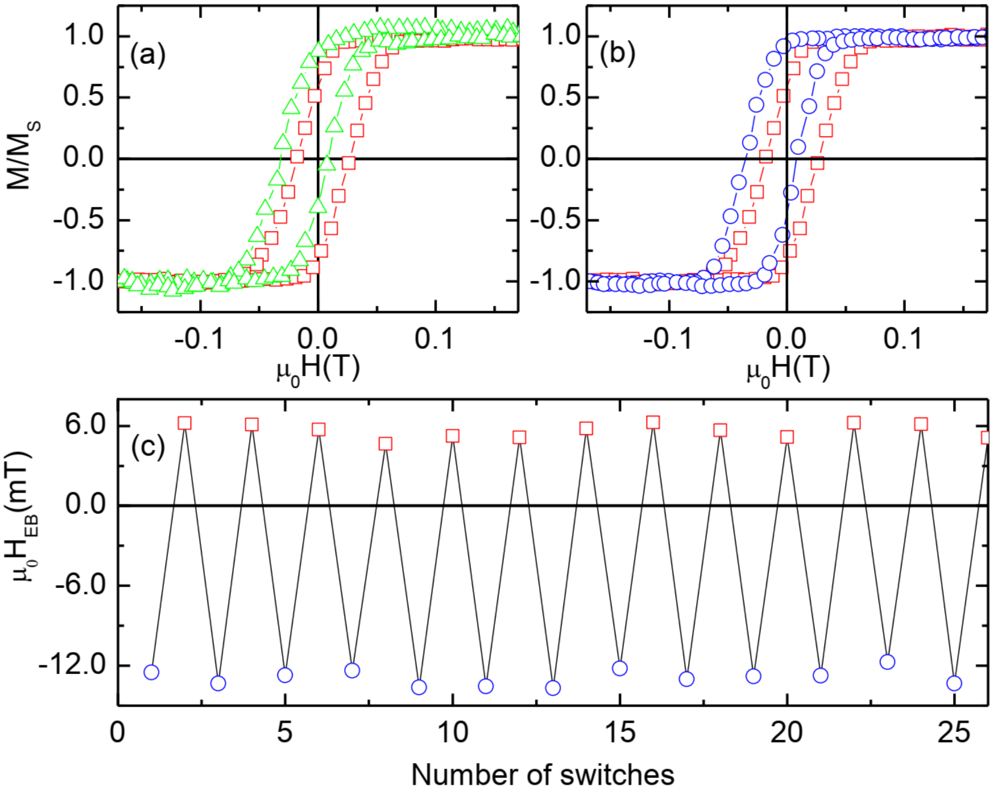

Figure 1.5.1: (a) Two ferromagnetic hysteresis loops of ferromagnetic/chromia heterostructures. Red squares show the hysteresis after magnetoelectric annealing E>0 and B>0, green triangles show the hysteresis after isothermal switching in E<0 and B>0. (b) Red squares show the same loop as in (a) after magnetoelectric annealing, blue circles show the hysteresis after isothermal switching in E>0 and B<0. (c) Exchange bias after a number of switches with a constant B<0 and E>0 (blue circles) or E<0 (red squares)

It was further verified that the critical switching thresholds obey the relation $|EH|_c = constant$, as expected from the conditions allowing the coherent flip of the antiferromagnetic domain state. Since the product $|EH|_c$, defines the critical threshold it follows that the magnetic switching field can be made arbitrarily small, as long as the electric field compensates. This ability to trade between electric and magnetic field requirements is important for low energy devices. For example, a small magnetic field can be supplied at no additional energy by a permanent magnet in the proximity of the device.

Since the initial study on electrically-controlled exchange bias in chromia-based heterosystems, more successful demonstrations have been done.[47, 48] Of particular interest are those experiments in which the exchange bias is larger than the ferromagnetic coercive field, that is $|H_{EB}| > |H_{Coerc}|$. In such systems the hysteresis loop will be fully shifted to one side or the other with respect to the zero magnetic field point. Then, at zero magnetic field, the ferromagnet will be fully saturated in either the up or down magnetization state depending on if the exchange bias is negative or positive. If the exchange bias is then electrically-controlled, as demonstrated above, and the required magnetic field can be made arbitrarily small, for example $|H_{switch}| < (|H_{EB}| - |H_{Coerc}|)$, the result is that as the exchange bias switches, the magnetization of the ferromagnet switches along with it. Such a device would be useful for a variety of applications, one major one being the ME-MTJ.

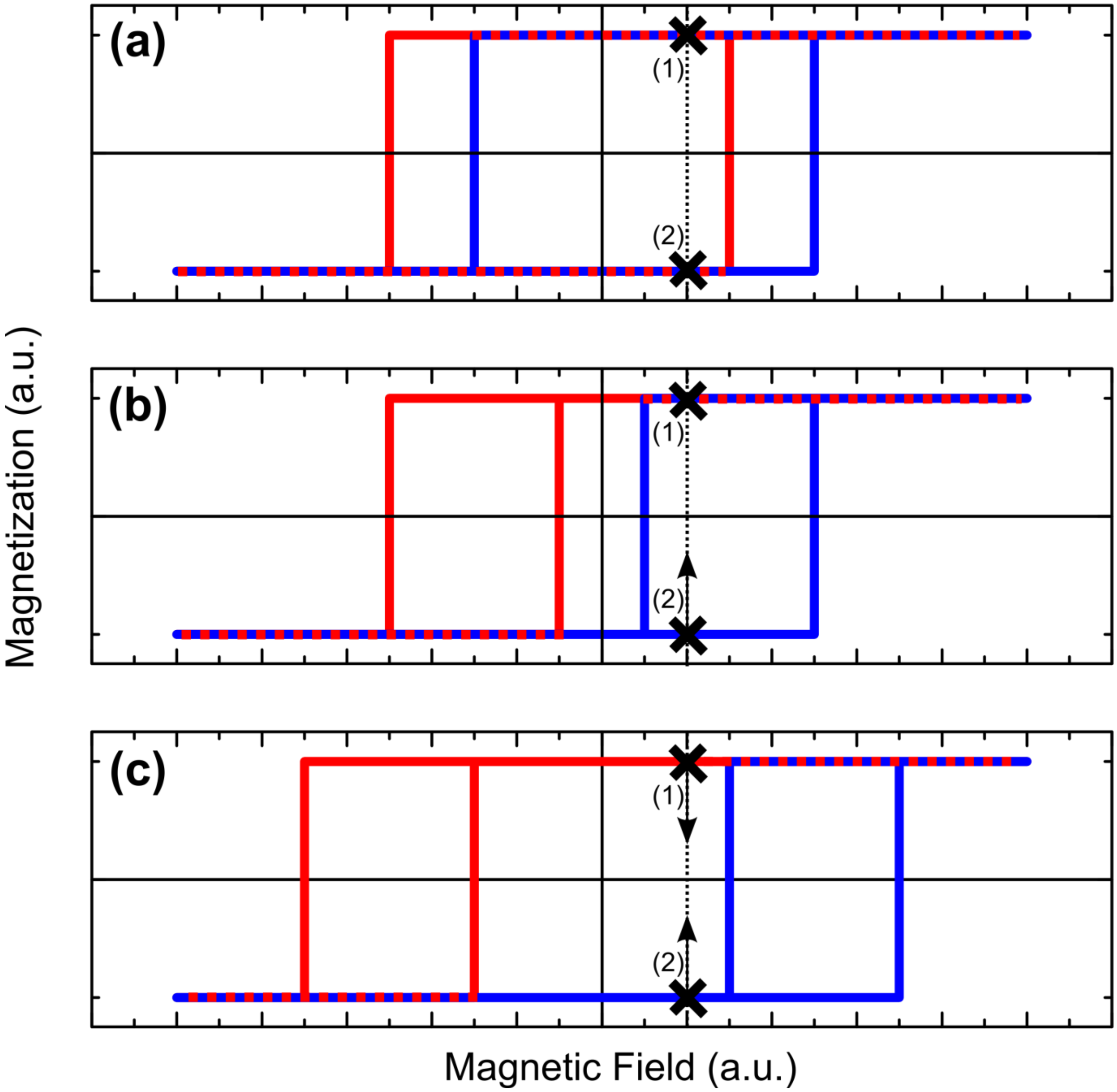

Figure 1.5.2: Illustration of the ferromagnetic switching criterion ($|H_{EB}| > |H_{Coerc}|$ and $|H_{switch}| < (|H_{EB}| - |H_{Coerc}|)$) in ferromagnetic/antiferromagnetic exchange biased systems. (a) $|H_{EB}| > |H_{Coerc}|$ is not fulfilled, thus there is no magnetization switching with exchange bias switching at the designated magnetic switching field (dashed line). (b) $|H_{switch}| < (|H_{EB}| - |H_{Coerc}|)$ is not fulfilled, thus there is only unidirectional switching. (c) Both criterion are fulfilled, thus there is bidirectional magnetization switching between points (1) and (2)

These switching criterion are illustrated in Figure 1.5.2. In panel (a), the first criterion is not satisfied ($|H_{EB}| \ngtr |H_{Coerc}|$), therefore, for a magnetic switching field as shown by the dashed line, if the system was at point (1) and the exchange bias was electrically switched from the red hysteresis loop to the blue hysteresis loop, the magnetization would remain at point (1) because both hysteresis loops have that state available. Likewise for point (2) in panel (a). In panel (b), the first criterion is satisfied ($|H_{EB}| > |H_{Coerc}|$), but the second criterion is not ($|H_{switch}| \nless (|H_{EB}| - |H_{Coerc}|)$), this leads to magnetization at point (1) to also be stationary when electrically switching between the red and blue exchange biased hysteresis loops, as in panel (a). Unlike in panel (a), if the system starts at point (2) in panel (b) on the blue hysteresis loop, and the exchange bias is electrically switched to the red loop with the magnetic switching field shown by the dashed line, the magnetization of the system would switch with the exchange bias because the magnetization state at (2) does not exist on the red loop. Finally, panel (c) illustrates the ideal scenario, with both criteria satisfied ($|H_{EB}| > |H_{Coerc}|$ and $|H_{switch}| < (|H_{EB}| - |H_{Coerc}|)$). Magnetization points (1) and (2), only exist on one hysteresis loop, thus when the exchange bias is switched from the red hysteresis to the blue hysteresis, the magnetization goes from point (1) to point (2) and vice-versa.

1.6 The Magnetoelectric Magnetic Tunnel Junction

The ME-MTJ is a three terminal device which converts a voltage signal into a non-volatile magnetic state.[2, 3, 49-51] The device is illustrated in Figure 1.6.1.

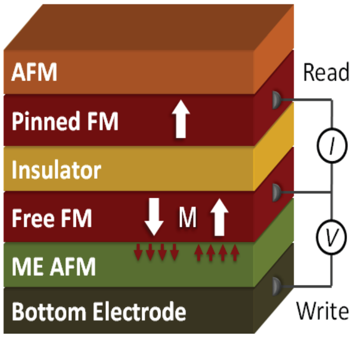

Figure 1.6.1: The magnetoelectric magnetic tunnel junction.

The working principle of this device is as follows. A voltage pulse is applied across the write terminals (between the free ferromagnetic layer and the bottom electrode) causing an electric field across the magnetoelectric antiferromagnetic layer. In combination with a constant external magnetic field (not shown), the sign of the electric field determines the domain state of the antiferromagnet. The domain state of the antiferromagnet determines the state of the boundary magnetization at the interface of the magnetoelectric and the free ferromagnetic layer. The orientation of the magnetoelectric antiferromagnet is chosen so that the boundary magnetization is perpendicular to the plane and parallel to the perpendicularly anisotropic free ferromagnetic layer. The exchange coupling between the boundary magnetization and the ferromagnetic free layer causes exchange bias in the ferromagnet. The properties of the free ferromagnetic layer are designed in such a way that the exchange bias field is larger than both the coercive field of the ferromagnet and the external applied field. Because of this condition, the magnetization of the ferromagnetic layer follows the direction of the boundary magnetization. The reorientation of the free ferromagnetic layer caused by a voltage pulse across the magnetoelectric antiferromagnet constitutes one write operation. An insulating tunnel barrier is placed between the free ferromagnet and the pinned ferromagnet. The pinned ferromagnet has its magnetization determined by the exchange coupling between it and the adjacent antiferromagnet which tops the stack. The exchange bias between the pinning antiferromagnet and the pinned ferromagnet must be sufficiently large to determine the magnetization of the pinned ferromagnet independent of the external magnetic field or any residual influence of the free ferromagnetic layer. The relative magnetic orientation of the pinned ferromagnet and the free ferromagnet will determine the resistive state of the device via tunneling magnetoresistance between the two layers, parallel for a low resistivity state (on) and antiparallel for a high resistivity state (off). The state of the device is read by measuring a small test current between the read terminals which connect the free and pinned ferromagnetic layer.

It has been shown that the ME-MTJ can be integrated into CMOS devices to provide non-volatile, high density, low power memory and logic functionalities. Circuitry that allows the ME-MTJ devices to interface with SRAM memory elements have already been proposed.[52] Moreover, the ME-MTJ can also serve as a fundamental building block for higher complexity devices. A three-terminal transistor, a majority (or minority) gate, an XOR gate, a full adder, a comparator, and an analog to digital converter have all been shown to be possible using the basic structure of the ME-MTJ.[53, 54]

Chapter 2: Sample Fabrication

This chapter outlines the methods used in fabricating the samples under study. The substrates used are commercially available Al_2O_3 (0001) (sapphire) of 99.99% purity and orientation tolerance of ±0.5°. The surface of the substrates is polished to a roughness less than 0.8 nm. It is on top of these crystals that devices were fabricated. Chromia, Vanadium oxide, and B-doped chromia were primarily grown with pulsed laser deposition while metallic layers were typically grown by molecular beam epitaxy or sputtering. Each deposition method has its own advantages and disadvantages, as well as limitations depending on the specific material which is grown. For certain samples, after the stack of thin films were deposited an additional step of lithography was sometimes done to pattern the film into microscopic lateral size.

2.1 Cleaning

To prepare high quality epitaxial films, a defect free substrate which is clean on an atomic scale is necessary. Surface contaminants are broadly categorized in three categories: molecular, ionic, or atomic.[55] These contaminants can lead to a variety of problems in sample fabrication, for example, molecular contaminants can cause poor film adhesion, ionic contaminants may diffuse into subsequently deposited samples causing electrical defects, and atomic contaminants may influence carrier lifetime or surface conduction among other problems.[55] Facing these challenges, Kern and Puotinen developed a cleaning procedure for silicon crystals which later became the industry standard.[55, 56] Whereas, hydrogen peroxide solutions at high pH were found to be particularly effective for removing organic contaminants by oxidation, and hydrogen peroxide solutions at low pH were effective for desorbing metal contaminants by complexing, the procedure suggested by Kern and Poutinen was a two step wet-etch process, using both types of solution in sequence.[55] The exact recipe and ratios can and have been adjusted over the years according to effectiveness[57] and specific application[58], but the basic process is: (1) submerge the substrate in an $H_2O+H_2O_2+NH_4OH$ solution, followed by (2) a $H_2O+H_2O_2+HCl$ solution. A preliminary treatment with a solution of $H_2SO_4+H_2O_2$ mixture can be beneficial for grossly contaminated samples.[56] Based on these early results, Zhang *et. al.* developed a procedure specifically tuned to clean sapphire wafers.[58] The procedure was shown to be superior to several alternate cleaning methods[58] and is therefore the procedure regularly used to clean the sapphire substrates prior to deposition in this thesis. The procedure is as follows:[58]

1) The substrate is soaked in ethanol for 12 hours at room temperature. It is rinsed in de-ionized water and blown dry.
2) The substrate is sonicated in a detergent solution (Liquinox+ethanol+H_2O, 1:20:79 vol%) for 30 minutes at room temperature. It is rinsed in de-ionized water and blown dry.
3) The substrate is soaked in a solution of ($H_2SO_4+H_2O_2$, 3:1 vol%) for 20 minutes at 80° C. It is rinsed in de-ionized water and blown dry.
4) The substrate is soaked in a solution of ($NH_4OH+H_2O_2+H_2O$, 1:1:2 vol%) for 20 minutes at 80° C. It is rinsed in de-ionized water and blown dry.
5) The substrate is soaked in a solution of ($HCl+H_2O_2+H_2O$, 1:1:2 vol%) for 20 minutes at 80° C. It is rinsed in de-ionized water and blown dry.

2.2 Molecular Beam Epitaxy

Molecular beam epitaxy (MBE) is a form of crystal deposition which utilizes the high temperature sublimation of materials under ultra-high vacuum conditions to create a beam of material, which when directed towards a suitable substrate under suitable heating conditions, results in crystalline film growth. One of the necessary prerequisites to achieve MBE is an ultra-high vacuum chamber. The vacuum chamber in this thesis is manufactured by Createc, and is evacuated using turbomolecular pumps[59] backed by scroll pumps[60]. While the turbo molecular pumps can achieve pressures less than 10^{-8} mbar, to further reduce the pressure an ion pump is used in parallel.[61] Furthermore, the intermittent cycling of a titanium sublimation pump serves to capture certain hard to pump gasses such as hydrogen.[62] With this pumping profile, pressures of 10^{-10} mbar are achieved.

The total vacuum pressure is measured by a Bayard-Alpert ionization gauge[63, 64], while the individual components of the residual gas can be measured by mass spectroscopy.[65] To achieve pressures below 10^{-8} mbar, the vacuum chamber must be baked. Baking is the process of heating the chamber while continuously evacuating the residual gas. Baking is necessary to remove adsorbed gasses from the chamber walls, in particular adsorbed water.

The deposition technique relies on Knudsen effusion cells which hold a crucible made of suitable material, in this case alumina for Co/Pd/Cu and vitreous carbon for Cr. The required temperatures to achieve MBE are high enough that the crucible must be thermally isolated from the chamber itself to avoid damage. This is done by sheathing the effusion cell in a water cooling jacket. With sufficient water flow the elevated temperatures can be contained to the crucible itself and the heating wires which surround it. The crucibles are heated until the contents begin to sublimate at an appreciable rate. The molecular flow rate is given by [66]

$$J = \left[{ap(T)} \Big/ {\pi d^2 \sqrt{2\pi m k_B T}} \right] \cos(\theta) \tag{2.2.1}$$

where J is the flux per unit area, a is the cross-sectional area of the crucible, $p(T)$ is the vapor pressure of the substance at temperature T, d is the distance from the source, m is the mass of the molecule being sublimated, k_B is Boltzmann's constant, and θ is the angle between the beam and the normal of the substrate. Note the molecular flow rate is dependent on the vapor pressure and the vapor pressure is strongly influenced by the temperature of the substance, for instance, the vapor pressure of palladium has been found to be $\mathrm{Log}(p_{mmHg}) = 8.749 - 18655/T$.[67] The beam is collimated simply due to the fact only those molecules which are moving towards the opening of the crucible escape, while all others collide with the surface of the narrow crucible. The ultra-high vacuum environment ensures the material in the beam transverses the distance from the source to the sample with a minimum amount of scattering from background atmosphere. Upon impinging on the sample, one of three things may happen, the molecule may come to rest on the sample (adsorption), the molecule may move to a different site on the sample (migration), or the molecule may move off the sample altogether (desorption). The rates at which each of these processes take place is determined by a variety of factors, including substrate temperature, flux rate, source temperature, substrate material, source material, substrate roughness etc. These surface kinetics, along with the molecular flux rate determine the quality and growth mode of the film. There are three typical growth modes, Frank-van der Merwe (layer-by-layer), Volmer-Weber (3D island), Stranski-Krastanov (layer plus island). Epitaxy is accomplished when the deposited material forms a single oriented crystalline layer on the substrate.

MBE relies on raising the temperature of the source material to a point where an appreciable vapor pressure is created. For many elemental metals this is achievable, and in those cases, MBE excels at creating epitaxial crystals with sharp interfaces and correct stoichiometry. On the other hand, many oxides of interest do not achieve substantial vapor pressures in a temperature range suitable for MBE. In other cases, deposition of complex molecules by high temperature sublimation may risk changing the stoichiometry of the source over time. For those applications where MBE is not appropriate other growth mechanisms such as pulsed laser deposition or sputtering might be beneficial.

2.3 Pulsed Laser Deposition

Pulsed Laser Deposition (PLD) is a conceptually simple thin film epitaxy technique, but the underlying non-equilibrium mechanisms involved are extremely difficult to model.[68-70] PLD is especially attractive due to the fact that the stoichiometry can be preserved from the target to the substrate with relative ease. As a result, PLD has been pivotal in the deposition of high T_c superconducting films of complex stoichiometry.[69, 71] A high intensity pulsed laser is directed towards a material target where it creates a region of flash heating. For efficient energy transfer, short laser pulses are used to minimize energy loss due to thermal diffusion, and the wavelength of light should be strongly absorbed by the target material.[70] The beam fluence is high enough to heat a thin surface layer of the target material beyond the melting temperature of the target material and initiate rapid expansion and evaporation, creating a plume of material traveling away from the target. Due to the intense absorption of optical energy in a short time span all of the target molecules are ejected from the surface equally, encouraging stoichiometric transfer.[70] The plume may further interact with the laser pulse by way of free electrons near the surface which are accelerated by the electromagnetic radiation. These electrons can then collide with other atoms in the plume causing a rapid cascade. Even a small proportion of free electrons results in a marked increase in the absorption coefficient of the plasma, leading to electron-ion collisions becoming the dominant heating process.[68] This results in a self-regulating process in which a low density of the plasma results in more light interacting with the surface, which has the effect of repopulating the plasma.[72] Because of this mechanism, the plume itself may reach temperatures as high as 20,000 K while the target surface only reaches moderately above its melting point ~2000-3000 K.[70] The emitted particles travel toward the substrate where they are deposited, creating a thin film of material. The substrate is typically temperature controlled and is chosen to facilitate the desired crystal growth. The thickness of the film is controlled primarily by the number of pulses, while the deposition rate per pulse can be controlled by adjusting the energy per pulse or the distance between the target and the substrate.

The PLD system used in this thesis is the PLD/MBE 2500 system designed by PVD Products. The laser is a KrF exciton laser with a wavelength of 248 nm, operated at 160-220 mJ per pulse. The main chamber is pumped by turbo molecular pumps and has a base pressure of $\sim 5.0 \times 10^{-8}$ Torr. Six targets are placed on a motorized carousel which rotates for target selection and spins each target during use to utilize the target uniformly. A mechanized mirror placed in the optical train serves to raster the laser across the spinning target during deposition to ensure uniform ablation of target. Laser rastering is important, not only to maximally utilize the target, but to also avoid the etching of macroscopic grooves in the target, which will deform the plume profile, decreasing the overall deposition rate, as well as potentially influence the stoichiometry of the deposited film.[73] The system is also equipped with an “intelligent window”. As the deposition proceeds, the window which the laser traverses to enter the chamber becomes coated by the target material. This coating can reduce the fluence of the laser on the target, decreasing the deposition rate. Depending on the material properties and the chamber pressure, over time 40% or more of the incident energy can be absorbed.[74] The intelligent window mitigates this problem by using a much larger window, only a fraction of which is exposed to the plume at any time.[74, 75] When the active section of the window is partially coated, the window can be mechanically rotated such that a fresh area is now exposed to the plume. Since the usable area of the disk, throughout one complete rotation, is between 20-60 times that of a fixed window the lifetime of the window is significantly extended.[74] Also part of the intelligent window system is an insertable beam splitter which can divert the beam towards a Joule meter. This is useful to measure the fluence of the beam after it has passed the rotatable window, thus making it easy to detect when coverage of the active area has significantly dimmed the laser.[74] A photograph of the intelligent window system is shown below.

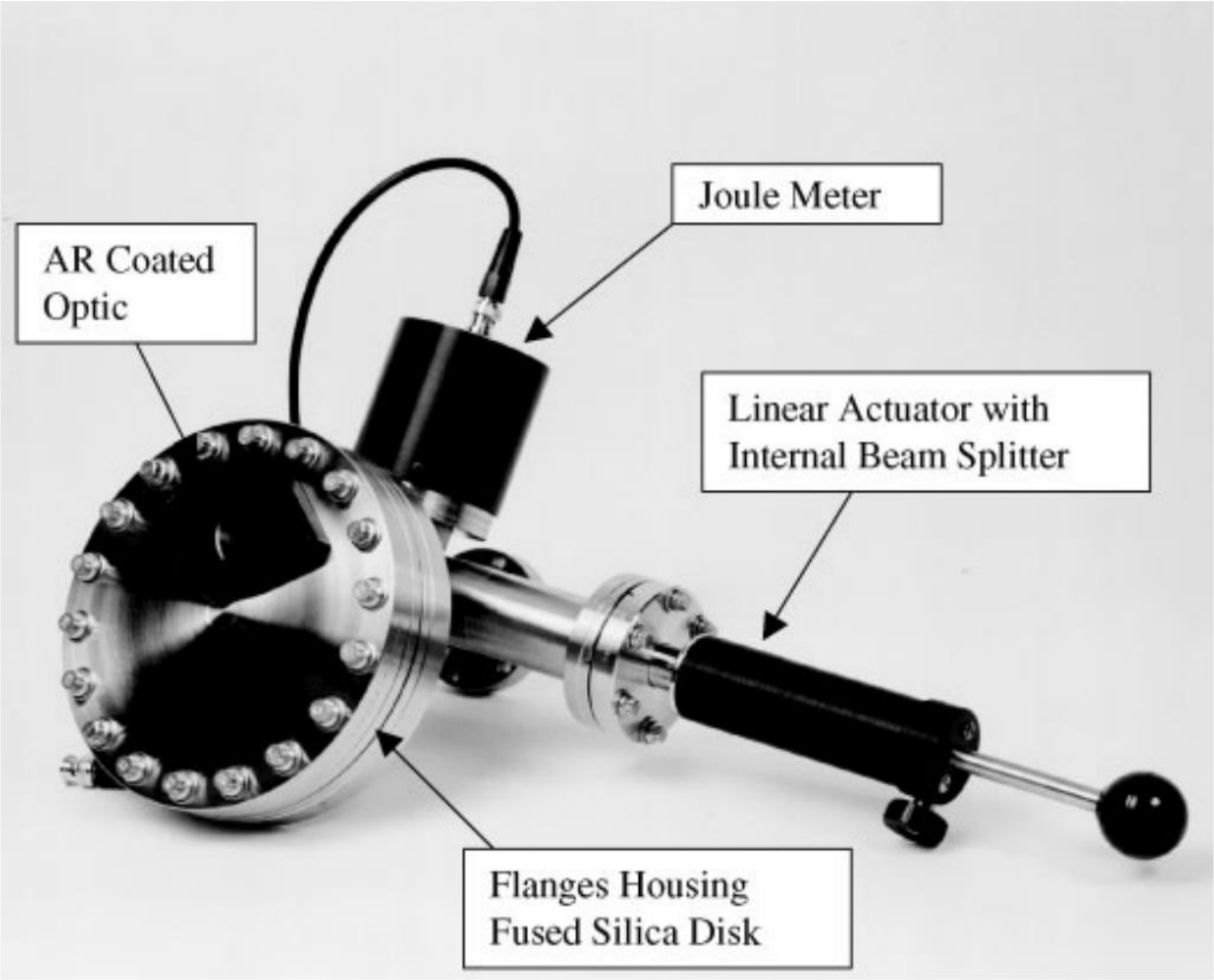

Figure 2.3.1: A photo of the intelligent window system. Photo from Greer[74], courtesy of PVD Products Inc.

In addition to the factory features of the PLD system, the one used in this thesis has an additional component used for boron doping. A small cylinder is attached to a precision leak valve which is subsequently attached to the main chamber. The cylinder is filled with a small amount of decaborane ($B_{10}H_{14}$) before being attached to the main vacuum chamber and evacuated of any remaining air. Decaborane is a highly volatile white crystalline solid with a vapor pressure of several Torr at room temperature.[76] A heater is wrapped around the cylinder to control the temperature of the decaborane, when in use the decaborane is maintained at a temperature of 80 C. When heated the decaborane sublimates and the gaseous decaborane is subsequently fed into the chamber through the precision leak valve. The decaborane pressure inside the chamber is monitored by a Bayard-Alpert ionization gauge and is adjustable between 10^{-7}-10^{-5} mTorr. In this manner, the growth of a chromia thin film can be done in an overall decaborane background pressure. By adjusting the background decaborane pressure the level of boron doping can be controlled. Decaborane begins to decompose above 170 C and decomposition is complete above 630 C.[76, 77] During the deposition of boron-doped chromia the sample temperature is held between 700-850 C to ensure complete decaborane decomposition as well as to assist defect free crystalline growth.

2.4 DC Magnetron Sputtering

Sputtering is the most popular thin film deposition technique.[78] High energy ions bombard a target, ejecting the target material which is subsequently deposited on a substrate. One straight forward way to accomplish this is to use an ion gun to generate high energy ions for target bombardment. While this is possible, the low sputtering yield of this method prevents it from being widely used. Rather than generating the ions from a plasma located in an ion gun which are subsequently accelerated toward a target, it is more efficient to create a plasma in the vicinity of the target for the purposes of bombardment. This is the basis of the most widely used sputtering methods. Typically, a vacuum chamber is evacuated to a high vacuum state, then a noble gas, usually argon, is introduced and a pressure of 10^{-2}-10^{-1} mbar of the gas is maintained. An anode and a cathode are positioned across the target such that the negatively charged cathode attracts positively charged ions to bombard the target. The plasma is created by applying a high voltage, typically of the order of a few thousand volts depending on the geometry, between the anode and cathode.

Ever present free electrons are accelerated in the field, colliding with and ionizing neutral gas molecules, creating an avalanche of electrons and ions. The voltage can be increased to the breakdown potential of the gas, at this point the current carried by the ionized particles is no longer controlled by the applied voltage, rather it is limited to the appropriate value by an external resistor. This region is known as the glow-discharge region, so-named due to the visible radiation being emitted by the ionized plasma. This is the region where sputtering is most often done at.

In the simplest arrangement as described above, the electron paths are only determined by the applied electric field. As a result, the pressure must be quite high to maintain the avalanche of ions used for sputtering. To address this issue, magnetron sputtering was developed. Magnetron sputtering keeps the free electron density high near the target by using an applied magnetic field. By introducing a magnetic field near the target, the free electrons emitted by the target are subject to the Lorenz force. These electrons travel in cycloidal paths near the target, increasing the number of collisions, which increases the plasma ionization rate and thus the sputtering rate. It was noted that under certain circumstances the inclusion of a magnetic field of 300 G brought about a 300-fold amplification of the discharge current.[79] The increased ionization efficiency of magnetron sputtering allows 10x lower operating pressures and/or significantly lower operating voltages compared to non-magnetron sputtering.[80]

2.5 Lithography

For certain samples it is useful to laterally structure the thin films. For example, in the case of Hall bars, the geometry of the device is essential to its operation. The dimensions of the current carrying portion of the device as well as the measurement arms must be strictly defined to accurately interpret the results. In other cases, it is simply useful to use smaller devices to reduce the number of defects in the device.

When structuring is needed, lithography is used. Lithography uses a polymer material called a resist which covers the sample evenly when applied with the help of a spin coater. Pieces of the resist are then removed to form a pattern. There are two lithography techniques used here, photolithography and e-beam lithography. In photolithography the resist used is photosensitive, when it is exposed to high intensity UV light it either becomes more soluble (positive photoresist) or less soluble (negative photoresist) in an appropriate chemical solution called the developer. Electron beam (E-beam) lithography operates similarly but instead of using directed light to expose the resist, a directed electron beam is used. Both photolithography and e-beam lithography have advantages and disadvantages. The main advantage of e-beam lithography is that it can achieve a higher resolution pattern. This is because the resolution of photolithography is limited by the wavelength of light used. One disadvantage of using e-beam lithography is that because it uses electrons, surface charging effects can become an obstacle, especially for insulating films, while photolithography does not have this problem. Generally speaking, e-beam lithography is a more time consuming, lower throughput method as compared to photolithography.

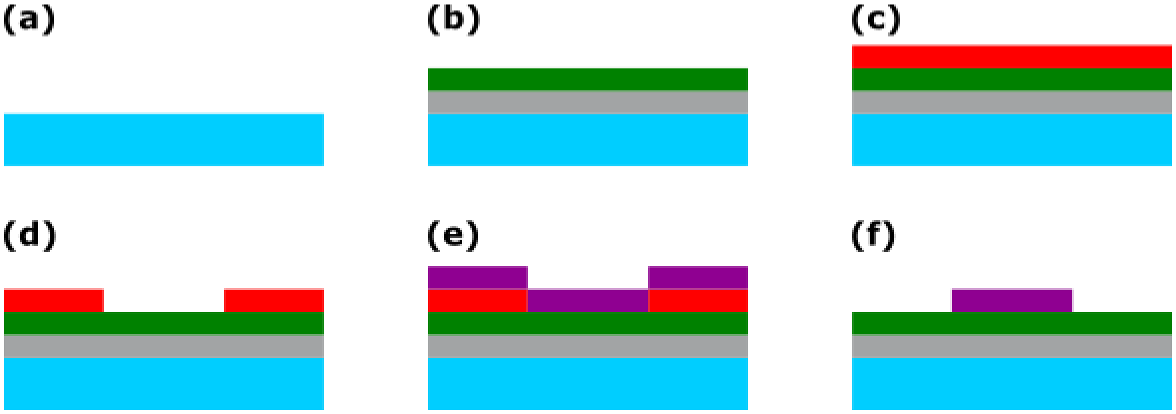

Figure 2.5.1: Illustration of the lithography process. (a) A clean sapphire (0001) substrate is used for deposition. (b) Any films which do not require structuring are deposited, for example a V_2O_3 film (gray) and a Cr_2O_3 film (green). (c) The resist is applied uniformly across the sample. (d) The lithography and development process removes a portion of the resist (e) Subsequent depositions are done, for example Pt is deposited (purple) (f) The resist is removed leaving a pattern in the remaining film.

After the sample is developed, a pattern in the resist remains. Subsequent depositions can then take place confining the growth of the new film to just those areas which are exposed. After deposition, the resist can be removed altogether by appropriate chemical treatment leaving a microscopically or nanoscopically patterned thin film. For more complex structures this procedure can be repeated as necessary. The lithography process is illustrated in Figure 2.5.1.

Chapter 3: Experimental Techniques

In this chapter the experimental techniques used to characterize samples structurally and magnetically are discussed. The thin films are characterized magnetically primarily using an apparatus measuring the magneto-optical Kerr effect which is extremely surface sensitive. A superconducting quantum interference device is also used to magnetically characterize the samples which, in contrast to the Kerr effect, is a bulk measurement. X-ray diffraction characterizes the samples structurally as it provides information about the crystallinity, lattice parameters, thickness and roughness, all of which may affect the magnetic properties of the film.

3.1 Magneto-Optical Kerr Effect

In 1877 John Kerr examined the light of a paraffin flame reflected from a polished iron core, he discovered that the plane of polarization of linearly polarized light is rotated upon the reflection from a magnetized metallic surface.[81] The magnitude of the rotation is directly related to the magnetization of the surface, and thus can be used as a contactless measurement of magnetization. Since its discovery, what is now known as the magneto-optical Kerr effect (MOKE) has become an indispensable tool for studying magnetic phenomena. The usefulness of MOKE is multi-fold. First, MOKE is surface sensitive, light only penetrates a metallic layer to a few nanometers in depth, this makes MOKE the ideal tool for studying magnetization in ultra-thin films. Next, MOKE is a high resolution technique, allowing spatial resolution down to the diffraction limit, and temporal resolution down to the picosecond level.[82, 83] In addition, due to its relative simplicity and remote detection, MOKE is an excellent and low cost technique for *in-situ* measurements.

In simplest terms the effect can be described with the following equation:

$$\begin{pmatrix} E_p \\ E_s \end{pmatrix}_r = \begin{pmatrix} r_{pp} & r_{ps} \\ r_{sp} & r_{ss} \end{pmatrix} \begin{pmatrix} E_p \\ E_s \end{pmatrix}_i \qquad (3.1.1)$$

Here, $\vec{E}_i$ is the polarization of the incoming light, $\vec{E}_r$ is the polarization of the reflected light, and $r_{pp}, r_{ss}, r_{ps}, r_{sp}$ are the Fresnel reflection coefficients. s and p indicate the components of the polarization in mutually perpendicular directions in the plane of incidence where s stands for perpendicular (from the German word senkrecht=perpendicular) and p stands for parallel to the optical plane spanned by the propagation vectors of the incoming and the reflected wave. The off-diagonal terms of the reflection matrix of Equation 3.1.1 are caused by the magnetization of the sample and account for the magneto-optical Kerr effect. In general, the reflection coefficients are complex numbers, and the light is elliptically polarized after reflection. The major axis of the reflected light is rotated with respect to the incoming light. The angle of rotation for a p-polarized incoming beam is given by[84]

$$\theta = Re\left(\frac{r_{ps}}{r_{pp}}\right) \qquad (3.1.2)$$

while the ellipticity is given by

$$\epsilon = Im\left(\frac{r_{ps}}{r_{pp}}\right) \qquad (3.1.3)$$

After reflection from the magnetized surface the angle of rotation of the light can be measured by, for example, determining the maximum (or minimum) of intensity of the light after passing through a second polarizer. The off-diagonal component of the reflection matrix is typically small resulting in small overall rotation. A magnetized Co/Pd multilayer, for example, with perpendicular magnetic anisotropy will produce a Kerr rotation of ~0.02 deg.[85] Due to the smallness of the typical Kerr angle more sophisticated methods are often employed to measure the rotation of the polarization. The following is a description of the MOKE configuration used in this thesis.

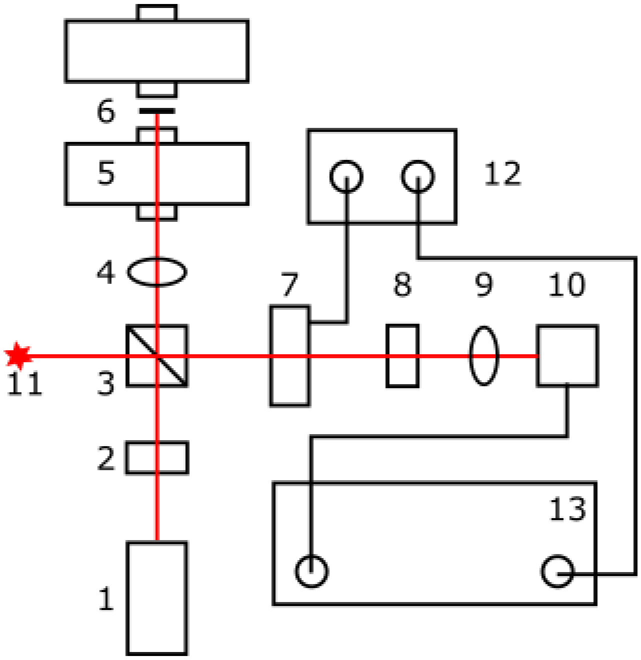

Figure 3.1.1: Diagram of experimental MOKE setup (1) Laser (2) Polarizer (3) Beam splitter (4) Lens (optional) (5) Magnet (6) Sample (7) Photoelastic Modulator (8) Polarizer (9) Lens (optional) (10) Detector (11) Beam stop (12) Modulator Control (13) Lock-in Amplifier

Figure 3.1.1 shows the typical MOKE experimental setup. A 5 mW solid state laser diode is located at (1) which produces monochromatic light of a wavelength 532 nm. The beam is directed through a Glans-Thompson polarizer (2) with an extinction coefficient of 10^{-5} polarizing the beam. Next the beam passes through a polarization preserving 50:50 beam splitter (3) which splits the beam down two paths one towards (4) and one towards (11). There is a beam stop located at (11) which halts the beam, this portion of the light is not used. Located at position (4) is an optional focusing lens. A focusing lens can be employed here if there is a small (~100-500 μm) area of interest on the sample. The focusing lens serves to concentrate the light onto the area of interest as well as magnifying the final image of the sample. The beam passes through a 5 mm hole drilled lengthwise through the pole of an electromagnet (5). The light is incident on the reflective magnetic sample at (6), striking the sample perpendicular to the plane of the sample, this configuration is known as polar MOKE and is sensitive to the perpendicular component of the magnetization.[86] If temperature control is required, the sample may be contained within a cryogenic chamber. The windows of the cryogenic chamber are composed of fused silica. The interaction of the light with the fused silica windows in the presence of a magnetic field add an additional rotation of the polarization angle of the light due to the Faraday effect. This additional rotation is cumulative as the light passes the window a second time after being reflected back towards the beam splitter (3). The Faraday rotation caused by the windows is linear in the applied magnetic field and can be subtracted from the final data. Upon arriving at the beam splitter, after reflection from the sample, 50% of the reflected light is directed through the photoelastic modulator (7) which modulates the light at a frequency of 50 kHz as determined by the modulator control unit (12). The modulated light passes through a second polarizer at (8) which is set at an angle α with respect to the initial polarizer. There is an optional second lens at (9) which can be used if the optional lens (4) is also used. The lens at (9) serves to magnify the image of the area of interest as well as bring it into focus at the detector. The focal lengths of both the optional lenses need to be carefully selected to account for the relevant distances. The signal is detected at (10) with the use of a photosensitive diode.

The signal from the detector is sent to a lock-in amplifier at (13) which uses a technique known as phase-sensitive detection to increase the signal-to-noise ratio of the measurement.[87] The reference signal used to accomplish the phase sensitive detection is supplied by the photoelastic modulator control unit and is fed into the reference signal receiver of the lock-in amplifier.

Polisetty et. al. have done a complete analysis of this very MOKE apparatus to optimize the signal to noise ratio.[88] The phase of the modulation was calculated to maximize both the first and second harmonic measurements; moreover the entire optical train was scrutinized using Jones matrix formalism. Each relevant optical element (polarizer, sample, modulator, analyzer) was modeled by a Jones matrix. By considering how each matrix element interacted with the polarization of the light, the measured signal was quantified according to the magnetic vs. non-magnetic contributions to the signal. Several configurations were analyzed by varying the relative orientations of the polarizer, modulator, and analyzer with respect to each other and an optimal configuration, which maximizes the signal on both the first and second harmonic while simultaneously minimizes non-magnetic background contributions, was identified.[88] In this thesis all MOKE measurements were done under with this optimized configuration. Measurements were done at the second harmonic, the polarization angle of the second polarizer is set to $\alpha = 45°$ with respect to the first and the modulation phase amplitude is set to $\phi_0 = 175°$ at the modulator controller.

3.2 Super Conducting Quantum Interference Device

Superconducting quantum interference devices (SQUIDs) are magnetometers able to detect extremely small magnetic fields and therefore extremely small magnetic moments.

A SQUID combines the quantum phenomena of magnetic field quantization inside a superconducting ring, along with Josephson tunneling to detect magnetic moments as small as 10^{-8} emu (10^{-11} Am^2).

The electrons in a superconductor which are responsible for superconductivity are all in the same macroscopic wavefunction.[89] In conventional superconductors this is caused by electrons pairing into so called “Cooper pairs” at low temperature,[90] these Cooper pairs behave as composite bosons. The collective wavefunction of these electrons is required to remain single valued at each point in the superconductor, this gives rise to flux quantization when it is applied to a ring geometry.[89, 91] Flux quantization refers to the fact that inside a fully superconducting ring the magnetic field flux can take only the quantized values of $\Phi = n\hbar/e^*$, where e^* is the effective charge on the superconducting charge carriers and n is an integer, this is sometimes referred to as a flux unit. After this discovery, Josephson pointed out that by connecting two superconducting regions together across a weakly resistive barrier, a super current can tunnel across the barrier, connecting the wave functions in each part.[92] It was shown that current flow across a Josephson junction varies periodically with the magnitude of magnetic flux across the junction with minima when the junction contains an integer number of flux units.[93] Moreover, if two junctions are present interference effects arise which are analogous to double slit electron beam interference effects.[94] The resulting interference pattern depends sensitively on the applied magnetic field across the double junction, and thus is an extremely sensitive way to measure magnetic fields.

The commercial SQUID system used in this thesis is the Quantum Design MPMS XL-7. This device has built into it:[95]

1. A temperature control module suitable for controlling the sample temperature from 1.9 to 400 K.
2. A superconducting magnet which provides up to ±70000 Oe, using an oscillatory technique to minimize magnetic drift
3. A SQUID detector system including amplifier control electronics, sensing pick-up loops, and specially designed filtering with full computer control
4. A sample handling system which pulls the sample through the pick-up loops and allows automatic sample measurements using a microstepping controller with precision of 0.0003 cm.
5. A gas handling system which provides gas flow control for temperature regulation, flushing and cleaning processes.
6. A liquid helium handling system which provides refrigeration for the superconducting detection system and magnet, a well as providing for sample operation down to 1.9 K.
7. A computer control system with integrated MPMS control system operating software.

3.3 X-ray Diffraction

X-ray diffraction is a non-destructive technique to characterize the structural properties of a material. It relies on the regular repeated structure of the atomic lattice in a crystal to diffract a monochromatic beam of x-rays in a predictable pattern. By interpreting the diffraction pattern, the atomic structure of the crystal, including the interatomic spacing, symmetry, and other aspects can be deduced. To find the condition for constructive interference consider two scatterers separated by a displacement vector $\boldsymbol{r}$. Let a plane x-ray wave front be characterized by wave vector $\boldsymbol{k} = 2\pi\boldsymbol{n}/\lambda$, where $\boldsymbol{n}$ is the unit vector in the direction of $\boldsymbol{k}$**.** The scattered wave front will be characterized by $\boldsymbol{k}' = 2\pi\boldsymbol{n}'/\lambda$, where $\boldsymbol{n}'$ is the unit vector in the direction of $\boldsymbol{k}'$. From Figure 3.3.1, the condition for constructive interference is

$$\boldsymbol{r}\cdot\boldsymbol{n} - \boldsymbol{r}\cdot\boldsymbol{n}' = m\lambda \tag{3.3.1}$$

Or

$$\boldsymbol{r}\cdot(\boldsymbol{n} - \boldsymbol{n}') = m\lambda \tag{3.3.2}$$

Where m is an integer.

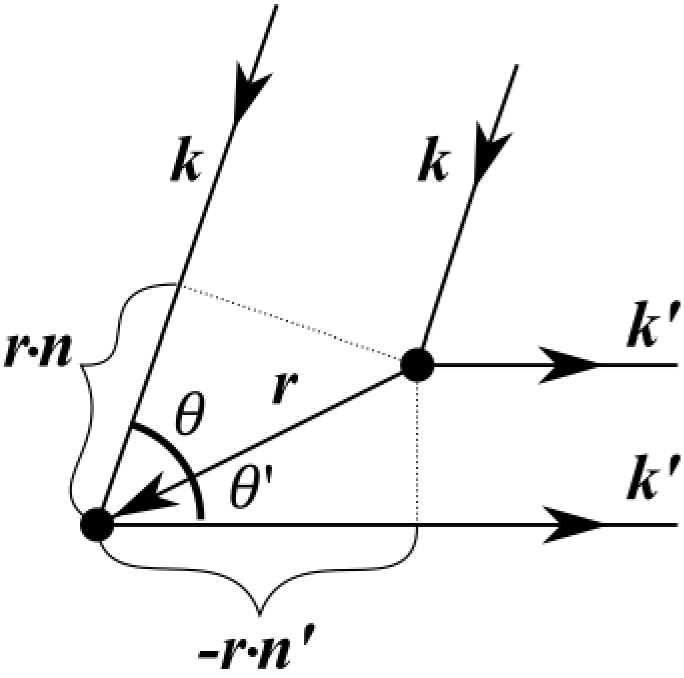

Figure 3.3.1: Illustration of the geometry of x-ray diffraction. An incoming wave of wave vector $\boldsymbol{k}$ is scattered by two lattice points, resulting in a wave of wave vector $\boldsymbol{k}'$

Multiplying both sides of Equation 3.3.2 by $2\pi/\lambda$ yields

$$\boldsymbol{r}\cdot(\boldsymbol{k} - \boldsymbol{k}') = 2\pi m \tag{3.3.3}$$

Equation 3.1.3 can be equivalently written

$$e^{i(\boldsymbol{k}-\boldsymbol{k}')\cdot\boldsymbol{r}} = 1 \qquad (3.3.4)$$

Comparing Equation 3.3.4 to the definition of the reciprocal lattice leads to the interpretation that constructive interference will occur provided that the change in wave vector $\boldsymbol{K} = (\boldsymbol{k} - \boldsymbol{k}')$ is a vector of the reciprocal lattice.[96] This interpretation leads quite naturally to identifying specific scattering vectors with Miller indices, which has become standard practice.

Note it is not assumed in Figure 3.1.1 that $\theta = \theta'$. For the case of spectral reflection, it is simple to see from the figure that the Bragg condition $m\lambda = 2rsin(\theta)$ is recovered.

Using just this simple analysis, information can be gained about the lattice parameter and crystal orientation, in a similar fashion, by mapping the diffraction pattern, information on the structure, phase, average grain size, crystallinity, and crystal defects can also be gleaned using x-ray diffraction techniques.[97]

The x-ray diffractometers used in this thesis consist of three basic parts, the x-ray source, the sample holder and the detector. The x-ray source consists of a cathode ray tube which provides electrons by heating a filament under high voltage, accelerating the electrons toward a target material which will provide the characteristic x-rays. These high energy electrons have sufficient energy to excite the inner shell electrons of the excited material, which, as they decay back to the ground state, provide certain characteristic x-ray spectra. The most prominent part of the x-ray spectra produced are the so called K_α and

K_β components, which occur when a vacancy from the $n = 1$ shell is filled. The K_α radiation is produced when an electron transitions from the $n = 2$ to $n = 1$ level, while the K_β radiation is produced when an electron transitions from the $n = 3$ to $n = 1$ level. The specific wavelengths of these radiations depend on the nature of the target material used. In this thesis only targets of Co (for the Rigaku D/Max-B diffractometer) and Cu (for the Rigaku SmartLab Diffractometer) are used which have K_α radiation wavelengths of 1.7903 Å and 1.5406 Å respectively. The K_α wavelength can be separated from the K_β wavelength as well as the bremsstrahlung background radiation by foils and/or crystal monochromators to produce the monochromatic beam used for diffraction. The beam of x-rays is focused and collimated toward the sample using either a Bragg-Brentano geometry or more commonly a parallel beam geometry depending on the application. The sample is positioned on the sample holder, and both the sample holder as well as the x-ray detector can be systematically moved relative to the x-ray source to sweep out $\theta - 2\theta$ measurements.

3.4 X-ray Reflectivity

X-ray reflectivity is a similar method to x-ray diffraction. The main difference between the two are that x-ray reflectivity takes place exclusively at low angle of incidence. X-ray reflectivity can typically be performed in the same apparatus as x-ray diffraction and is sometime known simply as low-angle x-ray diffraction. Reflectivity measurements are useful for gaining information about the near-surface region of materials and heterostructures, in particular thin film thickness/roughness/density analysis.

X-ray reflectivity measurements are done near the critical angle for total external reflection to occur. To good approximation, the index of refraction for x-rays in a material is given by[98]

$$n = 1 - \delta - i\beta \tag{3.4.1}$$

Where δ and β are determined by the scattering and absorption of the material, respectively. The critical angle calculated from Snell's law is given by

$$\cos(\theta_c) = n = 1 - \delta \tag{3.4.2}$$

X-rays are reflected specularly from a flat surface in a direction symmetric to the incoming beam. The specular reflectivity is given by

$$R(\theta) = I(\theta)/I_0 \tag{3.4.3}$$

Which is simply the ratio of the reflected to incident beam. Below the critical angle, incident x-rays are nearly all reflected. Just above the critical angle the reflection drops off quickly. The reflected intensity can, approximately, be calculated using Fresnel's equations. In the case of x-rays at low angles the reflectivity coefficient is calculated as[99]

$$R(\theta) = rr^* = \left|\frac{\theta - \sqrt{\theta^2 - \theta_c^2 - 2i\beta}}{\theta + \sqrt{\theta^2 - \theta_c^2 - 2i\beta}}\right|^2 \tag{3.4.4}$$

Reflectivity measurements are typically done on multi-layer structures; therefore we are primarily concerned with how an x-ray wavefront traverses and is reflected by multiple materials of different refractive indices and what effect that has on the simple Fresnel reflection coefficient. A polarized plane wave traveling through medium j in the xz plane can be represented as[99]

$$E_j(x,z) = \left(A_j^+ e^{ik_{z,j}z} + A_j^- e^{-ik_{z,j}z}\right)e^{i\left(\omega t - k_{x,j}x\right)} \tag{3.4.5}$$

$$= (U_j^+(z) + U_j^-(z))e^{i\left(\omega t - k_{x,j}x\right)}$$

where $k_{z,j}$ and $k_{x,j}$ are the component of the wave vector in the z and x direction respectively in medium j. Here, the upward and downward traveling waves are denoted with superscript $+/-$. If at a value of $z = z_{j+1}$, the wave front enters medium $j+1$, continuity of the electric and magnetic fields as well as conservation of $k_{x,j}$ at the interface yields[99]

$$U_j^+\left(z_{j+1}\right) + U_j^-\left(z_{j+1}\right) = U_{j+1}^+\left(z_{j+1}\right) + U_{j+1}^-\left(z_{j+1}\right) \tag{3.4.6}$$

$$k_{z,j}\left[U_j^+\left(z_{j+1}\right) - U_j^-\left(z_{j+1}\right)\right] = k_{z,j+1}\left[U_{j+1}^+\left(z_{j+1}\right) - U_{j+1}^-\left(z_{j+1}\right)\right]$$

Combining these equations we have

$$\begin{bmatrix} U_j^+\left(z_{j+1}\right) \\ U_j^-\left(z_{j+1}\right) \end{bmatrix} = \begin{bmatrix} p_{j,j+1} & m_{j,j+1} \\ m_{j,j+1} & p_{j,j+1} \end{bmatrix} \begin{bmatrix} U_{j+1}^+\left(z_{j+1}\right) \\ U_{j+1}^-\left(z_{j+1}\right) \end{bmatrix} \tag{3.4.7}$$

where

$$p_{j,j+1} = \frac{k_{z,j} + k_{z,j+1}}{2k_{z,j}}, m_{j,j+1} = \frac{k_{z,j} - k_{z,j+1}}{2k_{z,j}} \tag{3.4.8}$$

The 2x2 matrix which transforms the amplitudes of the electric field from medium j, to $j+1$ is known as the refraction matrix and can be denoted $\boldsymbol{R_{j,j+1}}$. Likewise, a translation matrix $\boldsymbol{T_{j,j+1}}$ can be defined which relates the amplitude of the electric field at the surface of medium j, and the amplitude at a depth of h.[99]

$$\begin{bmatrix} U_j^+(z) \\ U_j^-(z) \end{bmatrix} = \begin{bmatrix} e^{-ik_{z,j}h} & 0 \\ 0 & e^{ik_{z,j}h} \end{bmatrix} \begin{bmatrix} U_j^+(z+h) \\ U_j^-(z+h) \end{bmatrix} \tag{3.4.9}$$

For successive layers refractive and translational matrices can be handled by successive transformations with these matrices for each layer traversed as follows

$$\begin{bmatrix} U_0^+(z_1) \\ U_0^-(z_1) \end{bmatrix} = \boldsymbol{R_{0,1} T_1 R_{1,2}} \ldots \boldsymbol{R_{sub-1,sub}} \begin{bmatrix} U_{sub}^+(z_{sub}) \\ U_{sub}^-(z_{sub}) \end{bmatrix} \qquad (3.4.10)$$

The reflected amplitude of the electric field at the surface is given by

$$r = \frac{U_0^+(z_1)}{U_0^-(z_1)} \qquad (3.4.11)$$

As the angle of incidence is increased past the critical angle, more light penetrates further into the depths of the multilayer and the interaction of the x-ray light with the different layers gives rise to constructive and destructive interference. Mapping the intensity of the spectral reflection as a function of incident angle shows that the interference of different layers gives rise to so-called Kiessig fringes just above the critical angle. By fitting the Kiessig fringes appropriately, one can deduce, for example, the thickness of a thin film.

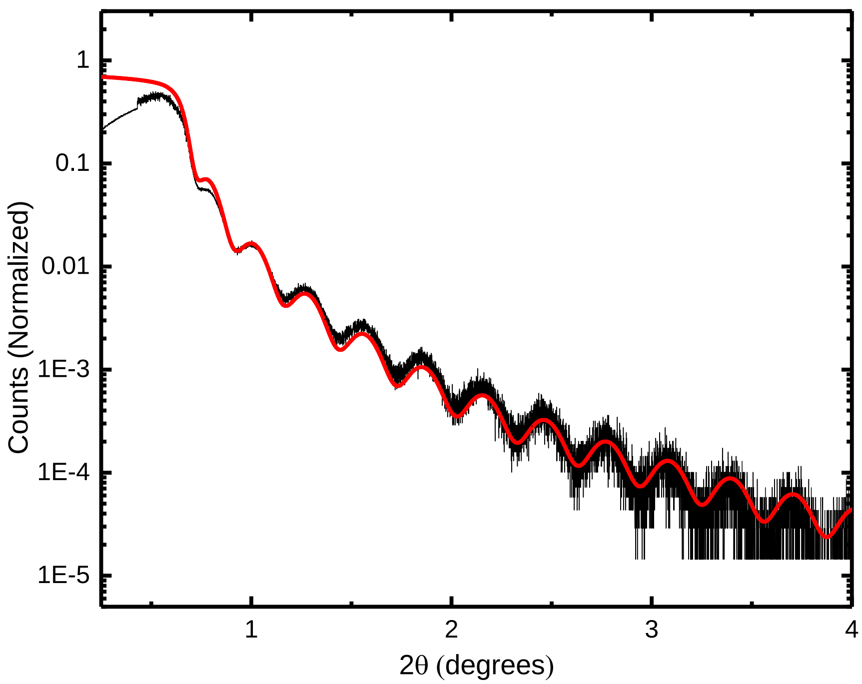

Figure 3.4.1: An x-ray reflectivity measurement a Cr_2O_3 film deposited on Al_2O_3 (0001) substrate. Data was taken on a Rigaku SmartLab using 0.154056 nm wavelength radiation. Thickness of the film is calculated by the fit (red line) to be 28 nm.

In addition to the thickness of any individual thin film, several other factors can change the profile of the Kiessig fringes including roughness, density, density gradient, porosity, background radiation, etc. which are beyond the scope of this thesis. These factors can and should be accounted for when fitting reflectivity data. Commercial software packages are available for fitting reflectivity data. For example, the software used in this thesis, Rigaku GlobalFit, can incorporate the relevant fitting parameters into an optimization routine to adequately fit reflectivity data.

3.5 Reflection High-Energy Electron Diffraction

Reflection high-energy electron diffraction (RHEED) is another diffraction technique used in addition to the aforementioned x-ray diffraction techniques to characterize thin films. RHEED has the advantages of extremely high surface sensitivity and ultra-high vacuum in-situ compatibility. These advantages allow RHEED to characterize the surface of the film, including layer coverage, crystallographic orientation, and morphology of the film while the film is in the process of growing.

Experimentally RHEED is a simple technique, an electron beam strikes a samples surface at a low angle of incidence (~1°) and is then reflected onto a phosphorescent screen which converts the electrons into photons. If the sample has a clean, crystalline surface the reflection will form a diffraction pattern on the screen as determined by the surface structure. Both the PLD and MBE growth chambers are equipped with RHEED capabilities.

The incident beam of electrons can be characterized by the wave vector $\boldsymbol{k}$, with $|\boldsymbol{k}| = 2\pi/\lambda$ where λ is the de Broglie wavelength of the electron. The wave vector of the reflected beam is characterized by its wave vector $\boldsymbol{k'}$**.** As seen in a previous section, the condition for constructive interference between two scattering centers separated by a displacement vector $\boldsymbol{r}$ is given by the von Laue diffraction condition[96]

$$(\boldsymbol{k} - \boldsymbol{k}') \cdot \boldsymbol{r} = 2\pi n \qquad (3.5.1)$$

where n is any integer. As depicted in the inset of Figure 3.5.1, if $\boldsymbol{r}$ is a vector constrained to the surface of the crystal, which is a reasonable simplification for surface sensitive RHEED measurements, several values of $(\boldsymbol{k} - \boldsymbol{k}')$ will lead to the same resulting dot product. This results in the so-called reciprocal lattice rods, because anytime the diffraction condition is met for any vector $(\boldsymbol{k}-\boldsymbol{k}')$, it will also be met by any other $(\boldsymbol{k}-\boldsymbol{k}')$ vector with the same in-plane projection.

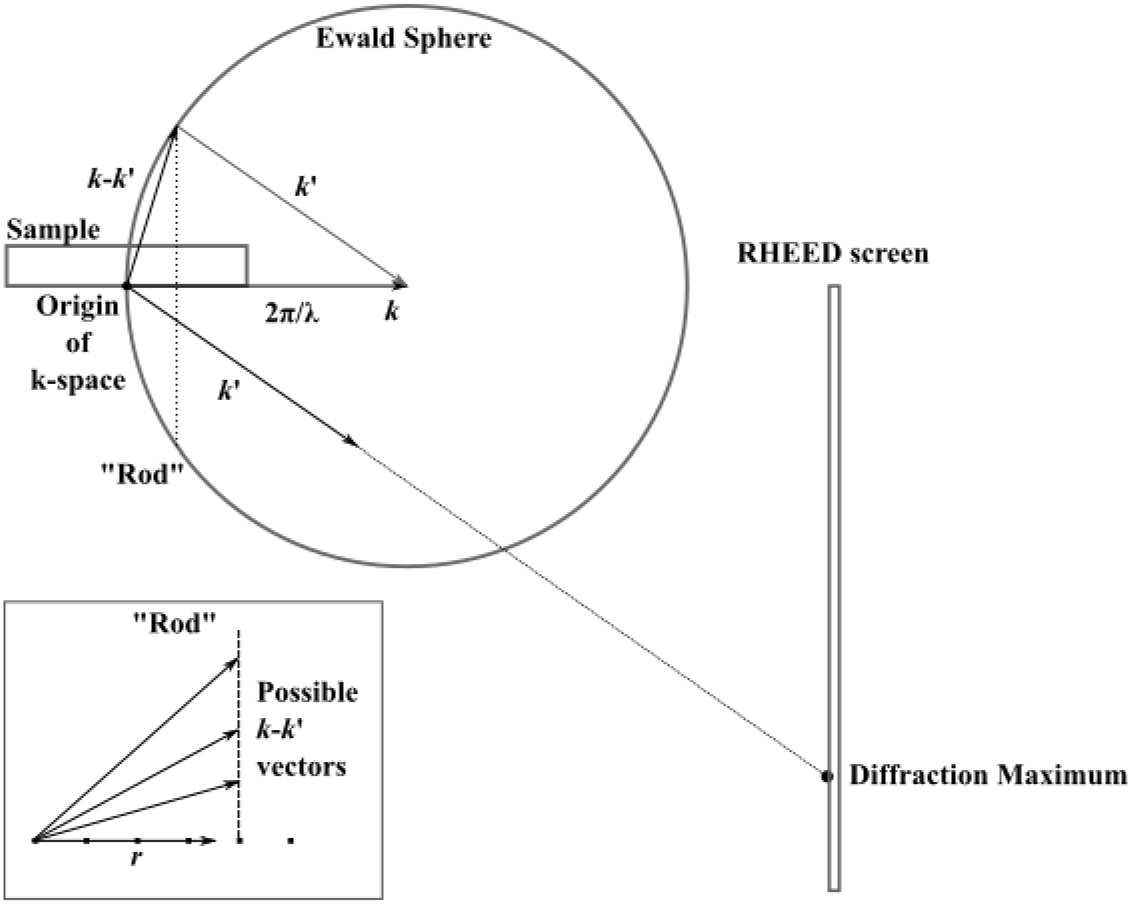

Figure 3.5.1: Cross section of the Ewald sphere in the plane of incidence using wave vector $\boldsymbol{k}$. Inset: A set of $\boldsymbol{k}-\boldsymbol{k}'$ vectors which define the reciprocal lattice rod. Figure adapted from Mahan et. al.[100]

In addition to the von Laue diffraction condition, in the simplest case, elastic scattering is typically also assumed, that is $|\boldsymbol{k}|=|\boldsymbol{k}'|$. As shown in Figure 3.5.1, choosing the origin of k-space to be the point of incidence, $(\boldsymbol{k}-\boldsymbol{k}')$ maps out a sphere known as the Ewald sphere. Combining the diffraction condition to the elastic scattering condition yields the result that a diffraction maxima will be observed along directions for which the tip of $(\boldsymbol{k}-\boldsymbol{k}')$ falls on a rod at the place where the rod pierces the Ewald sphere.[100]

Although, thus far ideal surfaces have been considered, there are some sources of noise which have a significant effect on the resulting RHEED pattern. As has been shown, an ideal surface in real space leads to rods in reciprocal space, but these reciprocal rods have a finite thickness due to lattice imperfections and thermal vibrations, additionally the Ewald sphere also has a finite thickness due to electron energy spread.[101] These unavoidable effects lead to the result that even for surfaces of the highest quality, the intersection of the reciprocal rods with the Ewald sphere leads to a streaked diffraction pattern.

RHEED can be an invaluable tool for monitoring film growth, especially for difficult or temperamental growth processes. For example, the growth of metallic palladium films on ceramic substrates by MBE may proceed in different growth modes depending on the rate of deposition and the substrate temperature. For high temperature and low deposition rate, growth tends to proceed in a 3D island growth mode.[102] The islands themselves may be crystalline and epitaxially matched to the substrate, but due to the growth mode a relatively large thickness may be necessary for the islands to converge into a uniform film, and the resulting roughness may be suboptimal. Whereas for low temperature and low deposition rate, growth tends to proceed in a 2D polycrystalline mode.[102] Due to these different growth modes, it is difficult to create a single growth condition which achieves highly oriented extremely thin platinum films on ceramic substrates. However this difficulty can be side stepped by a three step process[102], first grow a thin seed layer at high temperature. The seed layer will not be continuous, but it will be epitaxial. Next lower the temperature and grow an overlayer at low temperature. The overlayer growth will be nearly two dimensional but will be polycrystalline. Finally anneal the film at high temperature, the epitaxial grains from the seed layer grow throughout the overlayer resulting in a uniformly crystalline flat continuous film. The actual evolution of the films can be monitored by RHEED as demonstrated in Figure 3.5.2.

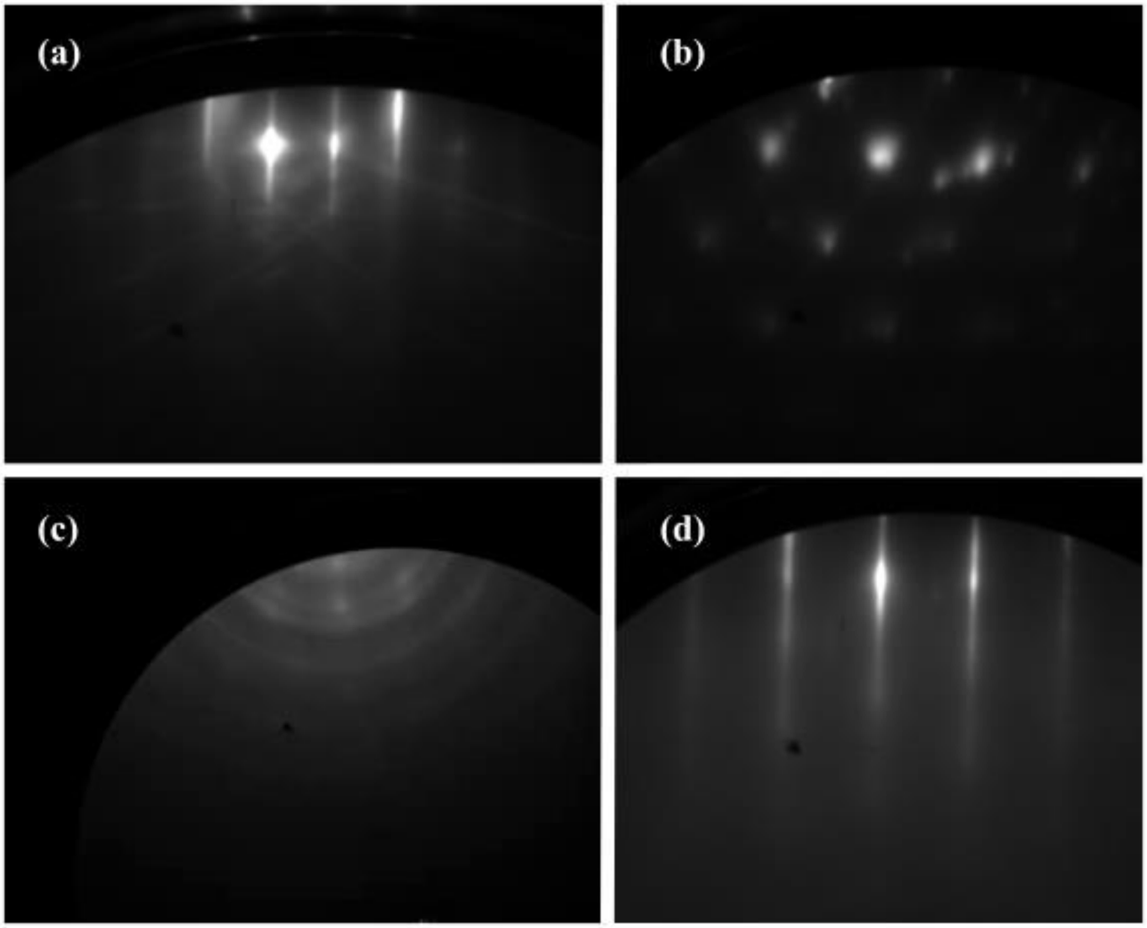

Figure 3.5.2: RHEED pattern during various stages of platinum deposition. (a) A clean Al_2O_3 substrate (b) A platinum seed layer deposited at high temperature (c) A platinum over layer deposited at low temperature (d) The film annealed at high temperature.

In panel (a) the RHEED pattern of a clean Al_2O_3 (0001) substrate is shown with the characteristic streaks of an exceptionally flat surface. Prior to deposition the sample temperature is maintained at 650 C, while the effusion cell is maintained at 1380 C resulting in a growth rate of 0.64 nm/min. A seed layer of palladium is grown at high temperature, the RHEED pattern shown in panel (b) is consistent with 3D island growth.[103] The temperature is then reduced to 0 C and an overlayer of platinum is grown. The circular rings shown in panel (c) are indicative of polycrystalline growth at low temperatures as the diffraction spots are smeared into rings due to the random orientation of crystallites in the film. Finally, panel (d) shows the same platinum film after the temperature is again raised to 650 C. The circular rings are replaced by a single streak pattern not only indicating the crystallinity of the sample, but also the extremely flat film surface.

3.6 Spinning Current Hall Magnetometry

In 1879 Edwin Hall discovered “a new action of the magnet on a current”.[104] The Hall effect as it is now known is the interaction of the charge carriers in a current with an applied magnetic field. In the presence of the magnetic field the moving charge carriers experience a Lorentz force curving their trajectories and causing an accumulation of charge on one side of the conductor. The accumulation of the charge carriers creates a transverse voltage of a magnitude which depends on the applied current, the applied field, the physical properties of the conductor and the geometry of the conductor. A few years later Hall discovered a similar but larger effect takes place in a conductor which is made of ferromagnetic iron. The second effect was subsequently named the anomalous Hall effect to distinguish it from the former. Today the Hall effect is part of a family of Hall effects including the anomalous Hall effect, the quantum Hall effect, and the spin Hall effect, among others.

As a measurement technique, there exists numerous uses for the Hall effects such as magnetometry[105-108], mobility and carrier density analysis[109-111], or even measuring the fine structure constant[112]. Although the mechanisms differ, each of these effects produce a transverse voltage due to a current moving through a material. As a result, the basics of the measurement technique in many cases are the same. Since the geometry of the current carrying wire is crucial in interpreting the results, Hall effect measurements are typically done on strictly defined structures often fabricated by lithography on thin films. One or more voltage probes are fabricated on each side of a current carrying leg allowing the transverse voltage to be measured while current is applied. The particular form can be varied as the application demands, but the Greek cross design shown in Figure 3.6.1 is particularly suited for spinning current measurements.

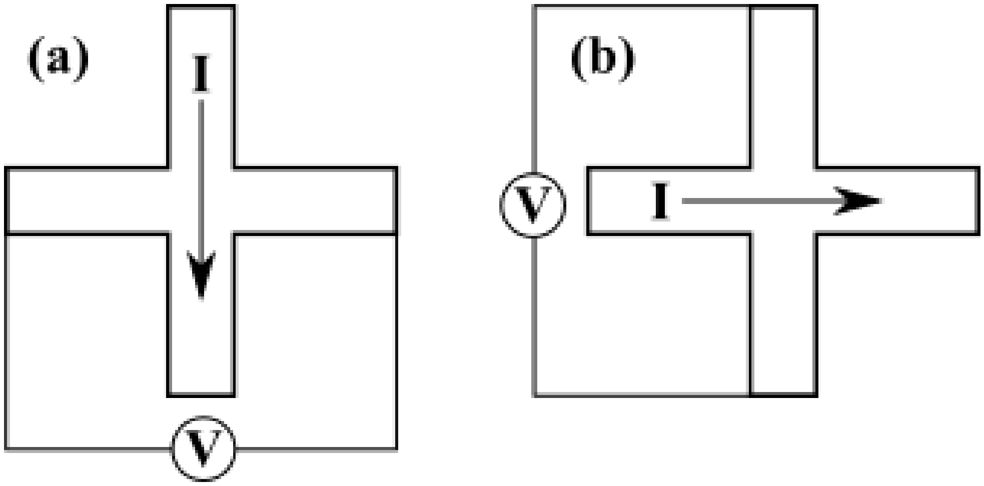

Figure 3.6.1: Diagram of a spinning current Hall effect measurement. The driving current and voltage measurement is switched between the two sets of terminals as indicated in (a) and (b)

Real Hall bar devices typically have some offset voltage, that is, some non-zero voltage between the voltage measuring terminals in the absence of any Hall effect. This can present a problem as the offset voltage can be up to 450 times larger than the Hall voltage and is subject to temperature variations in a sample.[113] The offset voltage is caused by the Hall voltage terminals not being on exactly equivalent positions with respect to the electric field lines pushing the current.[107, 108] Since the offset voltage adds to the Hall voltage it complicates the absolute measurements of Hall effects and may even obscure small signals. The spinning current method alternates the current direction and the voltage measurement between the two sets of terminals, summing the two measurements appropriately eliminates the offset voltage. The asymmetry in the device can be modeled by an equivalent circuit diagram as shown in Figure 3.6.2.[107]

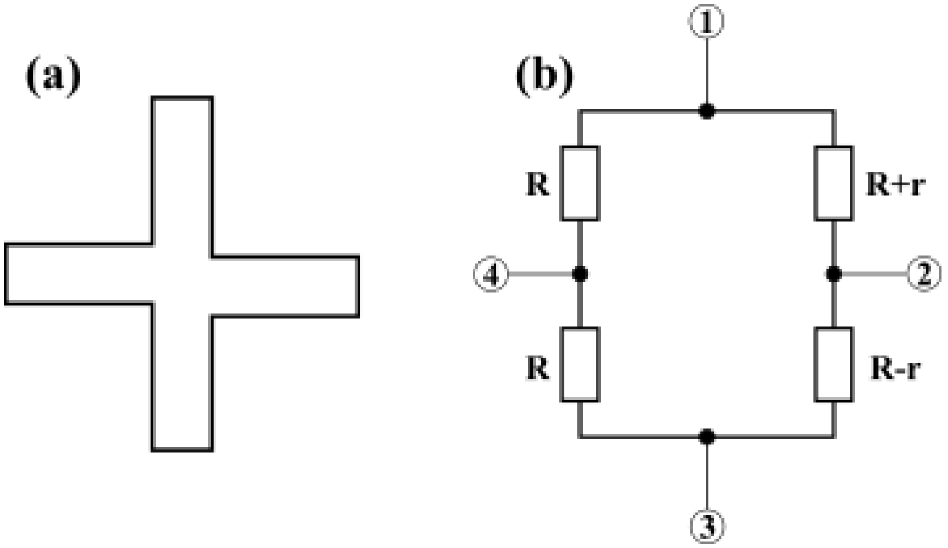

Figure 3.6.2: Equivalent circuit diagram for an asymmetric Hall bar. The asymmetry in one leg of the Hall bar in (a) is reflected in differing resistances around terminal 2 in (b).

As a current (I) flows from terminals 1 → 3, in the absence of any Hall voltage (V_H), due to the asymmetry of the circuit there remains a voltage between terminals 2 → 4 given by,

$$V_{24} = -\frac{V_{13} r}{2R} \tag{3.6.1}$$

The current between terminals 1 → 3 is given by,

$$I = \frac{V_{13}}{R} \tag{3.6.2}$$

When a Hall effect is present the total voltage V_{24} is given by

$$V_{24} = V_H - \frac{Ir}{2} \tag{3.6.3}$$

Likewise if a current is flows from terminals 2 → 4, in the absence of any Hall effect, the voltage between 1 → 3 is

$$V'_{13} = \frac{2RrV'_{24}}{(4R^2 - r^2)} \tag{3.6.4}$$

The current between terminals 2 → 4 is given by,

$$I' = \frac{4RV'_{24}}{(4R^2 - r^2)} \tag{3.6.5}$$

Therefore, when a Hall effect is present the total voltage V'_{13} is given by

$$V'_{13} = V'_H + \frac{I'r}{2} \tag{3.6.6}$$

If the driving current is equal in both cases, averaging the two voltages results in an offset free measurement.

$$\frac{V_{24} + V'_{13}}{2} = \frac{V_H + V'_H}{2} \tag{3.6.7}$$

Here is not assumed that the Hall voltages themselves are the same when measuring between different sets of terminals, but for those measurements where it is expected $V_H \approx V'_H$ the spinning current approach is appropriate.

Hall bars structures of non-ferromagnetic heavy metals on chromia have been experimentally established as a reliable readout mechanism for the boundary magnetization of chromia.[44, 108, 114] In particular, in the case of Pt on Cr_2O_3, the Hall signal is widely believed to originate from spin Hall magnetoresistance due to a non-zero imaginary component in the mixing conductance.[45, 115] The signal is however small, so the spinning current approach to Hall measurements is useful.[108] Switching the current and voltage leads between the terminals was accomplished using a 7012-S switch matrix card. Figure 3.6.3 shows the results of spinning current Hall magnetometry in a platinum thin film Hall bar fabricated on chromia. Under opposite field cooling conditions (+3T and -3T), the sample was cooled from 325 K to 280 K ($T_N = 307\ K$). Note that it has been previously shown in Cr_2O_3 thin-films that the magnetic field alone is sufficient to select a single domain state.[116] The zero field Hall signal was determined by linear fits of the measured Hall voltage after sweeping the magnetic field. At low temperature the transverse Hall signal splits, indicating opposite antiferromagnetic domain structures were selected with opposite boundary magnetizations. The temperature dependence of the Hall resistance is clearly correlated with the temperature dependence of the antiferromagnetic order parameter. These signals merge near 307 K, matching closely the expected Néel temperature of chromia. This demonstrates that the spinning current Hall magnetometry method is an effective method in magnetically characterizing appropriately fabricated chromia-based heterostructures.

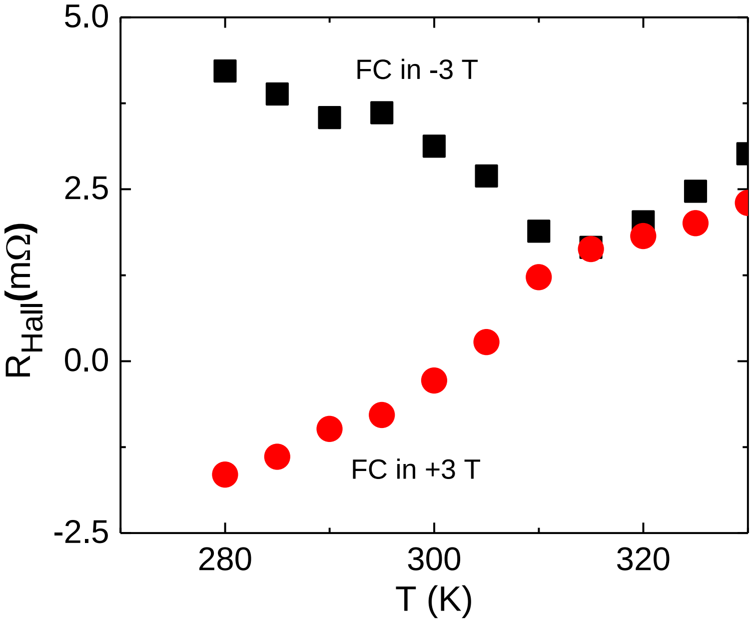

Figure 3.6.3: Temperature dependence of the zero field transverse Hall resistance in a Pt film on chromia. Measurements were made while warming up, after first cooling through T_N under applied magnetic fields of +3 T (red circles) and -3 T (black squares).

Chapter 4: Electrically-Controlled Exchange Bias Training

In this chapter, voltage-controlled exchange bias training and tunability are introduced. The evolution of the exchange bias is considered in a framework of spin relaxation triggered by consecutively cycled hysteresis loops. The corresponding exchange bias fields can be modeled with the help of a discretized Landau-Khalatnikov equation as $\mu_0 H_{EB}(n)$ where n is the loop index number. Isothermal voltage pulses are used to tune the antiferromagnetic order parameter of magnetoelectric chromia, and thus set the exchange bias of an adjacent CoPd film. It is seen that by tuning the antiferromagnetic interface into a nonequilibrium state, a state can exist in which the boundary magnetization is incommensurate with the underlying bulk. The subsequent relaxation of the boundary magnetization to its equilibrium state is responsible for the training observed. These results were published in Physical Review Letters.[117]

Upon the discovery of the electrically induced magnetoelectric effect in chromia it was found that, in the ordered phase, the magnetoelectric susceptibility α can be negative as well as positive and depends on the history of the sample.[31] The different signs in the magnetoelectric effect is explained by the existence of two electrically equivalent possibilities for the spin orientations of the magnetic unit cell of chromia each with opposite signs of α. The antiferromagnetic ordering of antiferromagnets such as chromia can be described by Landau Theory.[118, 119] In particular, the magnetic structure of a crystal can be described by an order parameter (η) such that it takes non-zero values for the ordered phase and is zero for the disordered phase. For antiferromagnets, η can be related to the sub-lattice magnetic moment of the crystal, with the conjugate field being the staggered field, h_{st}, which changes sign along with the periodicity of the antiferromagnetic sublattice.

In the perfectly ordered antiferromagnetic ground state, $|\eta|$ is at a maximum $|\eta| = 1$, while above the Néel temperature antiferromagnetic order is destroyed and $\eta = 0$. In the case of magnetoelectric antiferromagnets, the boundary magnetization is the symmetry driven consequence of antiferromagnetic order, therefore it must be the case that the boundary magnetization is directly linked to η, with $|m_{EB}|$ at maximum for $|\eta| = 1$ and $m_{BM} = 0$ for η=0.[38, 39] Indeed it has been shown experimentally that the boundary magnetization in chromia is directly tied to the antiferromagnetic order and does indeed disappear at the Néel temperature.[37, 42, 44, 47, 108, 120, 121] Moreover, the entire spin structure of magnetoelectric antiferromagnets, along with the boundary magnetization, can be reversed by the simultaneous application of electric and magnetic fields.[31, 32, 37, 40, 44, 47, 122] Therefore, magnetoelectric antiferromagnets not only provide an exceptionally simple way to electrically control the antiferromagnetic order parameter via magnetoelectric switching and annealing, but also a simple way to read the antiferromagnetic domain state via boundary magnetization. If a perpendicularly anisotropic ferromagnetic thin film is deposited on (0001) face of chromia, the out-of-plane boundary magnetization may pin the ferromagnetic film via the exchange interaction giving rise to exchange bias. As a consequence, in equilibrium, $H_{EB}(E) \propto m_{BM}(\eta(E))$ follows the isothermal switch of $\eta(E)$. Similarly, the temperature dependence $H_{EB}(T)$ follows the critical behavior of $\eta(T)$ on approaching T_N. Both experimental facts establish the approach to probe $\eta(E)$ via $H_{EB}^{\infty}(E)$.[37, 38, 121]

Voltage-controlled exchange bias and exchange bias training is investigated in a perpendicular heterostructure Cr_2O_3(0001)/Pd0.5nm/(Co0.6nmPd1.0nm)$_3$. The perpendicularly anisotropic ferromagnetic CoPd multilayer has been grown by molecular beam epitaxy on the (0001) surface of a chromia single crystal. The experiment employs the same exchange bias heterostructure which pioneered the isothermal voltage-controlled switching of exchange bias near room temperature.[37] Magnetic hysteresis loops of the CoPd film are measured via polar Kerr-effect using standard polarization modulation technique and phase sensitive detection.[88]

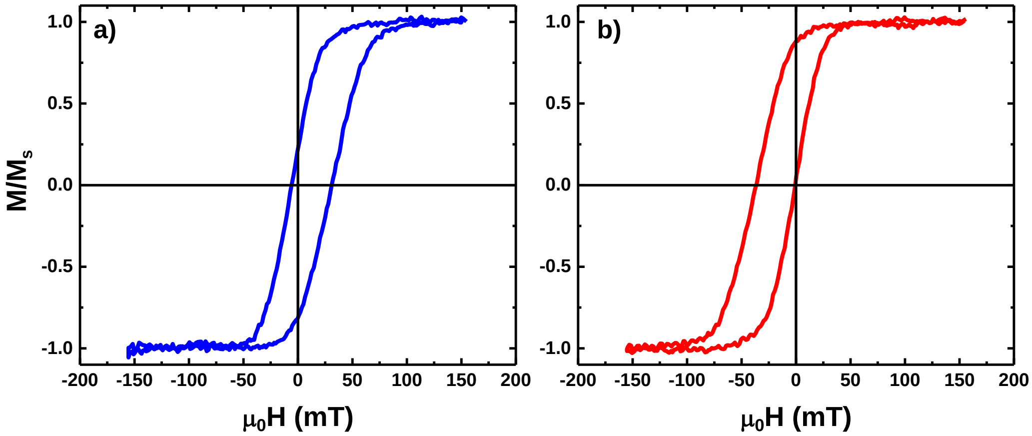

Figure 4.1: (a) Hysteresis loop of pinned CoPd thin film after magnetoelectric annealing of the sample. (b) Hysteresis loop of pinned CoPd thin film after electrically switching the spin configuration of the chromia

Figure 4.1 (a) shows a hysteresis loop with positive exchange bias shift measured at T = 303 K after preparing the chromia in a single domain state with negative boundary magnetization. This domain state has been selected through magnetoelectric annealing[123] from 350 K to 303 K, in applied electric and magnetic fields of E=100 kV/m and $\mu_0 H =$ 100 mT. The domain state of the chromia can also be selected by applying electric and magnetic field product isothermally. Above a critical field product $|\mathrm{EH}| > |\mathrm{EH}|_\mathrm{c}$ one antiferromagnetic single domain state switches into its reversed counterpart. Figure 4.1 (b) shows the resulting ferromagnetic hysteresis loop with negative exchange bias field after isothermally switching the exchange bias through inversion of the E-field while maintaining a positive magnetic field of $\mu_0 H = 100$ mT.

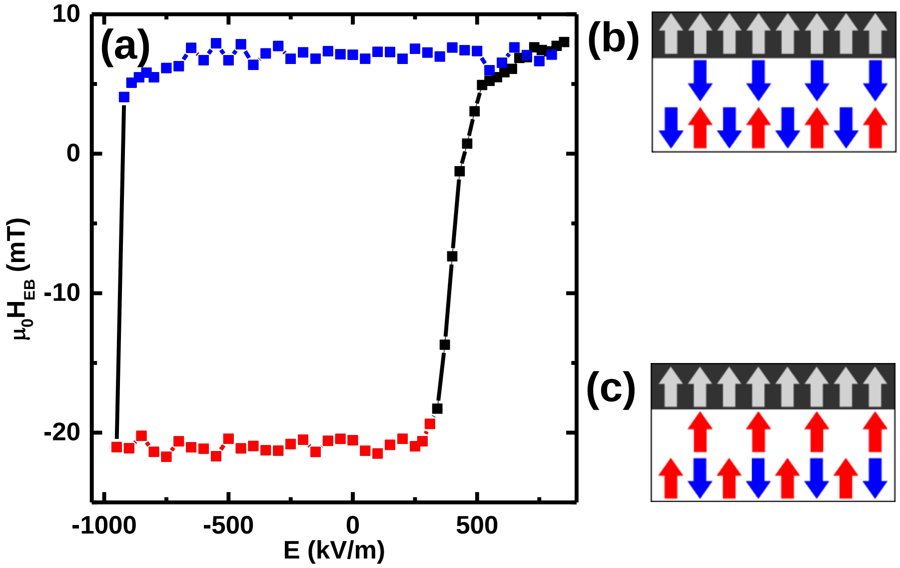

Figure 4.2: (a) Hysteretic behavior of equilibrium exchange bias with respect to applied electric field, a constant magnetic field of 100 mT is simultaneously applied. In the transition region, equilibrium exchange bias was determined by the 15th consecutive hysteresis loop. (b) Diagram of the spin structure of the antiferromagnetic bulk (bottom layer), the boundary magnetization (middle layer), and the ferromagnetic spins (top layer) in the positive exchange bias state. (c) The same as (b) except in the negative exchange bias state.

Figure 4.2 (a) shows the details of the complete hysteretic switching of exchange bias with applied electric field. In depth resolution is shown at the transition; here intermediate domain states with $|\eta(E)| < 1$ are electrically set and probed by the equilibrium exchange bias fields $H_{EB}^{\infty}(E)$. Figure 4.2 (b) depicts a simple model of the system in the positive exchange bias single domain structure and Figure 4.2 (c) the negative exchange bias single domain structure. The spin structure of the bulk (bottom layer), the boundary magnetization at the antiferromagnetic interface (middle layer), and the ferromagnet (top layer) is shown. The positive and negative boundary magnetization switches together with the voltage-controlled reversal of the bulk antiferromagnetic order parameter. Consequently the exchange bias fields switch as shown in Figure 4.1 (a),(b). The two single domain spin structures presented in Figure 4.2 (b),(c) are assigned to the two saturation regions of the hysteresis loop.

As seen in Figure 4.2 intermediate states between the two single domain states can arise. On approaching the critical threshold $(EH)_c$, the antiferromagnet transitions from $\eta = 1$ to $\eta = -1$ or vice versa through a series of states with $|\eta| < 1$. In these non-equilibrium states exchange bias training can occur. Exchange bias training refers to the change of the exchange bias when cycling the ferromagnetic layer through consecutive magnetic hysteresis loops. Training effects have previously been found in other heterosystems involving antiferromagnetic pinning layers.[124-127] Generally speaking, training effects are more important in polycrystalline samples and are expected to be very small or non-existent in magnetic heterostructures utilizing an antiferromagnetic single crystal.[12] The sample under study here is a remarkable exception to that rule. A nonstationary exchange bias indicates that the spin structure of the antiferromagnetic/ferromagnetic heterostructures is relaxing towards its equilibrium state.[124] It will be shown later on that, in this case, the antiferromagnet relaxes only at the interface while the bulk of the crystal remains stationary during the training, this gives rise to a potentially large training effect even in the case of a single crystal-based heterostructure.

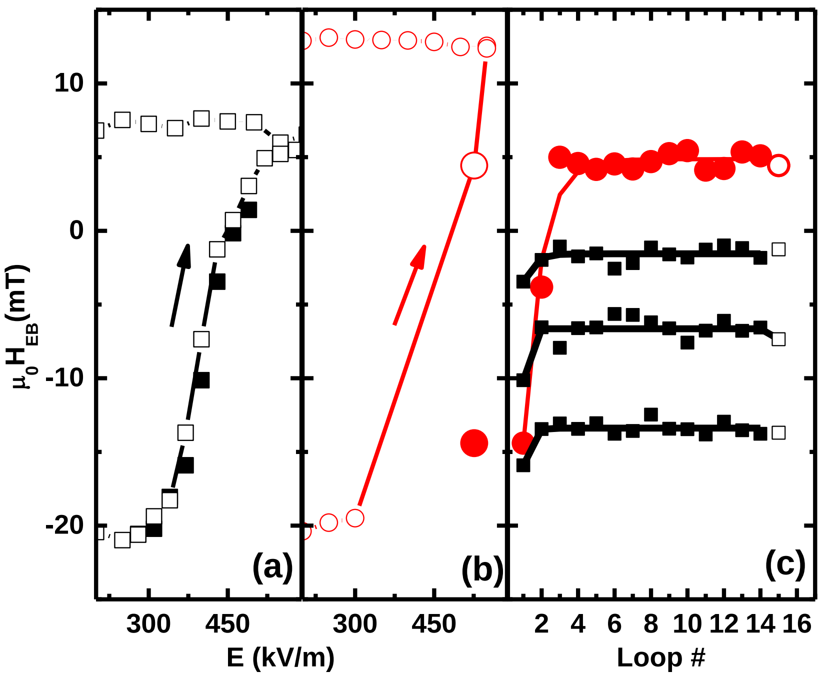

Figure 4.3: (a) Example of the hysteretic behavior of exchange bias with respect to the electric field applied in steps of 30 kV/m. The initial exchange bias is illustrated with solid symbols while the equilibrium exchange bias is illustrated with open symbols. The arrow indicates the history of the measurements. (b) Example of the hysteretic behavior of exchange bias with respect to applied electric field with one large step of 226 kV/m. The resulting initial and equilibrium exchange bias fields are displayed by large solid and open circles. The arrow indicates the history of measurements. (c) Circles show the exchange bias training series after initialization in a step from E=300 to E=526 kV/m. The first and fifteenth exchange bias values are also illustrated in (b) by a closed (n=1) and open circle (n=15), respectively. Squares show three exchange training series after initialization in a step from E = 340 to E = 370 kV/m, from E = 370 to E = 400 kV/m, and from E = 400 to E = 430 kV/m, respectively from bottom to top. First and fifteenth exchange bias values can be found in (a).

Figure 4.3 (a) and (b) show in detail the transition between negative exchange bias and positive exchange bias states. The initial exchange bias field is set via a voltage-pulse applied after the previous training cycle reached equilibrium. During training cycles the *E*-field is switched off. The exchange bias of the first loop, $H_{EB}(E, n = 1)$ (solid symbols), and the fifteenth loop $H_{EB}(E, n = 15) \approx H_{EB}^{\infty}(E)$ (open symbols) are plotted. In the first case shown in panel (a) the change in E between subsequent training cycles is small (30kV/m per step), keeping the exchange bias training of each cycle small. In the second case shown in panel (b) the E field was abruptly changed from 300 kV/m to 526 kV/m resulting in large exchange bias training. Figure 4.3 (c) shows the dependence of the exchange bias with respect to the number of sequentially measured hysteresis loops. Each of the black sequences shown in panel (c) corresponds to the measurements shown in panel (a) for electric field values of 370 kV/m – 430 kV/m, and the solid and open squares in panel (a) at these values are the first and fifteenth measurements shown in panel (c). Likewise, the full evolution of the two points shown at 526 kV/m in panel (b) is shown in panel (c).

Note that training of the exchange bias field toward $H_{EB}^{\infty}(E)$ does not imply that the bulk chromia relaxes asymptotically toward a single domain state. Bulk antiferromagnetic domain states with $|\eta| < 1$ are metastable but energetically separated by pronounced local minima. This leaves the spin structure in the antiferromagnetic bulk stationary in response to ferromagnetic hysteresis loops of the CoPd layer. Initially, however, after applying the set-fields, the antiferromagnetic interface region, which determines the boundary magnetization, can deviate from the bulk antiferromagnet domain structure. The initial antiferromagnetic non-equilibrium interface spin structure is incommensurate with the bulk. This mismatch originates from competing exchange with the underlying spins of the antiferromagnetic bulk and exchange with the adjacent ferromagnet. Hysteresis loops of the ferromagnetic film trigger relaxation of the antiferromagnet interface spin structure through coupling via the boundary magnetization. Consequently the antiferromagnet interface spin structure relaxes toward an equilibrium state which asymptotically becomes commensurate with the bulk. The changing boundary magnetization accompanying the evolving antiferromagnet interface spin structure gives rise to training of H_{EB} towards $H_{EB}^{\infty}(E)$.

It is important to recognize that the initial exchange bias field $H_{EB}(E, n = 1)$ is not a unique function of *EH* but depends on the history as expected from a hysteretic effect. Specifically, $H_{EB}(E, n = 1)$ depends on the domain state of the antiferromagnetic pinning layer before applying the set-fields. The history dependence explains the particularly pronounced training effect shown in Figure 4.3 (c) which corresponds to the large solid (n=1) and open (n=15) circles highlighted in Figure 4.3 (b). Here initialization of $H_{EB}(E, n = 1)$ took place from the single domain state with $\eta \approx 1$. Intuitively it is reasonable that the sizable electrically induced change from a single domain into a multi-domain state drives the antiferromagnetic interface far from equilibrium and thus far from a commensurate matching between interface and bulk

.

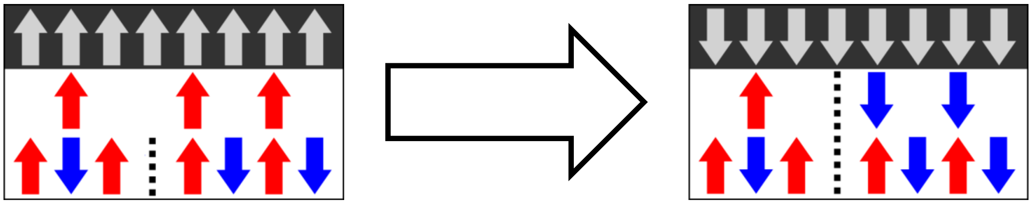

Figure 4.4: Diagram of the spin structure (up and down arrows) in a domain state after electric field initialization before training (left), and in equilibrium (right).

Figure 4.4 illustrates this process. The ferromagnetic layer is kept in positive saturation during initialization of exchange bias training and stabilizes the positive boundary magnetization associated with regular negative exchange bias (left). The voltage-induced reversal of the majority of the antiferromagnetic order parameter of the pinning layer is depicted by splitting the bottom layer into two opposite domain states separated by a dashed line. The majority of the antiferromagnetic bulk now favors negative boundary magnetization with a corresponding positive exchange bias in equilibrium. This results in competition and non-equilibrium spin structure at the interface. Reversal of the ferromagnetic layer (right) triggers relaxation of the antiferromagnetic interface spins accompanied by a large exchange bias training and (in the case shown in Figure 4.3 (b), a rather peculiar change in sign from $H_{EB}(E, n = 1) = -14.1$ mT to $H_{EB}(E, n = 15)$ = +4.43 mT. The antiferromagnetic bulk is static in this process.

The differing saturation values of the two hysteresis loops in Figure 4.3 (a) and (b) demonstrate the robust meta-stability of bulk AF domain structures. Since the maximum exchange bias shown in the upper part of panel (a) is reduced as compared to panel (b), it can be concluded that the sample in panel (a) is not in the fully single domain state with maximum boundary magnetization. Yet, in the upper region of panel (a) with $|E| < |E_c|$, training is absent despite the fact that the pinning system is not saturated in a perfect single domain state. It can therefore be concluded that the exchange bias training does not indicate that the domain state of the bulk of crystal is evolving. However, exchange bias training necessarily indicates some reorientation of the pinning layer. Taken together, this strongly supports the model that exchange bias training here originates from the interface region rather than the antiferromagnetic bulk. In addition, exchange bias training proceeds unidirectionally towards more positive values on the right side of the hysteresis and not necessarily towards the nearest single domain state. This behavior is inconsistent with bulk training but fits well with exchange bias training caused by competing exchange interactions at the interface. Note also that sizable exchange bias training can only be initialized at the right side of the $H_{EB}^{\infty}(E)$ hysteresis. This is again, strong evidence that the exchange bias training here results from competing interface exchange interactions. On the left side of the $H_{EB}^{\infty}(E)$ hysteresis the E-field reverses the antiferromagnetic order parameter into states favoring positive boundary magnetization. Positive boundary magnetization is, however, favored through exchange with the positively saturated ferromagnetic film. Hence competition leading to incommensurate interface spin structures is absent and as a result exchange bias training is absent.

Next quantitative analysis of the exchange bias training is outlined with the help of the discretized Landau-Khalatnikov approach. The discretized Landau-Khalatnikov theory has been developed previously for conventional antiferromagnetic and ferromagnetic pinning layers [124, 128]. For ferromagnetic films pinned by magnetoelectric antiferromagnet-based heterostructures the Landau-Khalatnikov theory of exchange bias training is formally in complete analogy to training in ferromagnetic hard/soft bilayers. The formal correspondence between training in magnetoelectric antiferromagnetic/ferromagnetic systems and ferromagnetic hard/soft bilayers originates from the fact that the boundary magnetization is directly proportional to the antiferromagnetic order parameter η, just as the ferromagnetic interface magnetization of a hard layer is proportional to the ferromagnetic order parameter. The free energy of the system can be expressed in a Landau type expansion as

$$F = F_0 + \frac{1}{2}\frac{\partial^2 F}{\partial S^2}\bigg|_{S=S_\infty} \delta S_n^2 + \cdots \tag{4.1}$$

Here, $S(n)$ is the boundary magnetization of the chromia, $\delta S_n = S(n) - S_\infty$ is the deviation of the boundary magnetization from the equilibrium state defined as $S_\infty = \lim_{n\to\infty} S(n)$. As noted earlier, this equilibrium state does not have to correspond to a global energy minimum, it is only the state after which subsequent cycling of the ferromagnet produces no further evolution of the boundary magnetization. Odd powers are omitted in the expansion by symmetry requirement $F(\delta S_n) = F(-\delta S_n)$. The relaxation of the system towards equilibrium is determined by the Landau-Khalatnikov equation

$$\xi \dot{S} = -\frac{\partial \Delta F}{\partial S} \tag{4.2}$$

where ξ is a damping constant, and $\Delta F = F - F_0$ is the non-equilibrium free energy of the chromia. As the evolution of the exchange bias is triggered by discrete reorientations of the magnetization of the adjacent ferromagnet, it is useful to discretize the Landau-Khalatnikov equation as

$$\frac{\xi[S(n+1) - S(n)]}{\tau} = -\frac{\partial \Delta F}{\partial S} \tag{4.3}$$

Here we take into account the state of the boundary magnetization at separate points corresponding to the number of consecutive ferromagnetic loop number n. The relevant experimental time constant between loops is given by τ. The derivative $-\partial \Delta F / \partial S$ to the lowest order is

$$-\frac{\partial \Delta F}{\partial S} = -\left.\frac{\partial^2 F}{\partial S^2}\right|_{S=S_\infty} \delta S_n \tag{4.4}$$

This can in turn be substituted into the discretized Landau-Khalatnikov equation to yield

$$\frac{\xi[S(n+1)-S(n)]}{\tau} = -\left.\frac{\partial^2 F}{\partial S^2}\right|_{S=S_\infty}(S(n)-S_\infty) \tag{4.5}$$

Substituting

$$K = -\frac{\tau}{\xi}\left.\frac{\partial^2 F}{\partial S^2}\right|_{S=S_\infty} \tag{4.6}$$

and solving for $S(n+1)$ gives

$$S(n+1) = (K+1)S(n) - KS_\infty \tag{4.7}$$

For convergence it is necessary to limit $-1 < K < 0$. The intuitive meaning of $-1 < K < 0$ has been previously discussed.[129] $K \to -1$ is the extreme case of a step-like exchange bias training where H_{EB}^{∞} is reached for $n \geq 2$. On the other hand, $K \to 0$ resembles continuous training with small changes between the exchange bias of subsequent loops, such that the boundary magnetization only asymptotically approaches its equilibrium value for $n \to \infty$.

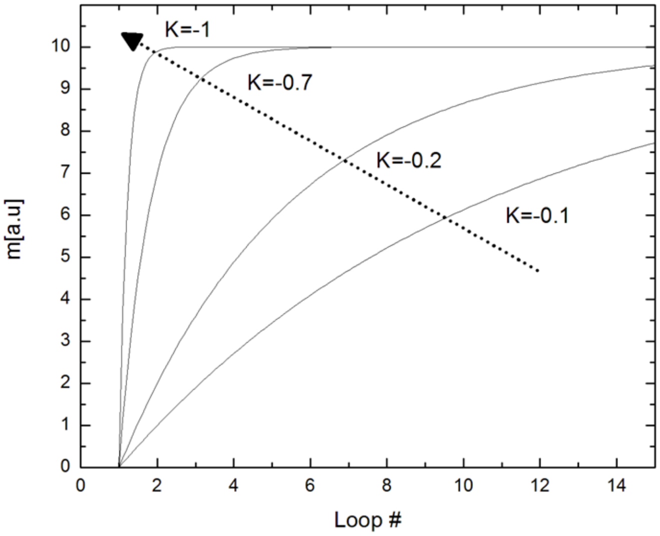

Figure 4.5: Simulated plots of Equation 4.9. Each curve shares an initial and final value, but the value of *K* decreases with the direction of the arrow from -0.1 to -1 to show the transition from continuous to step like behavior. Lines are to guide the eye; the function is only defined on the integers.

The recursive equation 4.7 can be made into an explicit expression for $S(n)$, depending only on the initial value $S(1)$, the final value S_∞, and the constant K.

$$S(n) = (K+1)^{n-1}S(1) - KS_\infty(K+1)^n \sum_{j=2}^{n} \left(\frac{1}{K+1}\right)^j \tag{4.8}$$

Since the boundary magnetization S is proportional to the exchange bias of the ferromagnetic thin film, equation 4.8 leads to an explicit expression of the exchange bias as a function of the loop number *n* of a training series

$$\mu_0 H_B(n) = (K+1)^{n-1}\left\{\mu_0 H_B(1) - K\mu_0 H_B(\infty)\left[\frac{(K+1)^{n+1}-1}{K(K+1)^{n-1}} - (K+2)\right]\right\} \tag{4.9}$$

Figure 4.5 shows this equation simulated for various values of *K* between -0.1 and -1 for one set of arbitrarily chosen values of $H_B(1)$ and $H_B(\infty)$. In addition, the solid line fits in Figure 4.3 (c) are done with this equation. Since the initial and final exchange bias values are experimentally determined, only a single parameter, *K*, is varied in the fit.

In analogy with a ferromagnetic hard layer in a ferromagnetic hard/soft bilayer, we can model the free energy of the antiferromagnetic boundary magnetization using the Landau expansion for a ferromagnet near the Curie temperature

$$F = F_0 + \frac{1}{2}aS^2 + \frac{1}{4}bS^4 - SH \tag{4.10}$$

Then

$$\left.\frac{\partial^2 F}{\partial S^2}\right|_{S=S_\infty} = a + 3bS_\infty^2 \tag{4.11}$$

This can be directly compared to equation 4.6 which shows *K* is proportional to the second derivative of the free energy. Using the fact the equilibrium exchange bias $H_{EB}^{\infty} \propto S_\infty$, it is expected that K and $H_{EB}^{\infty}(E)$ will be related by a simple functional form of the type

$$K = \tilde{a} + \tilde{b}(H_{EB}^{\infty})^2 \tag{4.12}$$

where the extra constants upon substitution have been absorbed into $\tilde{a}$ and $\tilde{b}$ with $\tilde{a} < 0$ and $\tilde{b} > 0$. To take the shift of the $H_{EB}^{\infty}(E)$ hysteresis with respect to zero exchange bias into account the expression for K can be modified into $K = \tilde{a} + \tilde{b}(\,H_{EB}^{\infty}(E) + U)^2$.

Inspection of Figure 4.3 shows that positive and negative saturation values H_{EB}^{max} and $H_{EB}^{min}$of the $H_{EB}^{\infty}(E)$ hysteresis differ in magnitude indicating that exchange bias training is already virtually zero even if full saturation of the boundary magnetization and the antiferromagnetic order parameter is not reached. All of the free parameters in this expression can be eliminated utilizing the constraints $K(H_{EB}^{max}) = K\left(H_{EB}^{min}\right) = 0$ (no training) and $K_{min} = -1$ following from the convergence criterion when deriving the explicit *n*-dependence of Eq. 4.9 from its constituting implicit sequence as outlined in Ref. [128]. The parameter free $K(\ H_{EB}^{\infty}(E))$ function reads finally

$$K = -1 + 4\left(\frac{H_{EB}^{\infty}(E) - \frac{1}{2}(H_{EB}^{max} + H_{EB}^{min})}{H_{EB}^{max} - H_{EB}^{min}}\right)^{2} \qquad (4.13)$$

Figure 4.6 shows the experimental data *K* vs. $H_{EB}^{\infty}(E)$ (squares) and a plot of Eq. 4.13 with values H_{EB}^{max} and H_{EB}^{min} adapted from the solid hysteresis loops shown in Figure 4.3 (a) and (b) and the experimental K values extracted from the fit of Eq. 4.9 to the training data (examples shown in Figure 4.3 (c)). In both cases there is reasonable agreement with the theory confirming the microscopic model of the voltage-controlled EBT as outlined above.

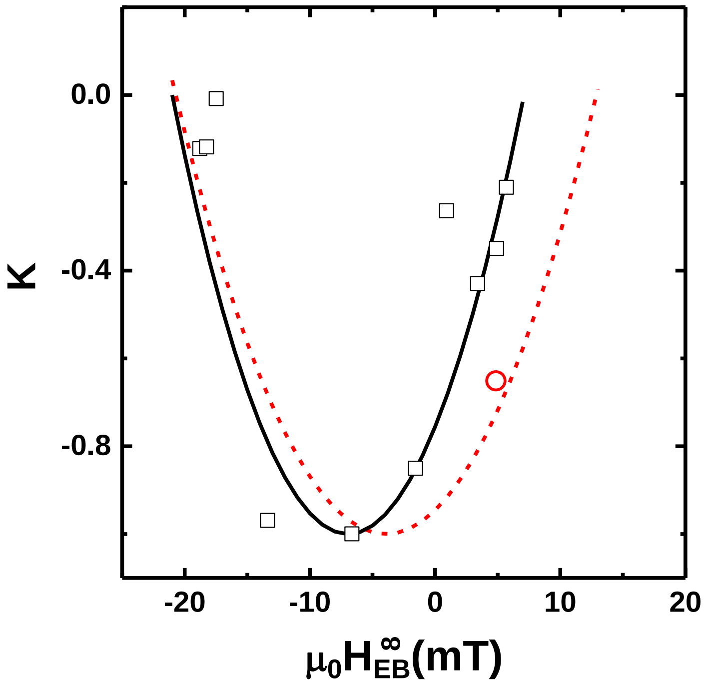

Figure 4.6: K vs. $\mu_0 H_{EB}^{\infty}$ for the training events arising from best fits of Eq. 4.9 to various training series corresponding to the data shown in Figure 4.3. Solid and dashed lines are plots of Eq. 4.13 using $\mu_0 H_{EB}^{min/max}$ from the saturation values in Figure 4.3 (a) and (b).

In conclusion two new phenomena in electrically-controlled magnetism have been introduced. These are the isothermal voltage-control of exchange bias training and the isothermal voltage-controlled gradual tuning of equilibrium exchange bias. The latter phenomenon reflects the isothermal counterpart of the thermally assisted exchange bias tuning via magnetoelectric annealing [130]. In addition it is emphasized that magnetoelectric antiferromagnets provide a simple way to electrically induce first-order reversal of the antiferromagnetic order parameter in the absence of an applied conjugate field.

Chapter 5: Tuning the Effective Anisotropy in a Voltage Susceptible Exchange Bias Heterosystem

In this chapter, Voltage and temperature tuned ferromagnetic hysteresis is investigated in a thin-film heterostructures of a perpendicular anisotropic Co/Pd ferromagnet exchange coupled to the magnetoelectric antiferromagnet chromia. An abrupt disappearance of exchange bias with a simultaneous more than two-fold increase in coercivity is observed and interpreted as a competition between the effective anisotropy of chromia and the exchange coupling energy between boundary magnetization and the adjacent ferromagnet. The effective anisotropy energy is given by the intrinsic anisotropy energy density multiplied by the effective volume separated from the bulk through a horizontal antiferromagnetic domain boundary. Kerr measurements show that the anisotropy of the interfacial chromia can be tuned, isothermally, and in the absence of an external magnetic field, by application of an electric field. A generalized Meiklejohn-Bean model accounts for the change in exchange bias and coercivity as well as the asymmetric evolution of the hysteresis loop. In support of this model, the reversal of the boundary magnetization is experimentally confirmed as a contribution to the magnetic hysteresis loop. These results were published in Physical Review Applied.[131]

Since the pioneering observation of exchange bias in small ferromagnetic Co particles embedded in their native antiferromagnetic oxide, there has been a renewed interest in the investigation of the exchange bias effect.[14, 19] Exchange coupled magnetic layers have played a key role in developing magnetic materials with increased energy product,[132] improved magnetocaloric properties,[133] increased areal storage density,[134] enhanced thermal stability,[135] and have enabled the development of high performance spin valves and magnetoresistive multilayers.[13, 136] Among the proposed devices which use exchange bias for information storage and processing is the ME-MTJ. A crucial parameter of any device which utilizes exchange bias is the maximum temperature at which the exchange bias can be maintained, this is called the blocking temperature. The maximum blocking temperature for an antiferromagnetic/ferromagnetic device is the Néel temperature of the antiferromagnet. Above the Néel temperature, the antiferromagnetic component loses its magnetic order and the ferromagnet is no longer pinned by it, thus the exchange bias disappears. Due to its Néel temperature, a chromia-based ME-MTJ could operate slightly above room temperature, while a boron-doped chromia-based ME-MTJ could operate far above room temperature. Generally it is ideal for an exchange bias device to have the blocking temperature as high as possible, but sometimes a unique temperature dependence of exchange bias arises in chromia-based heterostructures.[137, 138] This temperature dependence causes the exchange bias to abruptly drop to zero far below the Néel temperature. The disappearance of exchange bias more than 100 K below $T_N = 307$ K is detrimental to device applications and thus understanding of this transition is crucial.

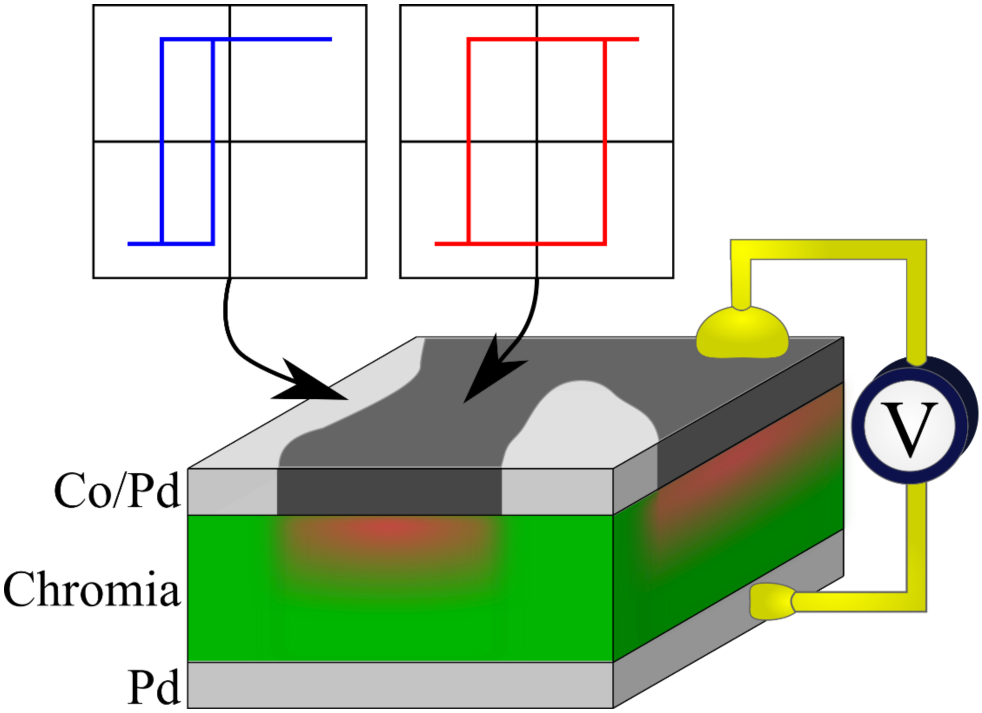

Figure 5.1: Device demonstrating voltage-controlled tuning of effective anisotropy. A chromia layer is sandwiched between two conductive electrodes, a voltage can be applied between the electrodes. The top electrode is a ferromagnetic thin film. Part of the chromia film depicted by an orange gradient rotates with the ferromagnet giving rise to the red hysteresis curve. The green chromia remains fixed giving rise to the blue curve.

As depicted in Figure 5.1, the samples studied consist of a magnetoelectric chromia layer sandwiched between two conductive electrodes which will allow a voltage to be applied across the chromia. The bottom electrode is constructed from a thin film of palladium (111), chosen to allow the subsequent deposition of chromia (0001). The top electrode is composed of a Co/Pd ferromagnetic multilayer, which is exchange coupled with the chromia, giving rise to exchange bias. There are two samples considered. For sample #1, a sapphire substrate is cleaned using modified RCA protocol.[58] The substrate is introduced into an ultra-high vacuum chamber for chromium and palladium to be deposited by Molecular Beam Epitaxy. A 1 nm chromium adhesion layer is grown at 300 C. The palladium is grown according to a three-step-growth process.[102] A seed layer of 7 nm is grown at 650 C. The sample is then cooled to ~50 C and an additional 50 nm of palladium is grown. Finally the temperature is raised to 650 C to crystalize the palladium. This process minimizes the roughness of the final film. The sample is then introduced into a separate vacuum chamber for deposition of chromia by Pulsed Laser Deposition. A KrF excimer laser with pulse energies of 200 mJ and pulse width of 20 ns at a repetition rate of 10 Hz creates a plume from a chromia target, allowing deposition of (0001) textured chromia thin films on top of the palladium. The temperature of the substrate is maintained at 500 C while a total of 500 nm is deposited. Finally a perpendicular ferromagnetic film of Pd (1 nm)+[Co (0.6 nm)/Pd (1 nm)]$_2$ is deposited by Molecular Beam Epitaxy while the sample is maintained at a temperature of 300 C. Sample #2 is likewise prepared, except on the final step a shadow mask is applied to the sample, restricting the Co/Pd deposition to 300 μm^2 region.

The hysteresis loops for sample #1 are measured using a superconducting quantum interference device (SQUID). Figure 5.2 shows the evolution of the ferromagnetic hysteresis loops and the associated exchange bias effects as a function of temperature. The initial sample state has been prepared via a field cooling from T=330 K to T=170 K in B=1 T applied normal to the film, i.e., along the easy axes of both the ferromagnet and antiferromagnet. Below 180 K the hysteresis is fully shifted to the left, with both the zero magnetization point of the descending branch (H_{C1}) and ascending branch (H_{C2}), having negative values. As the sample is heated, the ascending branch of the hysteresis loop undergoes a notable change. When applying the standard definition of the exchange bias field according to $\mu_0 H_{EB} = \mu_0(H_{C1} + H_{C2})/2$, the exchange bias decreases from nearly 200 mT at T=180 K to zero at T=200 K. This evolution is localized to the ascending branch of the hysteresis loop. The inset in Figure 5.2 shows the relative magnetization (M/ M_s^+ = Magnetization/Positive Saturation Magnetization), at 93mT (dotted line in the main figure) during the ascending branch of the hysteresis loop.

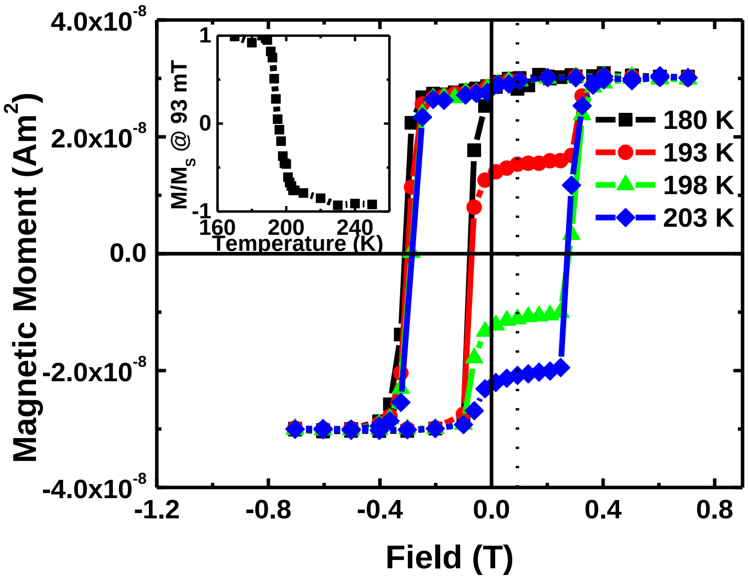

Figure 5.2: Hysteresis loops of the magnetization of perpendicular anisotropic Co/Pd for temperatures 180 (squares), 193 (circles), 198 (triangles) and 203 K (diamonds). Diamagnetic background from the substrate has been subtracted. Inset: Relative magnetization (M/M_S^+= Magnetization/Positive Saturation Magnetization), at 93mT (dotted line in the main figure) during the ascending branch of the hysteresis loop.

Figure 5.3 shows the absolute value of exchange bias as a function of temperature and the coercive field, $\mu_0 H_c = \mu_0 |H_{C2} - H_{C1}|/2$. The coercive field jumps up dramatically just as the exchange bias goes to zero. The jump in both exchange bias and coercivity corresponds to the temperature at which the step in the ascending branch of the hysteresis loop descends below the zero magnetic moment axis. Note that this behavior is in strong contrast to most ordinary exchange bias systems in which the coercivity typically increases below the blocking temperature.[12] It will be shown that the unusual increase in coercivity at the blocking temperature is a strong indication for dragging of boundary magnetization on reversal of the ferromagnet.

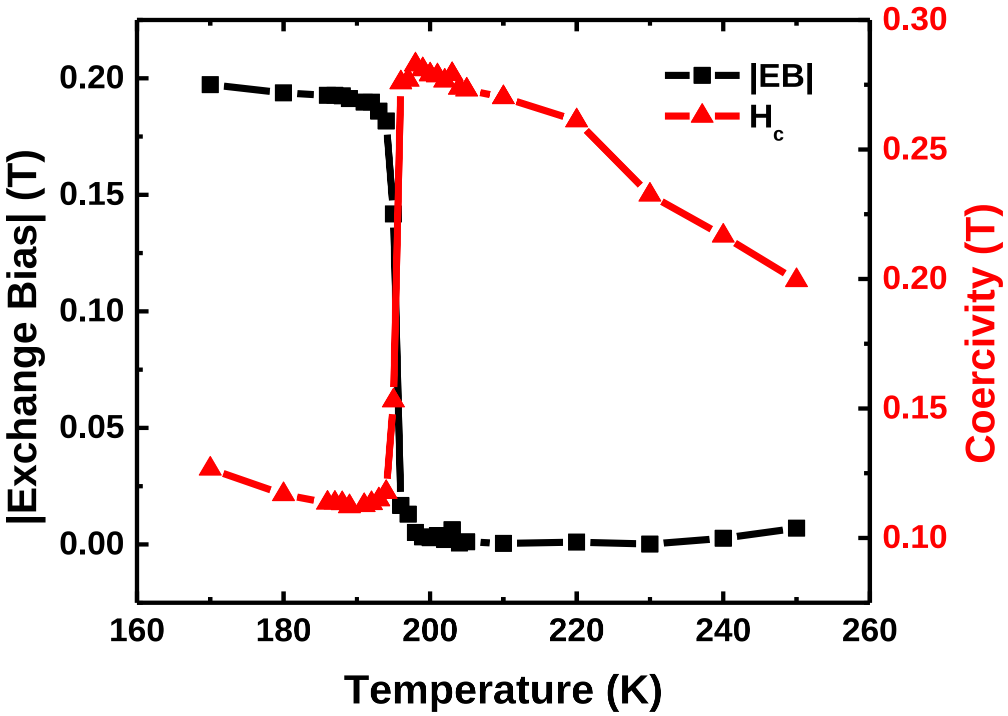

Figure 5.3: Absolute value of the hysteresis loop's exchange bias (squares) and coercivity (circles). Coercive fields have been determined from interception with the magnetic field axis.

The disappearance of exchange bias, doubling of coercivity, and apparent asymmetric evolution of the hysteresis loop can be understood by applying a coherent rotation model to the antiferromagnetic-ferromagnetic interface. In such a system, one can write the free energy per area as:[14, 22, 139]

$$F = -\mu_0 H M_{FM} t_{FM} \cos(\beta) - \mu_0 H M_{AF} t_{AF} \cos(\alpha) \\ + K_{FM} t_{FM} sin^2(\beta) + K_{AF} t_{AF} sin^2(\alpha) \\ - J S_{FM} S_{AF} \cos(\beta - \alpha) \tag{5.1}$$

where M_{FM}, M_{AF}, t_{FM}, t_{AF}, K_{FM}, K_{AF} are the magnetizations, thicknesses, and anisotropy constants of the ferromagnet and antiferromagnet, respectively. S_{FM} and S_{AF} are the interface magnetizations of the ferromagnet and antiferromagnet, while J is the exchange constant which describes the coupling between them. β and α are the angles of the ferromagnetic and antiferromagnetic magnetizations, both interface and bulk, with respect to the uniaxial anisotropy easy axis which is aligned along the film normal.

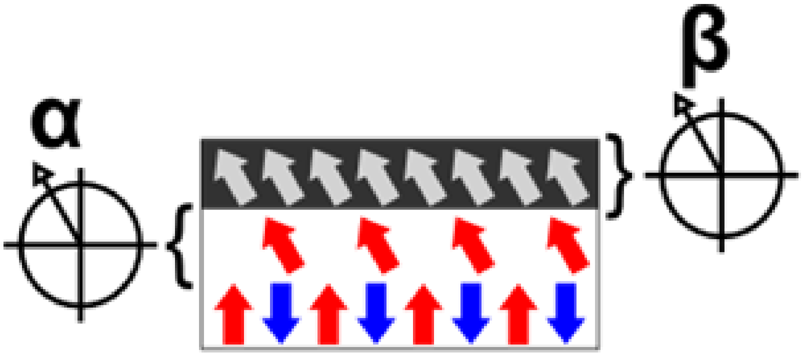

Figure 5.4: Sketch of the angles α and β. β characterizes the ferromagnet while α characterizes the antiferromagnet. It is found that an antiferromagnetic region near the interface can sometimes rotate with the ferromagnet.

Of particular interest is the behavior of the system around minima of the free energy. At these points, near equilibrium, the behavior of the antiferromagnetic interface magnetization can be ascertained using:[14, 22]

$$\begin{aligned}\frac{\partial F}{\partial \alpha} = 0 &= \mu_0 H M_{AF} t_{AF} \sin(\alpha) + 2K_{AF} t_{AF} \sin\alpha \cos\alpha \\ &\quad - J S_{FM} S_{AF} \sin(\beta - \alpha) \\ &\approx 2K_{AF} t_{AF} \sin\alpha \cos\alpha - J S_{FM} S_{AF} \sin(\beta - \alpha)\end{aligned} \tag{5.2}$$

Here the term containing M_{AF} is negligibly small as demonstrated later. As Meiklejohn points out, exchange bias can only arise if the anisotropy energy of the antiferromagnet is large compared to the exchange field.[14] Exchange bias occurs when the antiferromagnetic layer exerts a unidirectional microscopic torque on the adjacent ferromagnet, making one orientation of the ferromagnet energetically preferable over the other. This unidirectionality comes from the fact that the antiferromagnetic spins at the interface remain fixed as the ferromagnet rotates in an applied magnetic field. The necessary condition can be derived from the required stationary behavior of the antiferromagnet by assuming $\alpha \ll \beta$. Then equation 5.2 simplifies to:

$$\frac{\partial F}{\partial \alpha} = 0 = 2K_{AF} t_{AF} \sin\alpha - J S_{FM} S_{AF} \sin(\beta) \tag{5.3}$$

Then,

$$\sin\alpha = \frac{J S_{FM} S_{AF} \sin(\beta)}{2K_{AF} t_{AF}} \tag{5.4}$$

To ensure the antiferromagnetic spins do not reverse along with the ferromagnetic spins requires that $1 < \sin\alpha \leq 0$, for all values of β. Using the high end of this requirement as the maximum allowable deviation yields:

$$\frac{JS_{FM}S_{AF}\sin(\beta)}{2K_{AF}t_{AF}} < 1 \; \forall \; \beta \tag{5.5}$$

or

$$\frac{JS_{FM}S_{AF}\sin(\beta)}{2} < K_{AF}t_{AF}^{c} \tag{5.6}$$

Where t_{AF} is replaced by t_{AF}^{c}, as the critical thickness, the minimum thickness which will cause exchange bias to arise. When the "Meiklejohn criterion" of equation 5.6 is met, exchange bias is present, if it is not met exchange bias is absent because the exchange field causes the antiferromagnetic spins reverse along with the ferromagnetic spins. The crossover between this criterion being met and not being met is what causes the sudden disappearance of exchange bias.

The behavior of the ferromagnet in both cases, when the Meiklejohn criterion is met, and when it is not, can be ascertained by again studying the free energy. The extrema of the free energy with respect to the orientation of the ferromagnetic magnetization can be found by solving $\partial F/\partial\beta = 0$.

$$\frac{\partial F}{\partial \beta} = 0 = \mu_0 H M_{FM} t_{FM} \sin\beta + 2K_{FM}t_{FM}\sin\beta\cos\beta + JS_{FM}S_{AF}\sin(\beta - \alpha) \tag{5.7}$$

First, let's consider the case when $K_{AF}t_{AF} \gg JS_{FM}S_{AF}$. In this case the large antiferromagnetic anisotropy causes all spins of the antiferromagnet to remain parallel to the c-axis, that is $\alpha \approx 0$. Therefore in the limit of high anisotropy of the antiferromagnet $\frac{\partial F}{\partial \beta} = 0$ can be simplified into

$$\frac{\partial F}{\partial \beta} = 0 = \mu_0 H M_{FM} t_{FM} \sin\beta + 2K_{FM} t_{FM} \sin\beta \cos\beta + J S_{FM} S_{AF} \sin(\beta) \tag{5.8}$$

which yields

$$\cos\beta = -\frac{\mu_0 H M_{FM} t_{FM} + J S_{FM} S_{AF}}{2K_{FM} t_{FM}} \tag{5.9}$$

Substituting this into

$$\frac{\partial^2 F}{\partial \beta^2} = \mu_0 H M_{FM} t_{FM} \cos\beta + 2K_{FM} t_{FM} (2\cos^2\beta - 1) + J S_{FM} S_{AF} \cos\beta \tag{5.10}$$

provides an expression for the curvature of the free energy. Switching of the magnetization happens when a local minimum becomes unstable such that the free energy has a horizontal tangent according to $\frac{\partial^2 F}{\partial \beta^2} = 0$. This condition yields

$$-\frac{\mu_0 H M_{FM} t_{FM} (\mu_0 H M_{FM} t_{FM} + J S_{FM} S_{AF})}{2K_{FM} t_{FM}} + 2K_{FM} t_{FM} \left(\frac{(\mu_0 H M_{FM} t_{FM} + J S_{FM} S_{AF})^2}{2(K_{FM} t_{FM})^2} - 1 \right) - J S_{FM} S_{AF} \frac{\mu_0 H M_{FM} t_{FM} + J S_{FM} S_{AF}}{2K_{FM} t_{FM}} = 0 \tag{5.11}$$

Defining $h{:}= \mu_0 H M_{FM} t_{FM}$, $j{:}= J S_{FM} S_{AF}$, and $k \coloneqq 2K_{FM} t_{FM}$

$$-\frac{h^2 + jh}{k} + k\left(\frac{2(h+j)^2}{k^2} - 1 \right) - j\frac{h+j}{k} = 0 \tag{5.11}$$

$$h^2 + 2hj + j^2 - k^2 = 0$$

With solutions $h = -j \pm k$ providing the well-known Meiklejohn-Bean expression for exchange bias, $\mu_0 H_{EB} = -\frac{JS_{FM}S_{AF}}{M_{FM}t_{FM}}$ from the coercivities:

$$\mu_0 H_{c1} = \frac{-2K_{FM}t_{FM} - JS_{FM}S_{AF}}{M_{FM}t_{FM}} \quad \mu_0 H_{c2} = \frac{2K_{FM}t_{FM} - JS_{FM}S_{AF}}{M_{FM}t_{FM}} \tag{5.12}$$

However, if instead it is assumed that the anisotropy of the antiferromagnet is small, the exchange between the ferromagnet and antiferromagnet interface magnetization is large enough to couple them together so that the spins of both the ferromagnet and the antiferromagnet coherently rotate in the external magnetic field. In this limit, where $\alpha = \beta$, the free energy simplifies as:

$$\begin{aligned} F^* = -\mu_0 H M_{FM} t_{FM} \cos(\beta) - \mu_0 H M_{AF} t_{AF} \cos(\beta) \\ + K_{FM} t_{FM} sin^2(\beta) + K_{AF} t_{AF} sin^2(\beta) - JS_{FM}S_{AF} \end{aligned} \tag{5.13}$$

Using the same procedure as above one obtains $\mu_0 H_{EB} = 0$ from the coercive fields

$$\mu_0 H_{c1}^* = -\frac{2(K_{FM}t_{FM} + K_{AF}t_{AF})}{(M_{FM}t_{FM} + M_{AF}t_{AF})} \quad \mu_0 H_{c2}^* = +\frac{2(K_{FM}t_{FM} + K_{AF}t_{AF})}{(M_{FM}t_{FM} + M_{AF}t_{AF})} \tag{5.14}$$

For temperatures below 180 K the data shown in Figure 5.3 imply that the former condition of Eq. (5.12) is approximately satisfied, and the boundary magnetization remains fixed. For temperatures above 220K the latter condition of Eq. (5.14) is satisfied, and the boundary magnetization rotates with the ferromagnet.

In the present case the chromia film is 500 nm thick, far above the minimum critical thickness necessary for exchange bias. Exchange bias has been observed for chromia/ferromagnet heterostructures for chromia thicknesses as small as 20 nm.[140] Therefore, implicit in the assumption that the boundary magnetization rotates along with the ferromagnet is that the boundary magnetization becomes incommensurate with the underlying spin structure of the chromia by forming a horizontal domain wall. Dramatic changes in the exchange bias and coercivity due to domain wall formation at the interface have been previously proposed.[137, 138, 141-143] In addition a boundary magnetization in chromia which is incommensurate with the domain state of the chromia has previously been used to describe electrically-controlled exchange bias training, as in Chapter 4.

The above discussion suggests that a surplus moment originating from the boundary magnetization contributes to the saturation magnetization of the ferromagnetic hysteresis for temperatures above 180 K. In fact, the expected additional magnetic moment of the interface magnetization of the boundary magnetization rotating with the ferromagnet is evidenced by measuring the total change in magnetic moment (Δm) from positive magnetic saturation to negative magnetic saturation. Figure 5.5 shows Δm as a function of temperature. In exactly the same temperature region in which the hysteresis loop changes from negative exchange bias to zero exchange bias (vertical lines in Figure 5.5), the total Δm reverses the downward trend with increasing temperature as the additional magnetic moment of the chromia interface spins begin to reverse with the ferromagnet. Figure 5.5 shows the additional change in magnetic moment due to the reversal of the boundary magnetization is approximately 7.5×10^{-10} Am^2, one half of this value is the total magnetic moment of the boundary magnetization (m_{AF}). So $M_{AF}t_{AF}^{c} = m_{AF}t_{AF}^{c}/(Area * t_{AF}^{c})$, the area of the sample is 1.51×10^{-5} m^2, so $M_{AF}t_{AF}^{c} = 2.5 \times 10^{-5}$ A. Likewise $M_{FM}t_{FM} = 2.0 \times 10^{-2}$ A. Therefore the following approximation is justified.

$$M_{FM}t_{FM} \gg M_{AF}t_{AF}^{c} \tag{5.15}$$

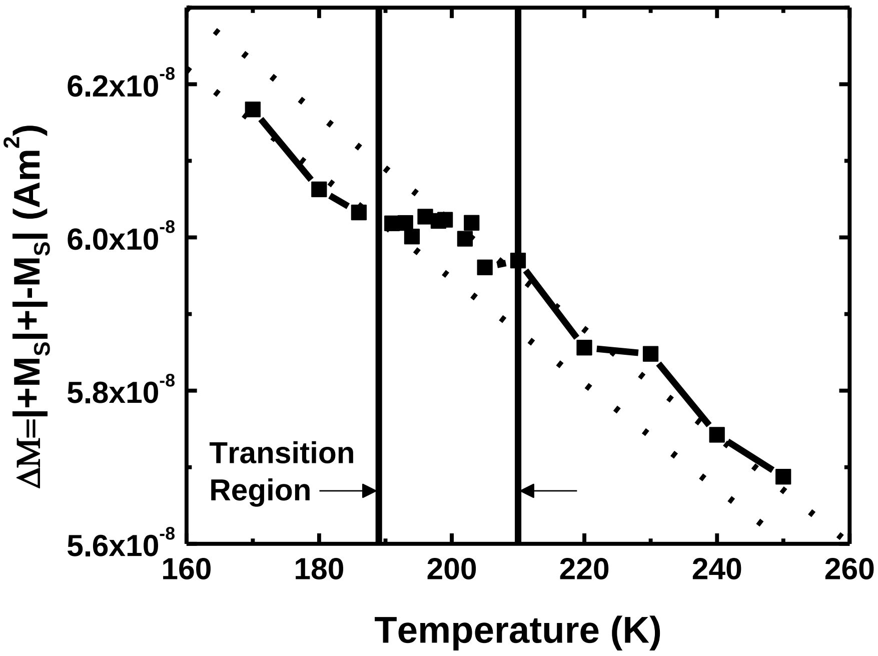

Figure 5.5: Total change in the magnetic moment between positive and negative saturation magnetization as a function of the temperature. The transition region is marked. Dotted lines are to guide the eye.

At the onset of this depinning effect the system is transitioning from a region where $JS_{FM}S_{AF}/2 < K_{AF}t_{AF}^{c}$, to a region where $JS_{FM}S_{AF}/2 > K_{AF}t_{AF}^{c}$, therefore it is natural to apply the condition

$$K_{AF}t_{AF}^{c} = \frac{JS_{AF}S_{FM}}{2} \tag{5.16}$$

Here t_{AF}^{c} is the thickness of the chromia domain at the interface which reverses with the ferromagnet. In contrast to the simple Meiklejohn Bean model where domains are not considered, here, t_{AF}^{c} is given by the temperature dependent effective thickness of the horizontal antiferromagnetic domain rather than the geometrical film thickness. The effective anisotropy energy per area, $K_{AF}t_{AF}^{c}$, is the intrinsic anisotropy energy density, K_{AF}, multiplied by the effective critical thickness, t_{AF}^{c}, determined by the distance between the interface and the horizontal antiferromagnetic domain boundary parallel to the interface.

Before the transition, the coercive field for the descending branch of the hysteresis is given by $\mu_0 H_{c1} = \frac{-2K_{FM}t_{FM} - JS_{FM}S_{AF}}{M_{FM}t_{FM}}$, after the transition, using $K_{AF}t_{AF}^{c} = JS_{FM}S_{AF}/2$, the coercive field is $\mu_0 H_{c1}^{*} = \frac{-2K_{FM}t_{FM} - JS_{FM}S_{AF}}{(M_{FM}t_{FM} + M_{AF}t_{AF})}$. Note here, that the experimental data of Figure 5.2, shows no change in the coercive field values of the descending branch. This further verifies Eq. 5.15, since no transition is present, the additional term, $M_{AF}t_{AF}$, in the denominator of $\mu_0 H_{c1}^{*}$, must be inconsequential.

Using Equation 5.14, along with the conditions $K_{AF}t_{AF}^{c} = JS_{FM}S_{AF}/2$ and $M_{FM}t_{FM} \gg M_{AF}t_{AF}^{c}$, the coercivities of the hysteresis loop in the regime of boundary magnetization rotation simplify to

$$\mu_0 H_{c1}^{*} \approx \frac{-2K_{FM}t_{FM} - JS_{AF}S_{FM}}{(M_{FM}t_{FM})} \quad \mu_0 H_{c2}^{*} \approx +\frac{2K_{FM}t_{FM} + JS_{AF}S_{FM}}{(M_{FM}t_{FM})} \tag{5.17}$$

There are two things of note here. First $\mu_0 H_{c1}^{*} = -\mu_0 H_{c2}^{*}$, which is the definition of a hysteresis with zero exchange bias. Second $\mu_0 H_{c1}^{*} = \mu_0 H_{c1}$, while $\mu_0 H_{c2}^{*} \neq \mu_0 H_{c2}$, which explains the increase of the coercivity from $\mu_0 H_{c} = \frac{2K_{FM}t_{FM}}{M_{FM}t_{FM}}$ to $\mu_0 H_{c}^{*} = \frac{2K_{FM}t_{FM} + JS_{AF}S_{FM}}{(M_{FM}t_{FM})}$ solely due to change in the coercive field of the ascending branch.

Finally, the effective anisotropy of the chromium oxide can be altered isothermally by the application of electric and magnetic fields. As previously shown, by applying electric and magnetic fields across chromia one of two degenerate 180° antiferromagnetic domains can be selected isothermally.[37, 44, 47, 48] The magneto-optic

Kerr effect was used to examine the effect of an applied electric field on the hysteresis of sample #2.[88] Figure 5.6 (a) shows the hysteresis loop of sample #2 at 295 K immediately after -12 V (squares), 0 V (triangles), and +12 V (circles) is applied simultaneously with -829 mT magnetic field for approximately 1s. In Figure 5.6 (b) the active portion of the loop is shown in more detail. The small step in the hysteresis shows that in some area of the sample the chromia does not rotate with the ferromagnet, and causes exchange bias. In most areas the sample is unpinned and the chromia rotates with the ferromagnet. Those areas which are pinned show negative exchange bias. A chromia/ferromagnet heterostructure which exhibits negative exchange bias can be isothermally switched to positive exchange bias by applying a large enough positive field product. The squares in Figure 5.6 (b), show the result immediately after pulsing the positive field product of -829 mT and -12 V. The field was not sufficient to create positive exchange bias, but it did destabilize those areas which are pinned to a negative exchange bias. By reversing the electric field, the effect is reversed. The circles in Figure 5.6 (b) show the effect after pulsing +12 V and -829 mT. This causes some chromia domains which, prior to field exposure, rotate with the ferromagnet to no longer rotate. This increase in the antiferromagnetic domain volume partially reinforces pinning of the ferromagnet and thus raises the step in the ascending branch. It should be noted that the effect is not persistent, after one reversal of the ferromagnet, the hysteresis loop reverts to its original state before any electric fields were applied.

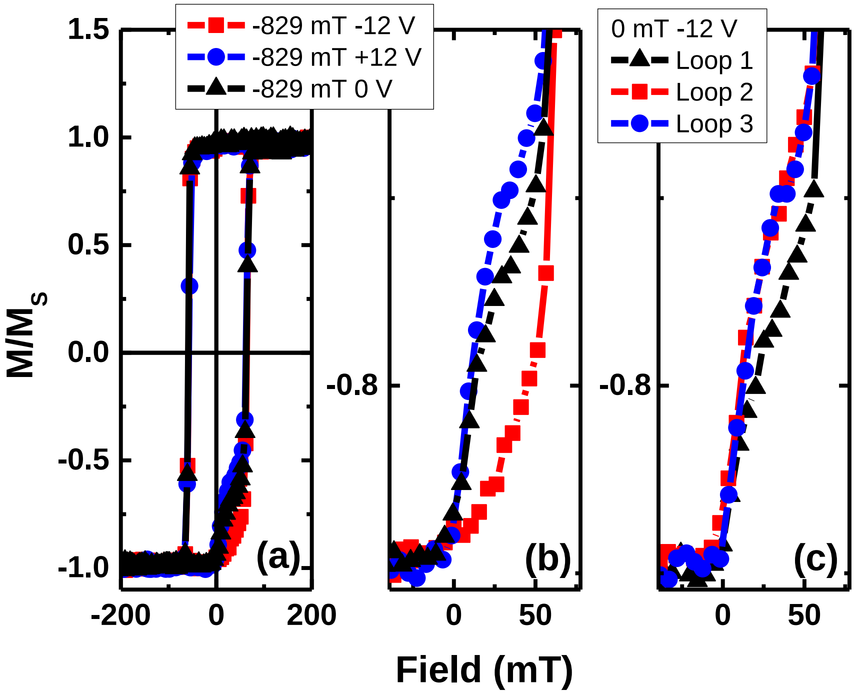

Figure 5.6: a) Hysteresis of Sample #2 at 295K after -829 mT and +12V, 0V, and -12V pulse, b) detail of the active region shown in a), c) Detail of active region after 0 mT and -12V is pulsed

It is possible to trigger this effect even without an external magnetic field. The active region in the chromia in this case is just below the interface to a depth of the critical thickness. In this region the exchange field from the adjacent ferromagnet acts as an effective magnetic field. In Figure 5.6 (c) -12 V is pulsed with zero external magnetic field, while a negative remnant magnetization is maintained for the ferromagnet. The triangles show the hysteresis loop immediately after pulsing the electric field. The voltage pulse alone also has a destabilizing effect on those areas which remain pinned, moving the step in the hysteresis loop lower. Figure 5.6 (c) also shows the effect is not persistent, as the second (squares) and the third (circles) loop after the pulse is applied return to its pre-pulse state. This finding has encouraging implications for the operation of magnetoelectric device where an external magnetic field would be too cumbersome to apply. The results of Figure 5.6 imply that within a certain penetration depth the exchange field of an adjacent ferromagnet mimics an applied magnetic field, unlocking fully voltage-controlled switching of magnetization with the assistance of a permanent magnet. This interpretation has subsequently been given theoretical support. Udalov and Fraerman have found that near a ferromagnetic interface where there is strong exchange interaction the antiferromagnetic vector near the surface can tilt relative to the anisotropy axis toward the perpendicular orientation.[144] This reorientation takes place within the width of a domain wall from the interface and causes the disappearance of the exchange bias. It is found that within this region the application of an electric field can rotate the antiferromagnetic vector by more than $\pi/2$. Moreover, if the total thickness of the film is less that of a domain wall, it is theorized, the antiferromagnetic order parameter for the entire film can be switched by electrical field only.[144] A device concept has already been proposed which employs this mechanism for magnetoelectric switching at technologically interesting densities.[145] Domain wall dynamics in chromia then become important in terms of switching speeds of such a device. It is found that the domain wall mobility has a maximum as a function of the applied electric field, this maximum is reached at $E = 0.06$ V/nm, where a mobility of 0.1 m/(s Oe) is achieved.[146] But both the maximum mobility and requisite electric field to achieve it can be modified by strain[146] and the exchange field modified by tuning the fabrication of the device. Conventional isothermal magnetoelectric switching of chromia has already been achieve with applied electric fields of ~0.1 V/nm.[147]

In conclusion, it has been shown that an effective anisotropy energy can be tuned by electrical means in the magnetoelectric antiferromagnet chromia. Effective anisotropy is the result of voltage-dependent formation of horizontal domains in proximity of the interface between chromia and an adjacent exchange coupled ferromagnet. It is argued that the abrupt disappearing of exchange bias of the ferromagnetic layer sets in when the horizontal domain thickness is less than the critical thickness for pinning. At this point, chromia's boundary magnetization reverses in concert with the magnetization reversal of the exchange coupled ferromagnet. The lack of pinning due to subcritical effective anisotropy energy of the antiferromagnet also explains, in the framework of a generalized Meiklejohn Bean model, the more than two-fold increase of the coercivity at the transition. These results may have important implications for the optimization of voltage-controlled exchange bias heterostructures which are the building block for energy efficient memory and logic device applications.

Chapter 6: Increasing the Néel Temperature of Magnetoelectric Chromia for Voltage-Controlled Spintronics

In this chapter, boron doping of chromia thin films is addressed. Boron doping is done by pulsed laser deposition of chromia in a decaborane ($B_{10}H_{14}$) atmosphere. Subsequent magnetometry measurements indicate that the Néel temperature of the chromia is increased, which is consistent with first-principles calculations of the effects of substitutional doping. Spin resolved inverse photoemission reveals that the magnetoelectricity of B-doped chromia is preserved above the undoped Néel temperature. This result makes the operation of voltage-controlled spintronics feasible in above room temperature conditions. These results were published in Applied Physics Letters.[148]

Magnetoelectric antiferromagnets have an electrically controllable boundary magnetization which can be exploited to create ultra-low power spintronic devices. This property is maintained up to the Néel temperature of the material above which time inversion symmetry is reestablished and the linear magnetoelectric effect is ruled out by symmetry constraints. Chromia is a magnetoelectric antiferromagnet with a Néel temperature slightly above room temperature ($T_N = 307\ K$), and for this reason it is a particularly promising candidate for spintronic devices. While chromia is suitable for room temperature operation, integration into existing technologies would require any chromia-based spintronic device to operate well above room temperature. It is therefore desirable to increase the Néel temperature of chromia to provide the flexibility necessary for practical applications.

There are two prominent approaches to engineer an increase in the Néel temperature of chromia, the first of which is introducing strain. Strain may be able to increase the Néel temperature of chromia by increasing the orbital overlap between neighboring Cr^{3+} ions, therefore increasing the intralayer antiferromagnetic exchange. Indeed it has been calculated that a 5% increase of c/a (lattice parameters) leads to a 20% enhancement of T_N.[149] While promising, increasing the Néel temperature by strain has a few drawbacks. One method to introduce strain is through lattice mismatch with a neighboring film or substrate. For example, it was shown that large strains can be created in chromia nanoparticles imprisoned in a single crystalline dielectric matrix of MgO.[150] However, creating strain in this way requires strict control of the epitaxy, as the elastic relaxation at the dot edges often yield an exponential relaxation of stress with increasing layer thickness.[150] In general, strict epitaxial requirements are not favorable for device applications. Alternatively, strain can be produced in thin film materials deposited on piezoelectric substrates such as $LiNbO_3$.[151] Strain can be generated by applying rf voltage at the resonance frequency of inter-digitated metallic electrodes creating a surface acoustic wave. The device can be fabricated so that these surface acoustic waves can deliver large strains at frequencies in the GHz range.[152] The strain generated this way can be coupled to an adjacent chromia film giving rise to changes in the Néel temperature. This approach has the advantage of electrical control, and low power consumption, but has the disadvantages of relatively low packing densities and slightly inferior switching speeds to their best semiconductor counterparts.[153]

The second prominent approach to increasing the Néel temperature of chromia is by doping. It has been shown that substitution of boron on the oxygen sites of chromia can increase the exchange energies between neighboring Cr spins and thus increase the antiferromagnetic ordering temperature.[148, 154, 155] Boron substituting oxygen introduce impurity states which cause strong hybridization between nearby Cr ions and strengthen ferromagnetic coupling between those Cr sites with the same spin orientation. This interaction is superimposed on the existing antiferromagnetic order, and thanks to the favorable hybridization geometry in the ground state this ferromagnetic coupling reinforces the anti-ferromagnetic order and enhances the exchange energies, thus increasing the antiferromagnetic ordering temperature.[154] The calculations show each B atom enhances the exchange energy on its four Cr neighbors by a factor of 2 to 3 and that substitutional boron doping of chromia can increase T_N by roughly 10% per 1% O site substitution with B.

Following this theoretical guidance, boron doped chromia thin films were fabricated. Sublimated decaborane has been shown to be valuable for doping semiconductor materials with boron.[76, 77] Al_2O_3 (0001) substrates were used, which are known to facilitate the growth of (0001) textured chromia films. Deposition was done by pulsed laser deposition in a background vapor pressure of decaborane as described in Chapter 2. The decaborane pressure was maintained at values ranging from $7.5 \times 10^{-8} - 1.0 \times 10^{-6}$ millibars resulting in doping levels between 0-3% as determined from core level photoemission. A KrF eximer laser with pulse energies of 200 mJ at a repetition rate of 10 Hz was used to ablate a chromia target causing film deposition on the sample. The substrate itself was held at 700° C during deposition, which is above the temperature of complete thermal dissociation of decaborane.[77]

Boron substitution on the oxygen site in films grown in this manner was subsequently confirmed by electron energy loss spectroscopy (EELS). EELS is highly sensitive to the nature of chemical bonds present in a sample and has been used to acquire elemental maps of thin film heterostructures to a nanometer resolution.[156] By comparing the EELS measurement on boron doped chromia to the simulated EELS result arising from the possible dopant locations, the existence of BCr_4 structures were experimentally confirmed.[157] It was found that 12%-43% of the B dopants took their place inside the BCr_4 tetrahedra which were shown to increase the Néel temperature, while the remainder occupied other sites.[157]

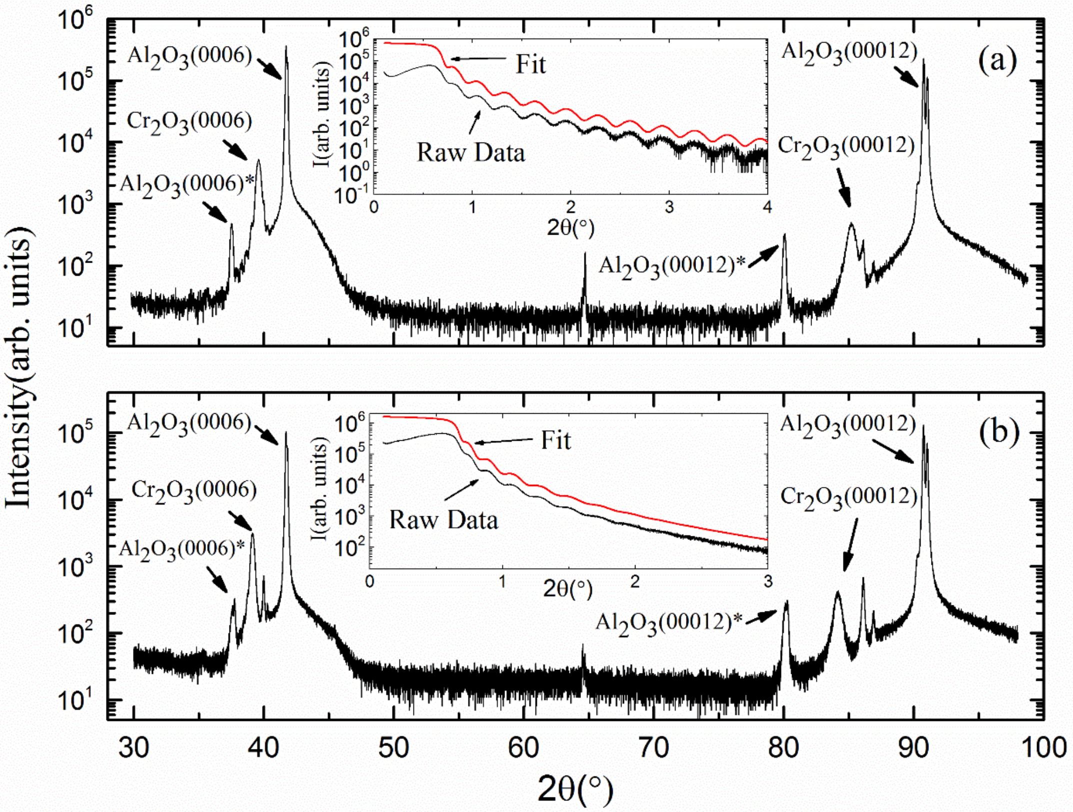

Figure 6.1: Wide and small angle x-ray diffraction of pure (a) and B-doped (b) chromia thin films. Narrow (0006) and (00012) Kα peaks indicate (0001) textured chromia. (*) indicates Kβ peaks. Inset of (a) shows small angle x-ray

diffraction raw data and best fit (shifted for clarity relative to raw data) determining a film thickness of 26.3 nm and roughness of 0.22 nm. Panel (b) and inset show the corresponding data for 3% B-doped chromia thin film. The 0006 and 00012 chromia peaks are shifted -0.4˚ with respect to the pure film. Fit of x-ray small angle diffraction data reveals a film thickness of 35.5 nm with roughness of 0.26 nm.

Samples were structurally characterized using x-ray diffraction and reflectivity. The primary wavelength used in diffraction was that of Cu K-α = 0.154056 nm but additional peaks are also present from the Cu K-β wavelength. Figure 6.1 (a) and 6.1 (b) show the structural characterization of our films through wide angle θ-2θ x-ray diffraction patterns of undoped (Figure 6.1 (a)) and approximately 3% B-doped (Figure 6.1 (b)) chromia. Note here the similarity between the two data sets indicate that the texture of the film is largely unchanged with doping levels of up to 3%. Both films are (0001)-textured as indicated by the narrow (0006) and (00012) Bragg-peaks. The insets show the respective small angle x-ray diffraction images allowing to determine the film thicknesses of the undoped and B-doped films to 26.3 nm and 35.5 nm with roughness of 0.22 nm and 0.26 nm, respectively.

To determine the Néel temperature of the films SQUID magnetometry was employed. Samples were field-cooled from 400 K to 200 K in an applied magnetic field of 7 T applied normal to the film. It has been shown in chromia thin-films that the magnetic field alone is sufficient to select a single domain state.[116] This is possible because in a thin-film geometry the Zeeman energy of the interfacial spins make a sizable contribution to the total magnetic energy in the film. Due to the intimate connection of the interfacial magnetization and the antiferromagnetic domain state, the applied magnetic field preferentially selects one of the two antiferromagnetic single domain ground states. Below the Néel temperature the spin structure of chromia is locked in even after removing the applied magnetic field. Moreover, a small but measurable magnetic moment remains which is indicative of the antiferromagnetic order parameter.[116] In the simplest of cases, this remaining moment corresponds to the boundary magnetization, but recently it has been shown that in the case of thin-films, both doped and undoped, columnar grain boundaries are responsible for most of the uncompensated spins in the sample.[158]

Due to the weakness of the magnetic signal, it is necessary to eliminate any background signal caused by the magnetic susceptibility of the substrate. To suppress any erroneous signals, measurements were taken in zero magnetic field conditions. Immediately before measurement, true zero-field conditions were obtained by slightly heating the magnetic coils above their superconducting transition temperatures, thus quenching any residual trapped flux. The magnetization of the film is then measured as a function of temperature while heating from 200 K to 400 K. As the magnetization of the sample is strictly tied to the antiferromagnetic order parameter, the temperature at which the magnetization disappears corresponds to the Néel temperature.

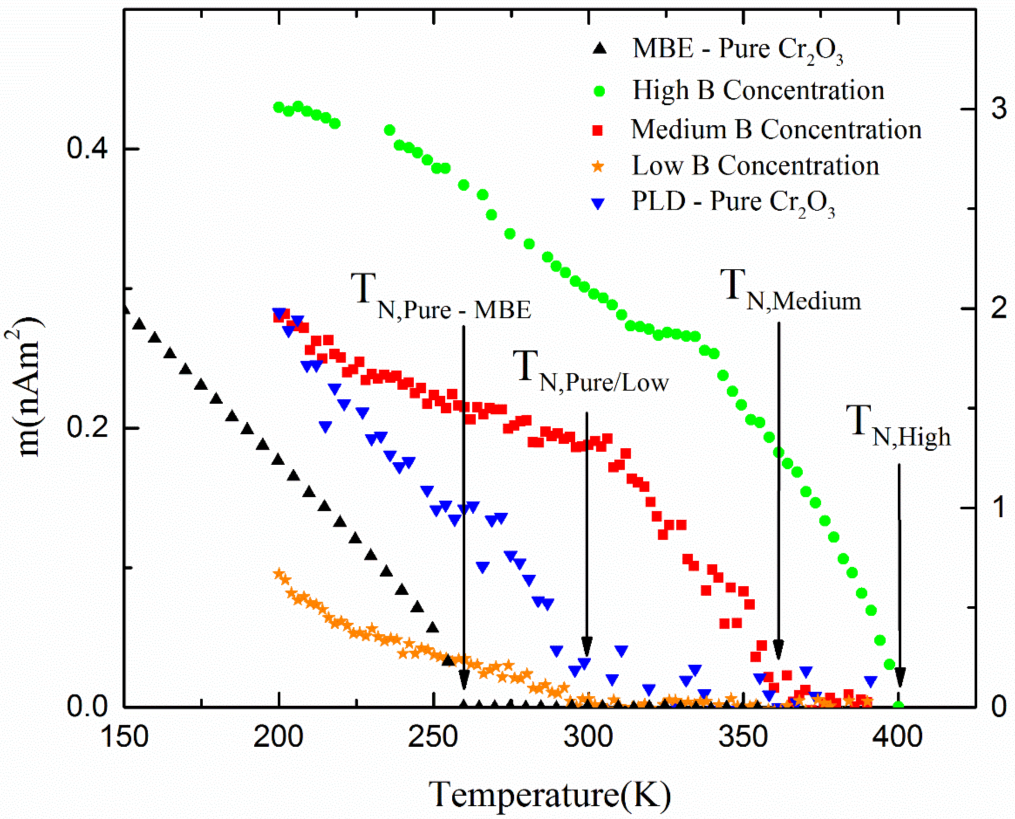

Figure 6.2: Magnetic moment, m, versus temperature measured on heating in zero applied field for PLD grown films of pure chromia (down triangles) and B concentrations from <1% (stars) to ~2% (squares) to ~3% (circles). Samples were field-cooled in the presence of 7 T normal to the film from 400 K to 200 K. Up triangles show reference zero-field heating data for a pure chromia film of 100 nm thickness grown by molecular beam epitaxy.

Figure 6.2 shows the result of the zero-field measurement. It is seen that chromia doped with increasing concentrations of boron (<1%, 2%, 3%) show increasing Néel temperatures (300 K, 360 K, and 400 K respectively). These results are largely in-line with the theoretical predictions.[154] Also shown are two reference undoped samples, one grown by pulsed laser deposition for direct comparison and one grown by molecular beam epitaxy which was previously characterized.[159] The MBE grown film in particular has a significantly lower Néel temperature which can likely be attributed to oxygen vacancies or other defects likely to occur in epitaxial growth in a reactive oxygen atmosphere.[160] The data suggest that these deficiencies are largely avoided using this doping method.

The magnetoelectric properties of the boron doped films were investigated by inverse photoemission spectroscopy. A transversely polarized spin electron gun based upon the Ciccacci design was used to characterize the samples.[161] The spin electron gun was designed in a compact form on a separate chamber equipped with an iodine-based Geiger-Mueller isochromat photon detector with a SrF_2 window, with base pressure of 3.0×10^{-10} mbar or better. As is typical of such instruments, the electron gun has 28% spin polarization, and the data has been corrected for this incident gun polarization. The direction of electron polarization is in the plane of the sample. The energy resolution was in the vicinity of 400 meV. The magnetoelectric cooling was accomplished in applied axial magnetic and electric fields with magnitudes in excess of 40 mT, with a 1400 V respectively. The Fermi level was established from tantalum and gold foils in electrical contact with the sample. Typically, many experiments are summed, to improve the signal-to-noise ratio in the spin-polarized inverse photoemission spectra.

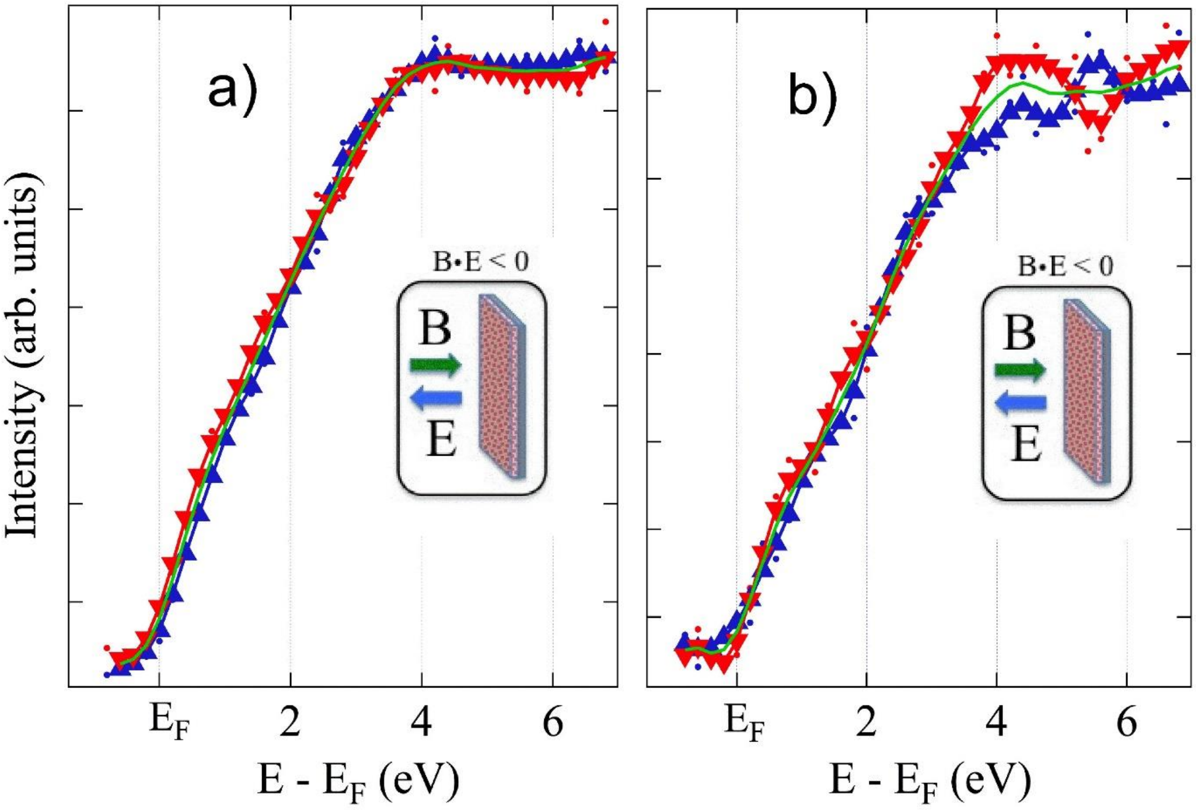

Figure 6.3: Spin-polarized inverse photoemission spectra taken at 295 K after field cooling with B•E < 0. Data are shown for Boron concentrations less than 1% (a) and approximately 3% (b), as determined from XPS core level intensities. Spin majority - spin up state, and spin minority - spin down state, components are indicated by upward triangles and downward triangles, respectively, as a smoothed spectra result. The green lines are spin integrated spectra.

The significance of the inverse photoemission experiments lies in the fact that their unmatched surface sensitivity allows us to determine whether the B-doped films possess boundary magnetization and whether this boundary magnetization can be switched via voltage-control, a necessary prerequisite for their use in potential room temperature spintronic applications. Figure 6.3 shows the spin polarized inverse photoemission of B-doped chromia thin films with doping concentration <1% (Figure 6.3a) and a B-doped chromia of about 3% (Figure 6.3b). Spin up and spin down channels are represented by up and down triangles. The lines represent the respective average inverse photoemission signal. The spectrum of low B-doped samples (Figure 6.3a) measured at T=295 K shows no appreciable spin polarization, similar to undoped chromia. However, Figure 6.3b depicts the spin resolved inverse photoemission spectra of the 3% boron doped sample with significant spin polarization at room temperature. Electric field switching was demonstrated together with control experiments in non-spin-mode over several samples.

A key result is that the boundary magnetization is seen to reverse when the electric field is reversed during field cooling to T=295 K. It confirms a magnetoelectric origin to this boundary magnetization together with the fact that sizable boundary magnetization is present at T=295 K. The spectra of the doped samples are in contrast to the spectra of the undoped samples where the antiferromagnetic order parameter and the boundary magnetization are too low at T=295 K to resolve voltage-controlled switching via inverse photoemission. The photoemission data are thus consistent with the data from SQUID magnetometry shown in Figure 6.2 and moreover confirm that B-doped samples with increased Néel temperature have voltage-controllable boundary magnetization.

In conclusion it has been shown that B-doping of the magnetoelectric antiferromagnet chromia is an efficient way to increase the Néel temperature. Findings obtained by SQUID magnetometry and spin polarized inverse photoemission spectroscopy are in good agreement with first principle investigations predicting an increase of the Néel temperature by approximately 10% per 1% substitution of oxygen by boron. Magnetometry data reveal an increase of the critical temperature of chromia from its bulk value of 307 K to 400 K by approximately 3% boron doping. The findings are of utmost significance for the use of chromia in ultra-low power, voltage-controlled spintronic applications at practical temperatures.

Chapter 7: Voltage-controlled Néel vector rotation in zero magnetic field

In this chapter, it is shown that by boron doping chromia, the new functionality of voltage-controlled, non-volatile Néel vector reorientation in the absence of an external magnetic field arises. Switching is demonstrated in prototype Hall bar structures which are sensitive to the antiferromagnetic boundary magnetization. Switching of the Hall voltage between zero and non-zero values imply a 90° Néel vector reorientation. Combined magnetometry, spin resolved inverse photoemission, electric transport and scanning probe microscopy measurements support this interpretation. A model which employs boron induced nanopolar regions which strain the B:Cr_2O_3 is presented to explain the anisotropy change from out-of-plane to in-plane. These results were published in Nature Communications.[162]

It has been shown that magnetoelectric antiferromagnets such as chromia may be useful in voltage-controlled spintronic devices. Voltage-controlled switching of the Néel vector between 180° antiferromagnetic domain states can be achieved by lifting the degeneracy between the two states. In chromia this is accomplished by simultaneously applying E and H along the c-axis, when the magnetoelectric energy, $2\alpha EH$, overcomes the anisotropy energy barrier between the two antiferromagnetic single domain states, the antiferromagnetic spin structure of the crystal will reverse.[40] The antiferromagnetic domain state is intimately coupled with the boundary magnetization which can in turn be exchange coupled to an adjacent ferromagnet. In such heterostructures, under certain conditions, reversing the antiferromagnetic domain state can also reverse the remnant magnetization of the ferromagnet.[37, 46-48, 163] Switching of this sort is often known as voltage-controlled switching, however magnetoelectric switching requires the simultaneous presence of E and H fields to create an energy difference between the two antiferromagnetic domains states to allow for switching. In principle, a static magnetic field could be provided, with no additional energy requirement, by a nearby ferromagnet via stray-field or exchange field,[145] but this extra requirement is detrimental to the implementation of practical devices. In the previous chapter it is demonstrated that boron doped chromia may be more suitable for device applications due to its higher Néel temperature, here it is demonstrated that B-doped chromia also does not require an external magnetic field in order to switch its antiferromagnetic spin structure, making it a promising single-phase material for energy efficient nonvolatile CMOS compatible memory applications.

Although antiferromagnetic order and the persistence of magnetoelectricity have been predicted and demonstrated up to T = 400 K in B-doped chromia,[148, 154] utilizing the high-T_N material in device structures which rely on exchange bias, remains elusive. In device architectures based on voltage-controlled exchange bias, B-doping does not translate into improved device performance. Although B-doping can increase the Néel temperature of the chromia, exchange coupling is not accompanied by effective pinning and thus voltage-control of the ferromagnet. Figure 7.1 demonstrates this short-coming.

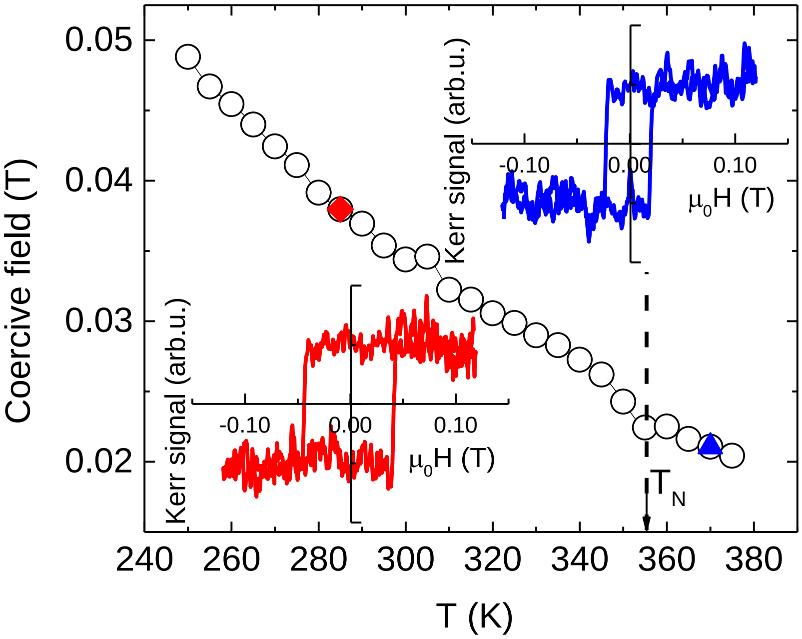

Figure 7.1: Coercive field versus temperature of hysteresis loops of CoPd film in proximity of 10% B-doped chromia (100nm). T_N=355 K is indicated by an arrow and a vertical dashed line. Insets show representative loop at 285 K < T_N (lower inset and red diamond data point in H_c vs T) and 370 K > T_N (upper inset and blue triangle data point in H_c vs T) measured by polar Kerr effect, respectively.

The temperature dependence of the coercive field (H_c) of a perpendicularly magnetized CoPd ferromagnetic film exchange coupled with a 10% B-doped chromia film is shown. The ferromagnetic hysteresis loops of CoPd have been measured at various temperatures using polar magneto-optical Kerr effect. Below the Néel temperature of T_N= 355 K, loop broadening sets in. It is associated with exchange coupling between the interface magnetizations of the antiferromagnetic and ferromagnetic films indicating that antiferromagnetic order has been established for $T \leq 355$ K.[131] However, despite the presence of exchange, shift of the perpendicular CoPd hysteresis loop along the magnetic field axis is absent. Presence of exchange coupling in the absence of a loop shift, is repeatedly observed for ferromagnetic films with perpendicular anisotropy on B-doped chromia. The detrimental effect of B-doping on perpendicular exchange bias in these heterostructures can be attributed to reduced magnetic anisotropy and canting of the interfacial magnetization relative to the surface normal as evidenced by replacing the perpendicularly magnetized CoPd ferromagnet with an in-plane magnetized ferromagnet.

When growing B:Cr_2O_3/CoPd heterolayers with in-plane anisotropic CoPd films, sizable exchange bias reappears below the Néel temperature substantiating the interpretation that B-doping is associated with anisotropy reduction and spin canting. Figure 7.2 shows the temperature dependence of the exchange bias field ($\mu_0 H_{EB}$) *versus* temperature, of the exchange bias field in a $Cr_2O_{2.9}B_{0.1}$(100nm)/Pd(0.5nm)Co(3nm)Pd(0.5nm) heterostructure where the ratio of Co to Pd film thickness tunes the anisotropy of CoPd heterolayers to be in the plane.[164]

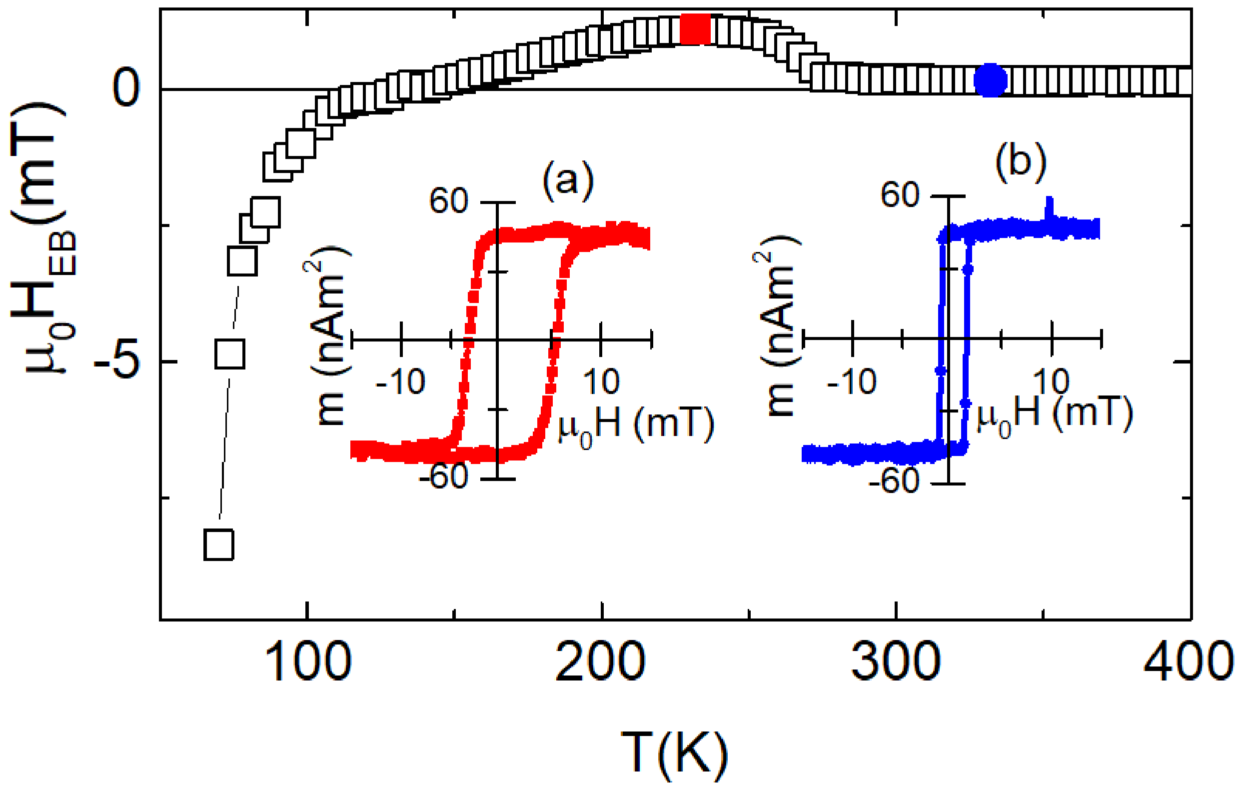

Figure 7.2: Exchange bias field ($\mu_0 H_{EB}$) versus T (open squares in main panel) for heterolayer based on B-doped chromia and in-plane anisotropic CoPd top layer. Insets a (red squares) and b (blue circles) show representative hysteresis loops at 323 K and 232 K. The loops are associated with $\mu_0 H_{EB}$ versus T data highlighted by solid squares.

Insets (a) and (b) in Figure 7.2 show representative in-plane CoPd hysteresis loops measured via vibrating sample magnetometry. The loops show positive exchange bias fields of 0.18 and 1.1 mT at 323 and 232 K, respectively. The absence of perpendicular exchange bias and the presence of in-plane exchange bias in B:Cr_2O_3-based heterostructures indicate that the boundary magnetization in B-doped chromia tends to tilt away from the c-axis which is consistent with recent findings in $CoFe_2O_4$ nanocomposites.[165] Further evidence for the interpretation of canted boundary magnetization comes in the form of temperature dependent spin resolved inverse photoemission. Inverse photoemission is a surface sensitive probe of the unoccupied spin dependent states. The presence of a spin resolved inverse photoemission signal, in the geometry of our experiment requires a tilt of the surface spins relative to the *c*-axis.

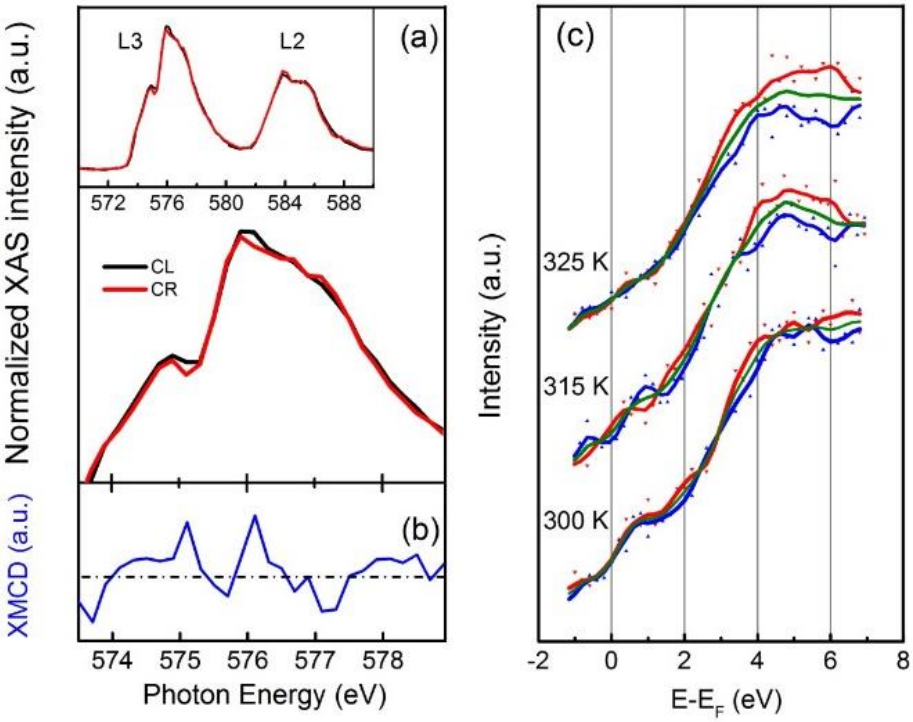

Figure 7.3: (a) XAS spectra at Cr L3 edges for B-doped Cr_2O_3 thin film. The inset shows the wider XAS energy range across both L2 and L3 edges. The spectra were taken at ~320 K. The polarity of light was label as CL (black) and CR (red) for circular left and right polarization respectively. (b) XMCD spectrum at Cr L3 edges. (c) Spin-polarized inverse photoemission spectra taken at different temperature as labeled after field cooling with $B \cdot E < 0$. Spin majority-spin up state and spin minority-spin down state are indicated by blue and red markers respectively. The green lines are spin integrated spectra.

The spin-polarized inverse photoemission spectra were taken at various temperatures. The magnetic and electric field were both applied to achieve field cooling from 500 K to 300 K with $B \cdot E < 0$. After field cooling, the spectra were taken at ~300 K and the sample was gradually heated to targeted temperatures of ~315 K and ~325 K where corresponding spectra were taken when the thermal equilibrium was achieved. In Figure 7.3 (c) blue up and red down triangles are signals associated with spin up and spin down electronic states. The difference in intensity for the spin polarization *versus* binding energy at 300, 315, and 325 K indicates that boundary magnetization and thus AFM order persist above the Néel temperature of pure chromia. It was found that the in-plane spin polarization increases with increasing temperature over the range 300 to 325 K. Since the spin asymmetry is increasing in a region where the boundary magnetization is decreasing, this generally indicates that the in-plane spin polarization increases faster than the boundary magnetization declines. Independent validation of the spin-polarized inverse photoemission data comes from X-ray absorption (XAS) and X-ray magnetic circular dichroism (XMCD) which were carried out at Canadian Light Source. The in-plane X-ray magnetic circular dichroism in Figure 7.3 (a), shows a small, but nonetheless non-zero signal at the Cr L3 ($2p_{3/2}$) edge, indicative of a small in-plane Cr^{3+} moment at 320 K.

While the reduction of magnetic anisotropy and the associated canting of the boundary magnetization in $B:Cr_2O_3$ hamper its use in devices which rely on an exchange biased ferromagnetic layer, these are not concerns in non-ferromagnetic Hall bar structures. Hall bars structures of non-ferromagnetic heavy metals on chromia have been experimentally established as a reliable readout mechanism for the boundary magnetization.[44, 108, 114] In our Hall-device, a Pt Hall bar detects a transverse voltage signal, V_{xy}, in response to an in-plane current density. The Hall-like signal V_{xy} is widely believed to originate from spin Hall magnetoresistance.[45, 166]

Spin Hall magnetoresistance is actually a combination of the spin Hall effect and the inverse spin Hall effect. The spin Hall effect uses a charge current to create a spin current, while the inverse spin Hall effect uses a spin current to create a charge current. The spin Hall effect is characterized by the equation[167]

$$\boldsymbol{J_S} = \alpha_{SH}\left(-\frac{\hbar}{2e}\right)\boldsymbol{J}_q \times \boldsymbol{s} \tag{8.1}$$

Where $\boldsymbol{J_S}$ is the spin current, $\boldsymbol{J}_q$ is the charge current, $\boldsymbol{s}$ is the spin polarization, and α_{SH} is the spin Hall angle. For a Hall bar device it makes sense to restrict the discussion to the charge currents which are in-plane, therefore we consider a charge current flowing in the **x**-direction. Here we are primarily interested in the spin current generated in the **z** direction (normal to the plane). By equation 8.1 the spins contributing to this spin current have $\boldsymbol{s} \parallel \boldsymbol{y}$. As these spins impinge upon the chromia/Pt interface, the resulting scattering is dependent on the relative orientation of the magnetic moment at the boundary and the spin current. Then by the inverse spin Hall effect the interaction the magnetization at the boundary has on the spin current will be reflected in the charge current and ultimately the measured Hall voltage.[45, 115, 167]

The Hall cross was fabricated by depositing Pt via DC magnetron sputtering, and subsequent lithographic patterning to create a 5 nm thick Pt Hall-cross with 2 orthogonal legs of 7.0 μm × 1.0 μm. on top of a 200 nm B-doped chromia film. The B-doped chromia has been grown via pulsed laser deposition on top of 20 nm V_2O_3 also grown by pulsed laser deposition which serves as a bottom electrode. The device is pictured in Figure 7.4, for simplicity, canting present in B-doped chromia is not shown.

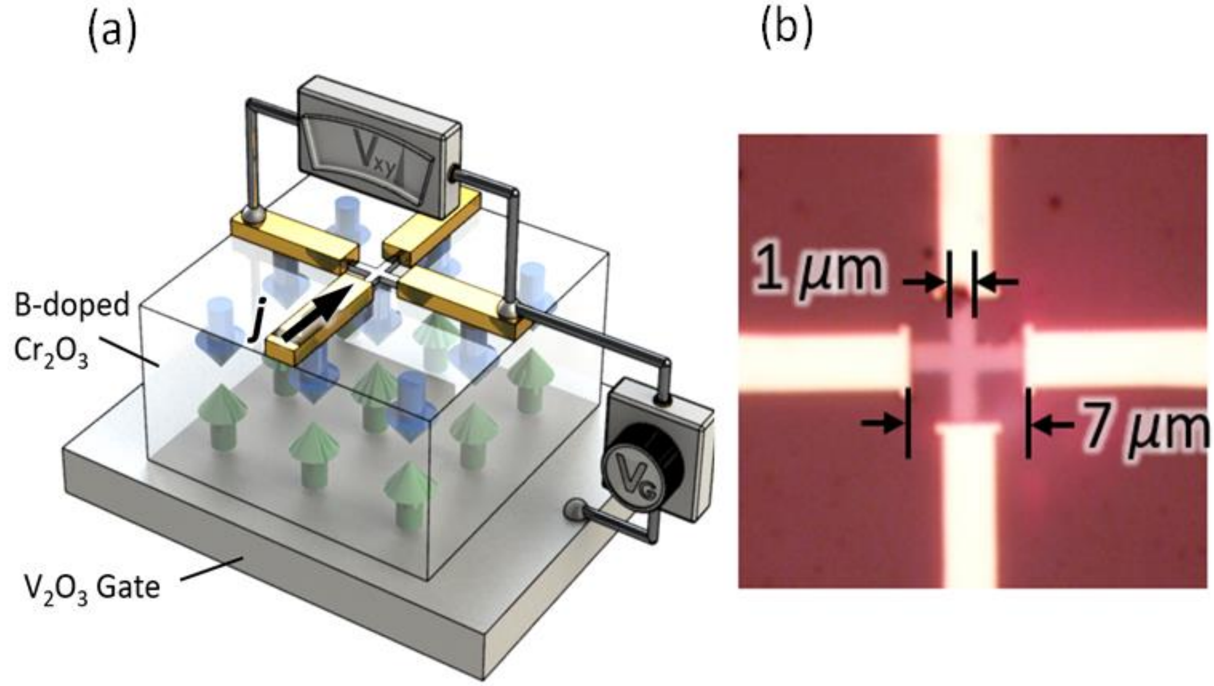

Figure 7.4: (a) Illustration of the Hall bar device showing V_2O_3 back gate, B-doped Cr_2O_3 film with antiferromagnetic spin structure, Pt Hall cross with Au electrodes, current density j flowing in direction of black arrow causing signal V_{xy} which depends on applied voltage V_G. (b) Optical image of the device with 7.0μm × 1.0μm legs forming the Pt Hall cross with attached Au electrodes on top of the B-doped Cr_2O_3 film.

Both temperature assisted and isothermal magnetoelectric non-volatile switching of pure chromia thin films has been demonstrated by a similar device.[44] As is always the case with magnetoelectric switching simultaneous application of an electric and magnetic field was required. Remarkably, when the pure chromia is replaced by B:Cr_2O_3, the magnetic field is no longer necessary. Figure 7.5 shows a hysteresis loop V_{xy} *versus* V_G measured at 300 K in zero magnetic field. The voltage V_G is applied as a quasistatic pulse between the top and bottom electrode of the device as shown in Figure 7.4 (a). The voltage is removed before probing V_{xy} using a longitudinal current of 20 μA. The sharp transitions at the coercive voltages of about ± 15 V resemble deterministic switching between distinct antiferromagnetic states. These results were repeated on various devices at temperatures up to 400 K.

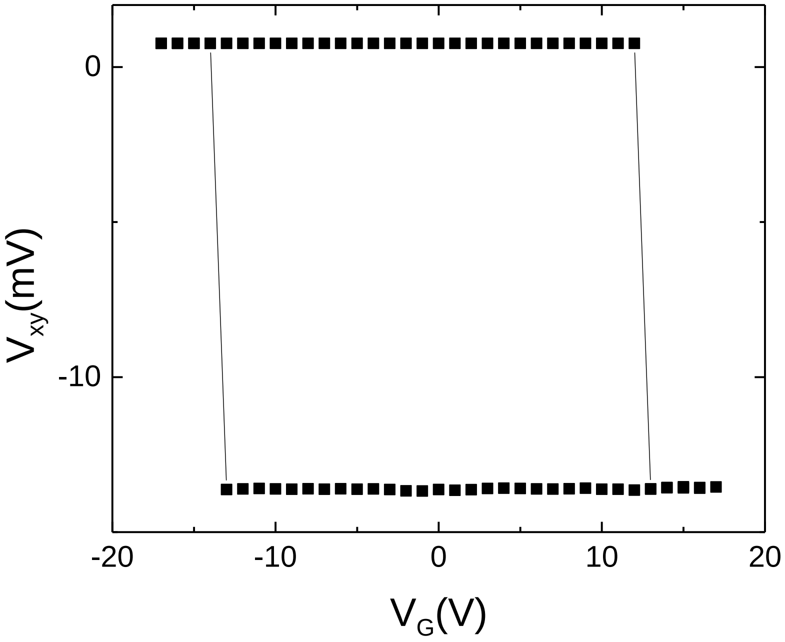

Figure 7.5: *V_{xy} versus V_G* hysteresis loop of a Hall bar device on B:Cr_2O_3 measured at 300 K in zero magnetic field.

Switching between antiferromagnetic domain states in zero magnetic field indicates that ME switching, which is the well-established switching mechanism in pure chromia, can be ruled out. The high degree of asymmetry in V_{xy} on switching between different nonvolatile antiferromagnetic states associated with $V_{xy} \approx 0$ and $V_{xy} \approx 15$ mV implies 90° rotation of the Néel vector, in sharp contrast to Hall-signals observed for 180-degree switching.[44] Rotation of the Néel vector by 90° is consistent with the fact that time reversal symmetry is not broken by an electric field.

Reversible, non-volatile switching is demonstrated by applying an electric field across the device by creating a voltage pulse of $V_G = \pm 25$ V for ~4 s between the hall bar and the bottom electrode. The voltage is removed and the Hall signal V_{xy} is subsequently measured using a current of 20 μA. One hundred subsequent Hall measurements in zero field were performed to determine a baseline for V_{xy} associated with a particular AFM state. After every hundredth point, a voltage pulse of $V_G = \pm 25$ V (of opposite sign) was again applied across the B:Cr_2O_3 film. Figure 7.6 (a) and (b) show V_{xy} of the Hall measurements taken at T=300 K, the grid of dashed vertical lines marks the points where unipolar voltage pulses are applied. The data in Figure 7.6 (a) demonstrate that a voltage pulse, V_G, can switch V_{xy} and thus the antiferromagnetic spin structure of the B-doped chromia film in zero applied magnetic field. A control experiment shown in Figure 7.6 (b) shows data taken at $-1\ T$ implying that the signal switching is independent of the presence of an applied magnetic field.

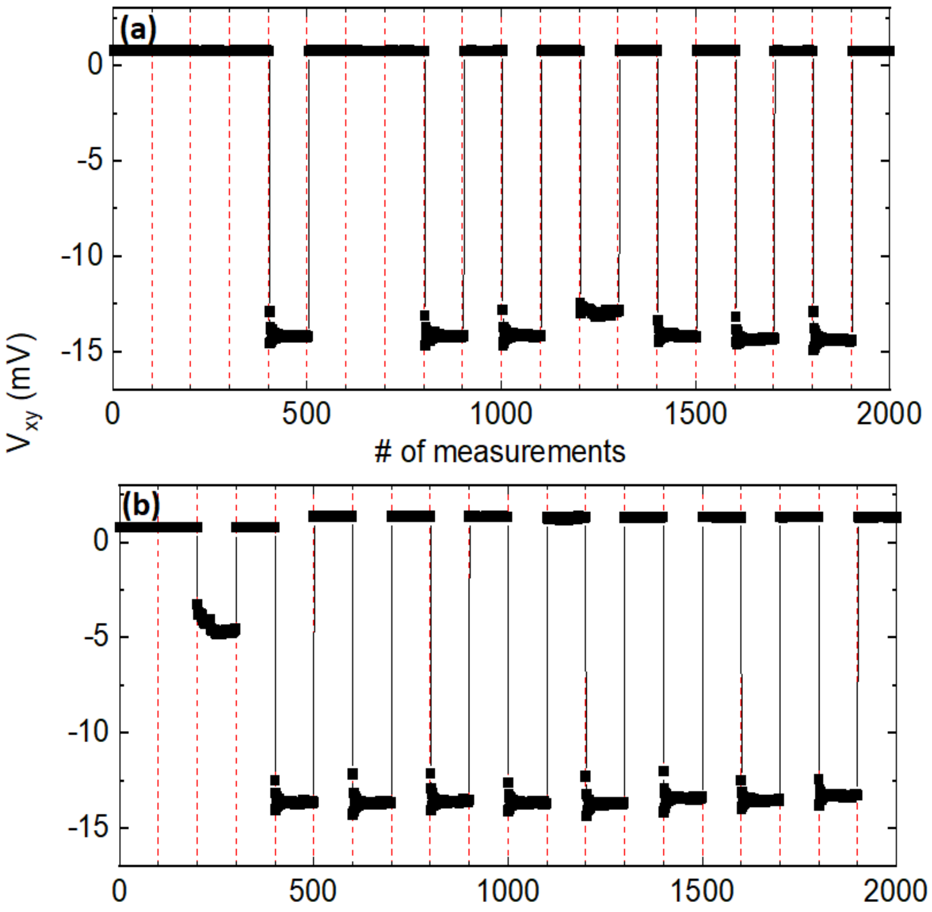

Figure 7.6: (a) and (b) show V_{xy} versus the number (#) of measurements. Vertical dashed lines indicate respective application of a voltage pulse $V_G = \pm 25$ V. Measurements are done at T=300 K in (a) 0 T, and (b) −1 T applied magnetic field

To unambiguously show that the different states of $V_{xy}^{zero} \approx 0$ and non-zero $V_{xy}^{non-zero} \approx -15$ mV are indicative of magnetically distinct states of B:Cr_2O_3 we measured the magnetic field dependence of V_{xy}^{zero} and $V_{xy}^{non-zero}$. Figure 7.7 shows the magnetic response of V_{xy}^{zero} (red circles) and $V_{xy}^{non-zero}$ (black squares) at T=300 K measured in a B:Cr_2O_3/Pt Hall bar device. The two different states are initialized by voltage pulses of +24 V (selecting V_{xy}^{zero}) and -25 V (selecting $V_{xy}^{non-zero}$). $V_{xy}^{zero}\ vs. H$

clearly shows a positive slope while $V_{xy}^{non-zero}\ vs. H$ is qualitatively distinct through the virtual absence of magnetic field dependence.

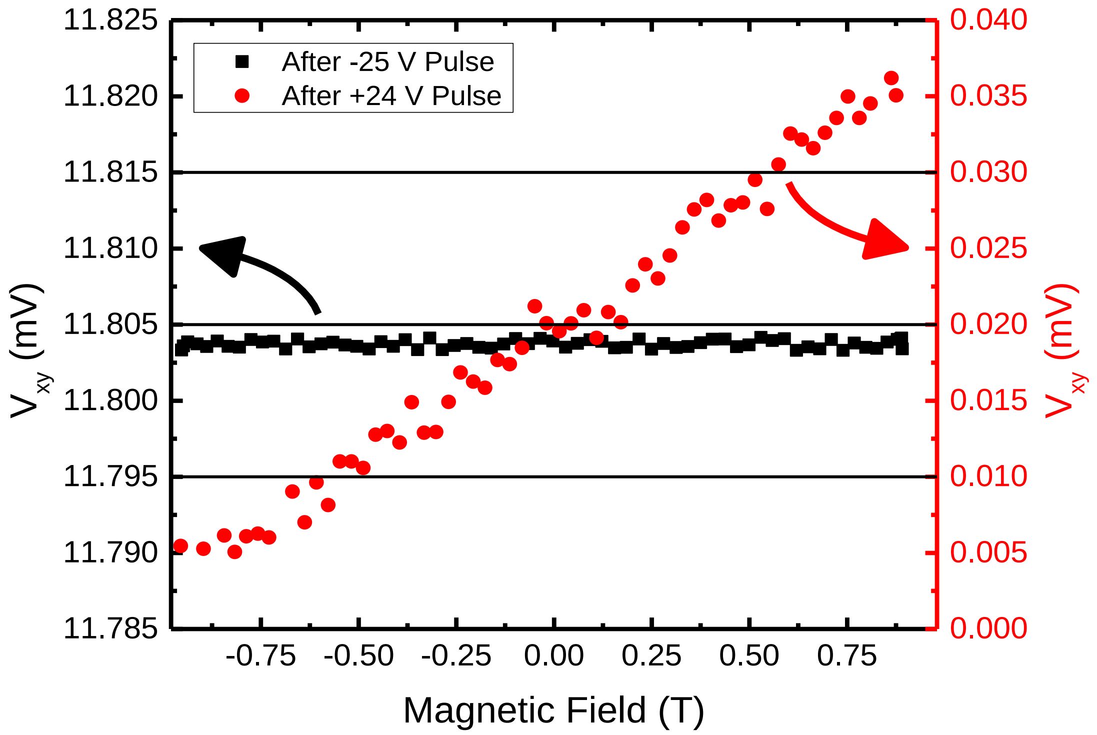

Figure 7.7: Magnetic field dependence of the transverse Hall voltage of the two states V_{xy}^{zero} and $V_{xy}^{non-zero}$ measured in a B:Cr_2O_3/Pt Hall bar device. The two distinct states are prepared by voltage pulses of +24 V (red circles) and -25 V (black squares).

This finding strongly supports the magnetically distinct behavior of the two states. The magnetic field dependence of the transverse Hall signal is consistent with spin Hall magnetoresistance. The V_{xy}^{zero} state is associated with in-plane orientation of the Néel vector and thus in-plane orientation of the boundary magnetization. As a result, the applied magnetic field normal to the surface creates maximum torque on the boundary magnetization tilting it out of the plane with increasing applied magnetic field. The increase of the normal component of the boundary magnetization increases the spin Hall magnetoresistance. The $V_{xy}^{non-zero}$ state is characterized by a large spin Hall magnetoresistance already at H=0 consistent with an out-of-plane orientation of the boundary magnetization. In this state, the applied magnetic field and the boundary magnetization are collinear, giving rise to minimal torque on the boundary magnetization, resulting in virtually negligible magnetic field response.

To provide independent evidence that the switching effects shown in Figure 7.5 and Figure 7.6 are magnetic in origin, we carried out additional measurements by magnetic force microscopy (MFM). Magnetic force microscopy utilizes the long-range forces, originating from interaction between a magnetized tip and the magnetic stray field of the sample. Figure 7.8 shows the topographic and magnetic force images of a segment of the Pt Hall cross, which was deposited on the same B:Cr_2O_3 thin film used for the devices in Figure 7.5 and Figure 7.6. The magnetic force microscopy images illustrate a change in the magnetic response signal of the pristine sample after application of the poling pulses of 2 s duration and +/-10 V magnitude. Clearly visible is the drastic reduction of the magnetic force contrast after application of the +10 V pulse and its partial recovery after application of the -10 V pulse.

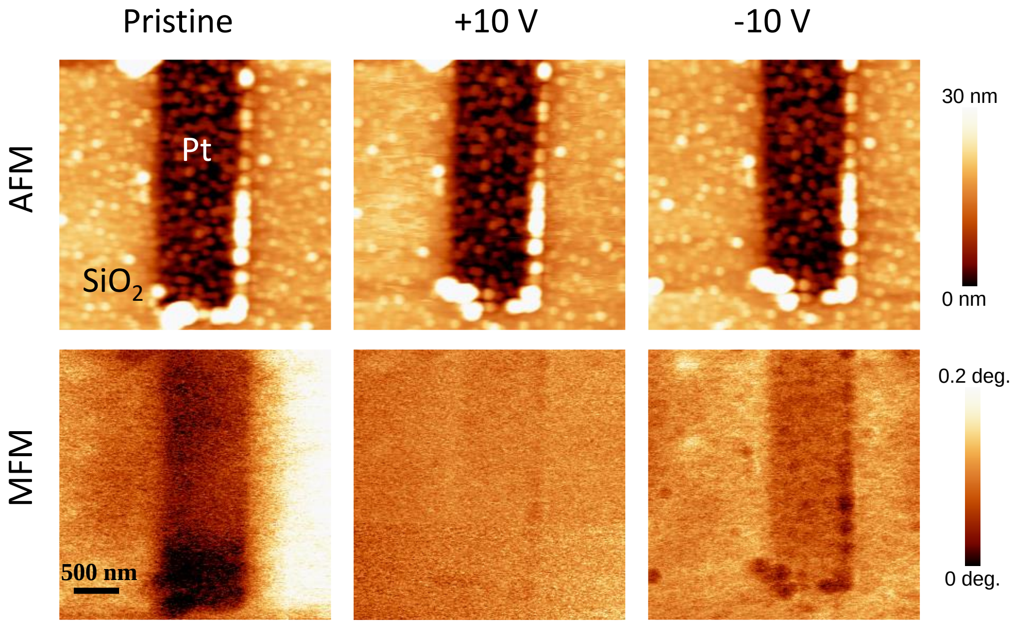

Figure 7.8: Top row: topographic images of a segment of the Pt Hall cross before and after application of the poling pulses (2 s; +/-10 V). Bottom row: Magnetic force microscopy images of the same segment after application of the poling pulses.

Since magnetoelectric switching is ruled out by the independence of the switching on applied magnetic field, indirect coupling between induced polarization and antiferromagnetic order is investigated. Using piezoresponse force microscopy (PFM), evidence was found of an induced dielectric polarization in B:Cr_2O_3. Figure 7.8 (a) shows the piezoresponse force microscopy measurements done (with the bias off) on the Pt/B:Cr_2O_3/V_2O_3 heterostructure which reveals the typical butterfly-shape amplitude hysteresis loops along with the 180° change in the phase indicating the presence of a switchable polarization in B:Cr_2O_3. No such response is detected in undoped chromia.

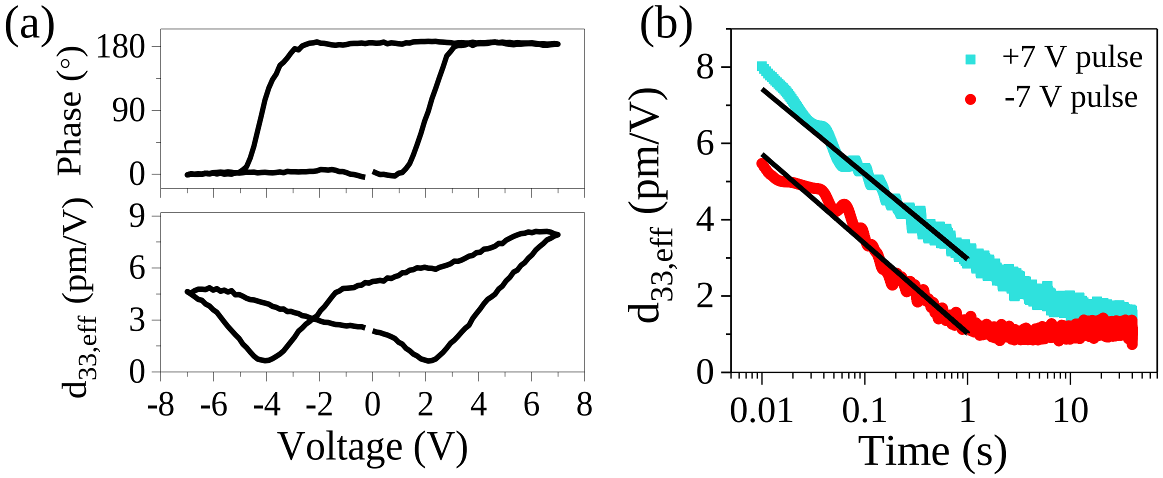

Figure 7.8: (a) Bias-off PFM amplitude (bottom panel) and phase (top panel) hysteresis loops measured in the Pt/B:Cr2O3(200nm)/V2O3 structure. (b) PFM amplitude signal as a function of time elapsed after application of a positive (blue) and negative (red) poling pulses (7 V, 12.5 ms). Solid lines in (b) illustrate the logarithmic fit of the temporal decay of the effective piezoelectric coefficient $d_{33}(t)$ in accordance with a relaxation model for electric field oriented PNRs

Previously, it has been shown that robust piezoforce microscopy signals could be registered in the non-ferroelectric materials due to electrically induced polarization resulting from various mechanisms, such as redistribution of oxygen vacancies[168] or reorientation of polar nanoregions (PNRs).[169] Figure 7.8 (b) shows that the PFM amplitude signal, measured in the Pt/B:Cr_2O_3/V_2O_3 heterostructure. The effective $d_{33,\mathrm{eff}}$ piezoelectric coefficient of B:Cr_2O_3 can be estimated by comparing its electromechanical response with the signal detected in another material with the well-known piezoelectric properties.[170, 171] $LiNbO_3$ is chosen as a reference material and by comparative analysis the amplitude signal measured in B:Cr_2O_3 yields a value of $d_{33} \approx 8$ pm/V right after the application of 7 V. However, this signal is not stable, but relaxes logarithmically with a characteristic relaxation time varying in the range from several hundreds of milliseconds to tens of seconds. This behavior suggests that voltage pulse application produces a metastable polarization state in B:Cr_2O_3. Logarithmic relaxation of the induced piezo-response after poling is characteristic of thermally activated polar nanoregions.[172]

Figure 7.9 illustrates a possible mechanism which gives rise to polar nanoregions in B:Cr_2O_3. The polar nano regions are linked to inhomogeneous local strains produced by random substitution of O atoms for B. The local strain moves the B atom to an off-center position within BCr_4 tetrahedra resulting in emergence of PNRs.[157, 173]

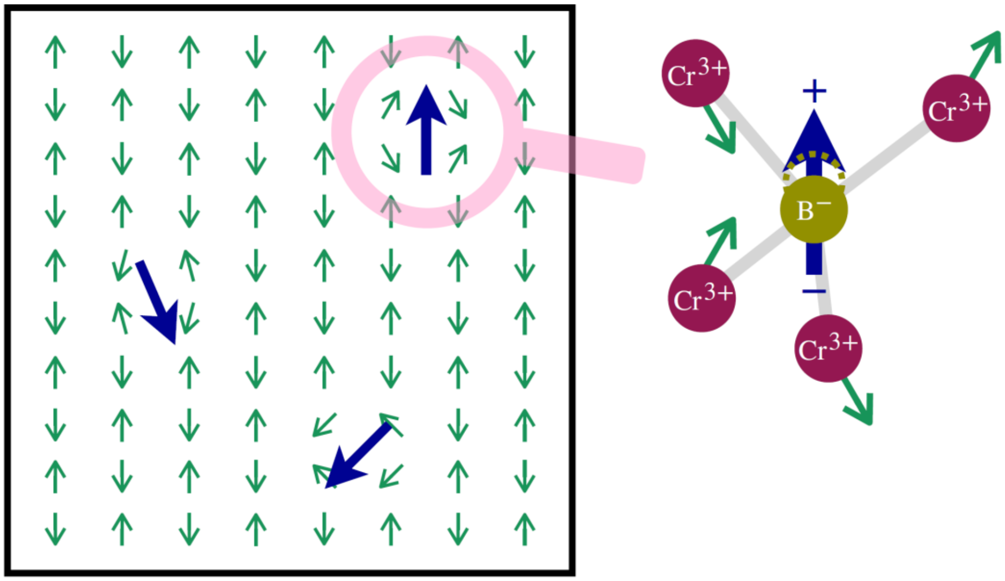

Figure 7.9: Illustration of polar nanoregions (blue arrow) arising from off-center B- substitutions and accompanying inhomogeneous local strains which give rise to canting of neighboring spins.

Electric field induced alignment of dipole moments in PNRs leads to detectable piezoresponse. Thermal fluctuations of polarization after the field is off cause temporal decay of the piezoelectric coefficient, which follows the logarithmic law: $d_{zz}(t) \approx d_0 - S\, log_{10}\left(\frac{t}{t_0}\right)$ where S is a measure of viscosity and $1/t_0$ is the attempt frequency. This equation is fitted in Figure 7.8 (b). The observed difference in the peak amplitude of the piezo-response between positive and negative poling voltage may be caused by residual strain near the surface.[172]

E-field induced orientation of polar nano regions plays a critical role in the interplay between polarization, piezoelectricity, strain and anisotropy control, which gives rise to the Néel vector rotation. The applied E-field aligns the polar nanoregions which transforms the local strain distribution into a uniform strain field $\epsilon = d_{33}E$. First-principles calculations show that the magnetic anisotropy (K) in undoped chromia is close to cubic and the preference to perpendicular anisotropy is strongly modified by strain as $\Delta K_\perp / K_\perp \approx 10^3 \epsilon$.[155] Assuming similar results in B:Cr_2O_3, depending on the direction of electric E-field (parallel or antiparallel to the *c*-axis), the piezoelectrically induced strain is compressive or tensile enabling rotation of the Néel vector between in-plane and perpendicular orientations. The nearly cubic anisotropy creates local minima in the free energy landscape giving rise to nonvolatility after removal of the E-field. The switching criterion $\Delta K_\perp / K_\perp = 1$, along with the experimentally observed coercive electric field of $E_c \approx 15$ V/200 nm, leads to an estimated piezo-response coefficient of $d_{33} = 13$ pm/V. The measured d_{33} (Figure 7.8) roughly agrees with this estimate and supports the model.

In conclusion, this chapter demonstrates that the prototypical magnetoelectric antiferromagnet Cr_2O_3 can be tuned into a multi-functional high-T_N material through B-doping. Emerging functionality associated with B-doping include purely electric-controlled 90-degree nonvolatile rotation of the Néel vector up to $T = 400$ K. Indirect coupling between polar and antiferromagnetic order explains the experimental findings. A prototype energy efficient memory which operates up to 400 K in zero magnetic field has been fabricated on the basis of B-doped chromia.

Chapter 8: Future research directions and summary

In this chapter an unexplained magnetoelectric effect in chromia is outlined. The effect concerns the magnetoelectric response of chromia when subject to exactly the critical magnetic field which causes the spin-flop transition. It is seen the effective magnetoelectric susceptibility can be enhanced by up to 10x, but the effect significantly differs between temperatures. A summary of key results is then presented.

8.1 Future research directions

The magnetoelectric effect was first predicted by Landau and Lifshitz in 1960,[27] the effect was predicted to exist in chromia by Dzyaloshinskii shortly thereafter,[30] and Astrov was the first to observe it experimentally.[31] Since then, chromia, as the prototypical magnetoelectric material has been studied for decades, yet it is still possible that the magnetoelectric effect is not completely understood in this material.

Besides being magnetoelectric, chromia also has the interesting property of having a spin-flop transition at high magnetic field. A spin flop transition occurs in antiferromagnets when a large magnetic field is applied parallel to the antiferromagnetic vector. At a certain magnetic field value, it becomes energetically favorable for all of the spins in the lattice to compromise their antiparallel alignment and begin to align parallel to the applied magnetic field.[174] This tipping point is called the spin-flop transition. The magnetoelectric effect has been studied at low magnetic fields and also at high magnetic fields above the spin-flop transition, however, there have been very few studies on how the magnetoelectric susceptibility behaves at the critical field at which the spin-flop occurs. At this particular magnetic field, the crystal will be in a state which is partially in the spin-flop phase and partially in the normal phase. At this point, it has been reported that the apparent magnetoelectric susceptibility is enhanced by ~10x.[175]

The sample under study here is a bulk chromia single crystal sample, commercially obtained with the (0001) axis perpendicular to the plane of the sample. All magnetic measurements were taken in a superconducting quantum interference device (SQUID) with the chromia crystal aligned with the (0001) axis parallel to the applied magnetic field. The electric field was accomplished by using silver paste electrodes across the thickness of the sample (0.4 mm) so that the electric field is also applied along the (0001) axis. Before all measurements the sample was prepared in a single domain state by means of magnetoelectric annealing. The crystal was brought to 330 K (T_N=307 K) and electric and magnetic fields were simultaneously applied while the crystal was cooled to the temperature under study (20 K or 87.3 K). The applied fields lift the degeneracy between two 180° rotated antiferromagnetic domain states, each with opposite spin orientations and magnetoelectric susceptibilities. The fields used are +1 T and ±300 V. These field products are sufficient to ensure a magnetic single domain state.[37, 46, 117]

The magnetic response of the crystal from applied magnetic field is shown in Figure 8.1.1. In the region of 5.5 T and 6.5 T, the magnetic moment along the (0001) axis increases dramatically, this is caused by the spin-flop of the chromia spins. The critical field at which the spin flop happens (H_{SF}) is conventionally given by

$$H_{SF} = \sqrt{\frac{4K}{\mu_0(\chi_\perp - \chi_\parallel)}} \tag{8.1.1}$$

Where K, $\mu_0, \chi_{\perp}$, and $\chi_{||}$ are the anisotropy, the permittivity of vacuum, the perpendicular and parallel magnetic susceptibilities of chromia respectively. Note here, that an electric field dependence on either K, or $\chi_{\perp}/\chi_{||}$ would result in an electric field dependence on H_{SF}. While a purely electric field effect on K has been theoretically predicted,[155] the effect is expected to be miniscule for the voltages applied here. An electric effect on the magnetic susceptibility of chromia has, as far as we know, never been reported. Moreover, it is reasonable to expect a change in the susceptibilities would result in a change in the Néel temperature of the crystal.[176] For the magnitude of electric fields applied here, this is not observed. For these reasons we take both K, and $\chi_{\perp}$, $\chi_{||}$, to be static at any given temperature with respect to an applied electric field.

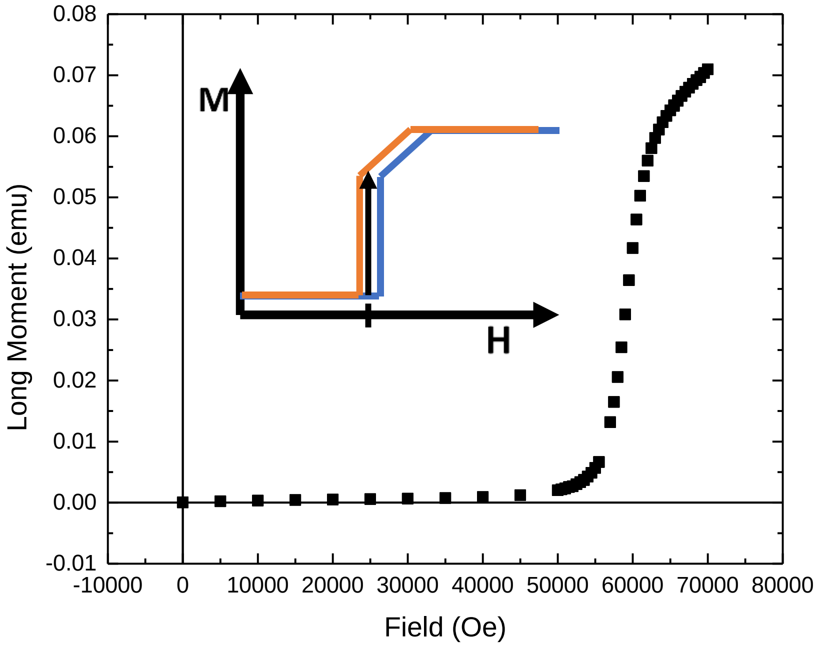

Figure 8.1.1: The magnetic moment measured in a chromia single crystal as the magnetic field is ramped through the critical value to induce a spin-flop. Inset: An idealized spin-flop which demonstrates that a large change in magnetization may result near the critical field if the spin-flop field was shifted from the blue curve to the orange curve.

These potential dependencies of the spin-flop field on the applied electric field are noted because as illustrated in Figure 8.1.1 (inset), even a small change in the spin-flop field caused by an applied electric field can result in a large change in magnetization, thus at the spin-flop transition the effective magnetoelectric effect would become large. The effective magnetoelectric susceptibility at the spin-flop transition would be:

$$\alpha_{eff}^{SF} = \mu_0 \left(\frac{\partial M}{\partial E}\right) = \alpha_{\parallel} + \mu_0 \frac{\partial M}{\partial H_{SF}} \frac{\partial H_{SF}}{\partial E} \tag{8.1.2}$$

The steepness of the spin-flop curve at the transition would effectively magnify the effective magnetoelectric effect.

The effective magnetoelectric effect sensitively depends on the value of the applied magnetic field. For that reason, the protocol to measure the effective magnetoelectric susceptibility at each magnetic field value at the target temperature is to set the magnetic field with the superconducting coils, then disengage the power supply to ensure the magnetic field is static for the duration of the measurement. At each magnetic field, a series of electric fields are applied, and the resulting magnetic moment is recorded. For each set of measurements at a given magnetic field, the linear slope of the data was obtained to calculate $(\partial M/\partial E)$. The results at 20 K for two different magnetoelectric annealing protocol are shown in Figure 8.1.2. The blue data are measured after annealing in (-300 V, +1 T), while the black data are measured after annealing in (+300 V, +1 T). In both sets of data, the effective magnetoelectric effect gets much larger in the region of the spin flop transition (~10x). The fact that the effect is reversed after opposite field products were applied during the annealing phase suggests that the origin of the effect is magnetoelectric rather than an electric field dependence of exchange or anisotropy.

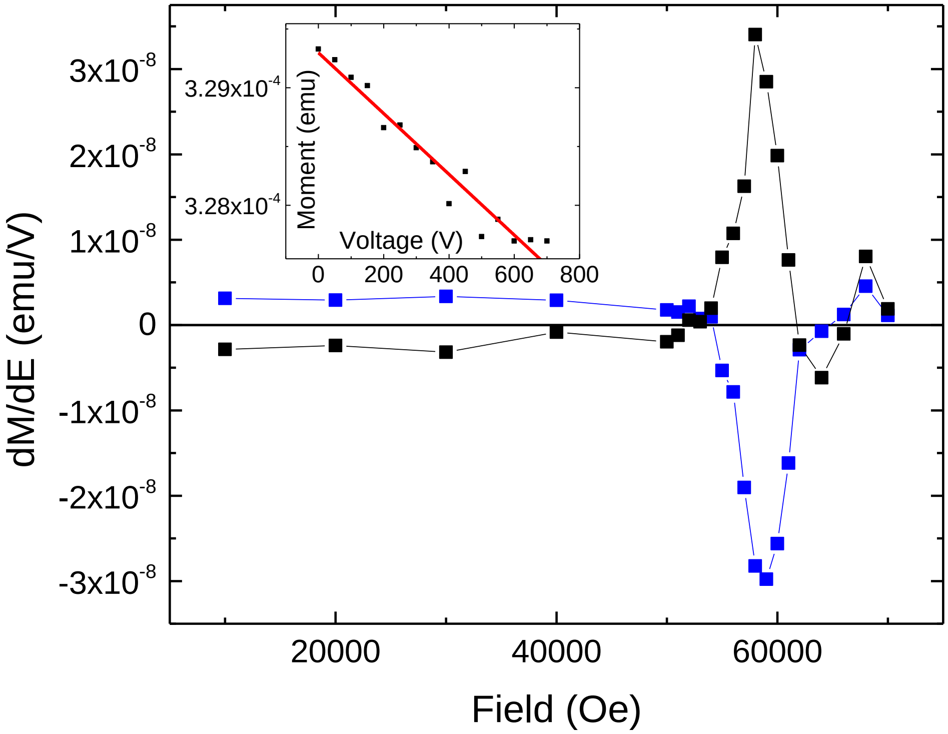

Figure 8.1.2: The effective magnetoelectric susceptibility across the spin-flop transition at 20 K. At each magnetic field the induced moment resulting from an applied electric field was fit with a line to calculate $\partial M/\partial E$ (Inset: Data at 10000 Oe). Results shown after field cooling in +1 T and +300 V (black) and -300 V (blue)

However, a simple explanation, wherein the spin-flop field is changed due to the magnetoelectric effect, does not necessarily hold up to scrutiny. The temperature dependence of magnetoelectric effect of chromia is well known, and the parallel magnetoelectric susceptibility in chromia (0001) crosses over to negative values at low temperatures.[31, 32, 177] Then there is a temperature at which the magnetoelectric susceptibility of chromia is zero, for this particular sample that crossover occurs at 87.3 K. At this temperature the parallel magnetoelectric susceptibility is zero, therefore if the enhancement of the effective magnetoelectric effect at the spin-flop transition is a consequence of a non-zero parallel magnetoelectric susceptibility, it would be expected that the peak structure disappears at that temperature. On the contrary there is a peak structure at 87.3 K as shown in Figure 8.1.3, at this temperature a double peak structure arises.

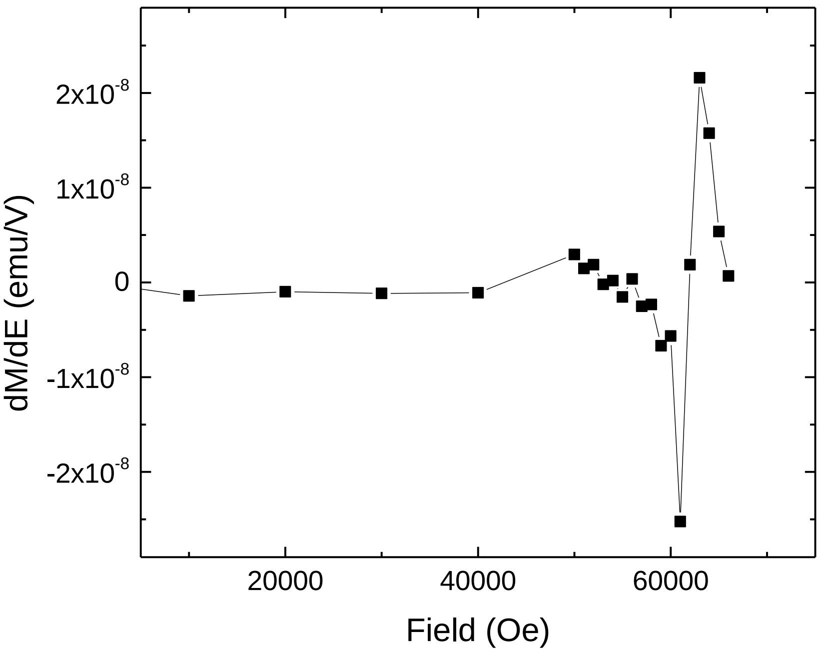

Figure 8.1.3: The effective magnetoelectric susceptibility across the spin-flop transition at 87.3 K. The electrical response at each magnetic field value is measured and the linear slope is plotted.

The most likely explanation of the peak structures comes from Holmes and Van Uitert who studied the magnetoelectric effect in $MnGeO_3$ across the spin-flop transition.[178] A similar single peak structure was measured and explained by a slight misalignment of the magnetic field with respect to the crystal axis. As in chromia, the magnetoelectric susceptibility tensor of $MnGeO_3$ changes its structure as it goes through the spin-flop transition. By weighting each tensor element according to the angle of the sublattice magnetization and considering all tensor elements in light of a small misalignment, a peak structure which was well matched to the data was calculated.

Although it is likely that this explanation can account for the single peak structure which arises at 20 K, it is unclear whether it can simultaneously describe the behavior at 87.3 K. The off-diagonal elements of the magnetoelectric susceptibility of chromia in the spin-flop phase may indeed play a role, but it is not clear from the theory presented that a double peak as observed can be generated in the complete absence of a parallel magnetoelectric susceptibility. The presence of the double peak structure at 87.3 K might be interpreted to mean the underlying mechanism is independent of the parallel magnetoelectric susceptibility. This interpretation also is questionable. All of the off-diagonal elements of the magnetoelectric susceptibility tensor are largely unchanged between the temperatures of 20 K and 100 K,[177] and the double peak structure only occurs in the vicinity where the parallel magnetoelectric susceptibility is zero.[175] The effect is also seemingly large enough that it is unlikely to be lost due to a superposition of effects at 20 K.

It seems clear that the rise of the double peak is intimately tied to the disappearance of the parallel magnetoelectric susceptibility in chromia. It is possible that a small adjustment to the theory of Holmes et. al. may be able to explain this behavior. It is also possible that it cannot. If not, resolving this issue might shed light on the underlying mechanism which causes the parallel magnetoelectric susceptibility to change sign at low temperature, an issue which has not yet been fully resolved.[179-181]

8.2 Summary

Voltage control of magnetization remains a key challenge in the field of spintronics, especially at CMOS compatible temperatures. It has been shown that chromia-based heterostructures such as the ME-MTJ may play a part in filling that role. The electric control of exchange bias in prototype devices has been demonstrated in 2010,[37] but at that time significant challenges remained. In this thesis, some of those challenges were addressed.

Using the same prototype device which was used to pioneer room temperature voltage-controlled magnetization switching, new dynamics and functionalities were discovered. It was found that, in certain circumstance, intermediate states existed between the two switching extrema, while in other cases they did not. Interfacial exchange coupling stabilizes the antiferromagnetic interface against the reversal of the bulk creating these intermediate states. In these states the near surface spin structure of the chromia is incommensurate with the underlying spin structure. Upon cycling the ferromagnet, the interfacial spins are allowed to relax which leads to exchange bias training. The dynamics of this training effect were analyzed using a discretized Landau-Khalatnikov model. The model is well matched with the observed effect, reinforcing this interpretation.

For those devices which would use exchange bias as a mechanism for voltage-controlled magnetization, such as envisioned in the ME-MTJ, maintaining exchange bias to as high a temperature as possible would be critical. Therefore, understanding the unique temperature dependence where an abrupt disappearance of exchange bias with a simultaneous more than two-fold increase in coercivity observed in chromia heterostructures is crucial. This behavior can be understood by applying a coherent rotation model to the antiferromagnetic-ferromagnetic interface. In doing so, the Meiklejohn criterion arises, and by considering the behavior of the system separately when this criterion is satisfied or not satisfied the behavior of the heterostructure is explained both before and after the transition. The transition therefore represents a threshold where the exchange field of the ferromagnet overwhelms the anisotropy of the antiferromagnet and the antiferromagnet interface begins to rotate with the ferromagnet. This interpretation is confirmed by measuring the increase in the total net magnetic moment participating in the hysteresis loop. This anisotropy is sensitive to applied electric field, and it is shown that by applying a voltage across the sample you can either stabilize or destabilize a certain interface spin configuration, causing a drastic change in the hysteresis loop isothermally. Importantly this method of voltage manipulation requires no external magnetic field.

Finally, to integrate chromia-based devices into current CMOS technology, it would be useful to increase Néel temperature to values well above room temperature. It was predicted that boron doping the chromia would increase its Néel temperature by approximately 10% per 1% boron substitution on the oxygen site.[155] By adding a doping cell to the PLD system, boron doping of chromia was accomplished using gaseous decaborane. The Néel temperature of the films were measured to be as high as 400 K while maintaining its magnetoelectric properties. Unfortunately creating exchange bias heterostructures with boron doped chromia remained elusive. It has, however, been previously shown that Hall bar magnetometry was sensitive to the boundary magnetization intrinsic to chromia. Hall bar measurements indicated that the antiferromagnetic Néel vector of the chromia could be reorientated from out of plane to in-plane by an applied electric field. This switching of the Néel vector takes place in zero magnetic field ruling out a magnetoelectric origin. This result was corroborated by magnetic force microscopy and spin-polarized inverse photoemission. Using piezoresponse force microscopy (PFM), evidence was found of an induced switchable dielectric polarization. It is theorized that the boron dopants create polar nanoregions in the film which indirectly couple the induced polarization and antiferromagnetic order through strain.

With these advancements the voltage control of magnetization in both chromia and boron doped chromia thin films is both better understood and much more functional. These results may pave the way for chromia base magnetic heterostructures to be used in functional low-power spintronic devices. At a time where the fundamental limitations of CMOS-based devices become more restrictive to progress of the microelectronics industry, chromia-based magnetic heterostructures may represent a path forward.

References

1. T. N. Theis and P. M. Solomon, Science **327** (5973), 1600-1601 (2010).
2. C. Binek and B. Doudin, Journal of Physics: Condensed Matter **17** (2), L39 (2005).
3. C. B. Peter A. Dowben, and Dmitri E. Nikonov, in *Nanoscale Silicon Devices*, edited by S. O. David K. Ferry (CRC Press, Boca Raton, 2016).
4. R. Islam, H. Li, P.-Y. Chen, W. Wan, H.-Y. Chen, B. Gao, H. Wu, S. Yu, K. Saraswat and H. S. Philip Wong, Journal of Physics D: Applied Physics **52** (11), 113001 (2019).
5. V. K. Joshi, Engineering Science and Technology, an International Journal **19** (3), 1503-1513 (2016).
6. P. Seneor, A. Bernand-Mantel and F. Petroff, Journal of Physics: Condensed Matter **19** (16), 165222 (2007).
7. K. J. Dempsey, D. Ciudad and C. H. Marrows, Philosophical Transactions of the Royal Society A: Mathematical, Physical and Engineering Sciences **369** (1948), 3150-3174 (2011).
8. S. Manipatruni, D. E. Nikonov and I. A. Young, Nature Physics **14** (4), 338-343 (2018).
9. S. Manipatruni, D. E. Nikonov, C.-C. Lin, T. A. Gosavi, H. Liu, B. Prasad, Y.-L. Huang, E. Bonturim, R. Ramesh and I. A. Young, Nature **565** (7737), 35-42 (2019).
10. N. F. Mott and R. H. Fowler, Proceedings of the Royal Society of London. Series A - Mathematical and Physical Sciences **153** (880), 699-717 (1936).
11. S. Maekawa and U. Gafvert, IEEE Transactions on Magnetics **18** (2), 707-708 (1982).
12. J. Nogués and I. K. Schuller, Journal of Magnetism and Magnetic Materials **192** (2), 203-232 (1999).
13. J. C. S. Kools, IEEE Transactions on Magnetics **32** (4), 3165-3184 (1996).
14. W. H. Meiklejohn and C. P. Bean, Physical Review **105** (3), 904-913 (1957).
15. H. Khurshid, W. Li, S. Chandra, M.-H. Phan, G. C. Hadjipanayis, P. Mukherjee and H. Srikanth, Nanoscale **5** (17), 7942-7952 (2013).

16. W. H. Meiklejohn, Journal of Applied Physics **33** (3), 1328-1335 (1962).
17. D. S. Geoghegan, P. G. McCormick and R. Street, Materials Science Forum **179-181**, 629-634 (1995).
18. G. C. Lavorato, E. Lima, H. E. Troiani, R. D. Zysler and E. L. Winkler, Nanoscale **9** (29), 10240-10247 (2017).
19. W. H. Meiklejohn and C. P. Bean, Physical Review **102** (5), 1413-1414 (1956).
20. M. N. Baibich, J. M. Broto, A. Fert, F. N. Van Dau, F. Petroff, P. Etienne, G. Creuzet, A. Friederich and J. Chazelas, Physical Review Letters **61** (21), 2472-2475 (1988).
21. G. Binasch, P. Grünberg, F. Saurenbach and W. Zinn, Physical Review B **39** (7), 4828-4830 (1989).
22. C. Binek, *Ising-type antiferromagnets : model systems in statistical physics and in the magnetism of exchange bias*. (Springer, Berlin ; New York, 2003).
23. M. Kiwi, Journal of Magnetism and Magnetic Materials **234** (3), 584-595 (2001).
24. M. Fiebig, Journal of Physics D: Applied Physics **38** (8), R123-R152 (2005).
25. J.-P. Rivera, Eur. Phys. J. B **71** (3), 299-313 (2009).
26. W. Kleemann and C. Binek, (2013), Vol. 442, pp. 163-187.
27. L. D. Landau and E. M. Lifshitz, *Electrodynamics of continuous media vol. 8*. (Pergamon Press, 1960).
28. R. R. Birss, Reports on Progress in Physics **26** (1), 307-360 (1963).
29. H. Schmid, International Journal of Magnetism **4** (4), 337-361 (1973).
30. I. E. Dzyaloshinskii, Journal of Experimental and Theoretical Physics **10** (3), 628-629 (1960).
31. A. D. N., JETP **40**, 1035-1041 (1961).
32. G. T. Rado and V. J. Folen, Physical Review Letters **7** (8), 310-311 (1961).
33. W. F. Brown, R. M. Hornreich and S. Shtrikman, Physical Review **168** (2), 574-577 (1968).
34. C. A. F. Vaz, Journal of Physics: Condensed Matter **24** (33), 333201 (2012).
35. J.-W. Lee, S.-C. Shin and S.-K. Kim, Applied Physics Letters **82** (15), 2458-2460 (2003).

36. S.-K. Kim, J.-W. Lee, S.-C. Shin, H. W. Song, C. H. Lee and K. No, Journal of Magnetism and Magnetic Materials **267** (1), 127-132 (2003).

37. X. He, Y. Wang, N. Wu, A. N. Caruso, E. Vescovo, K. D. Belashchenko, P. A. Dowben and C. Binek, Nature Materials **9**, 579 (2010).

38. K. D. Belashchenko, Physical Review Letters **105** (14), 147204 (2010).

39. A. F. Andreev, Journal of Experimental and Theoretical Physics Letters **63** (9), 758-762 (1996).

40. T. Martin and J. Anderson, IEEE Transactions on Magnetics **2** (3), 446-449 (1966).

41. G. T. Rado and V. J. Folen, Journal of Applied Physics **33** (3), 1126-1132 (1962).

42. N. Wu, X. He, A. L. Wysocki, U. Lanke, T. Komesu, K. D. Belashchenko, C. Binek and P. A. Dowben, Physical Review Letters **106** (8), 087202 (2011).

43. P. Appel, B. J. Shields, T. Kosub, N. Hedrich, R. Hübner, J. Faßbender, D. Makarov and P. Maletinsky, Nano Letters **19** (3), 1682-1687 (2019).

44. T. Kosub, M. Kopte, R. Hühne, P. Appel, B. Shields, P. Maletinsky, R. Hübner, M. O. Liedke, J. Fassbender, O. G. Schmidt and D. Makarov, Nature Communications **8**, 13985 (2017).

45. R. Schlitz, T. Kosub, A. Thomas, S. Fabretti, K. Nielsch, D. Makarov and S. T. B. Goennenwein, Applied Physics Letters **112** (13), 132401 (2018).

46. P. Borisov, A. Hochstrat, X. Chen, W. Kleemann and C. Binek, Physical Review Letters **94** (11), 117203 (2005).

47. T. Ashida, M. Oida, N. Shimomura, T. Nozaki, T. Shibata and M. Sahashi, Applied Physics Letters **106** (13), 132407 (2015).

48. K. Toyoki, Y. Shiratsuchi, A. Kobane, C. Mitsumata, Y. Kotani, T. Nakamura and R. Nakatani, Applied Physics Letters **106** (16), 162404 (2015).

49. P. A. Dowben, C. Binek, K. Zhang, L. Wang, W. Mei, J. P. Bird, U. Singisetti, X. Hong, K. L. Wang and D. Nikonov, IEEE Journal on Exploratory Solid-State Computational Devices and Circuits **4** (1), 1-9 (2018).

50. P. A. Dowben, C. Binek and D. Nikonov, presented at the 2018 International Symposium on VLSI Technology, Systems and Application (VLSI-TSA), 2018 (unpublished).

51. X. Chen, A. Hochstrat, P. Borisov and W. Kleemann, Applied Physics Letters **89** (20), 202508 (2006).

52. N. Sharma, A. Marshall, J. Bird and P. Dowben, presented at the 2015 IEEE Dallas Circuits and Systems Conference (DCAS), 2015 (unpublished).
53. N. Sharma, A. Marshall, J. Bird and P. Dowben, presented at the 2015 Fourth Berkeley Symposium on Energy Efficient Electronic Systems (E3S), 2015 (unpublished).
54. N. Sharma, J. Bird, P. Dowben and A. Marshall, presented at the 2017 30th IEEE International System-on-Chip Conference (SOCC), 2017 (unpublished).
55. W. Kern and D. A. Puotinen, RCA Review **31** (2) (1970).
56. W. Kern, Journal of the Electrochemical Society **137** (6) (1990).
57. M. Itano, F. W. Kern, M. Miyashita and T. Ohmi, IEEE Transactions on Semiconductor Manufacturing **6** (3), 258-267 (1993).
58. D. Zhang, Y. Wang and Y. Gan, Applied Surface Science **274**, 405-417 (2013).
59. J. G. Chu and Z. Y. Hua, Journal of Vacuum Science and Technology **20** (4), 1101-1104 (1982).
60. E. Morishita, Y. Kitora, T. Suganarni, S. Yamamoto and M. Nishids, International compressor Engineering Conference (1988).
61. L. D. Hall, Review of Scientific Instruments **29** (5), 367-370 (1958).
62. L. Y. L. Shen, Review of Scientific Instruments **43** (9), 1301-1306 (1972).
63. R. T. Bayard and D. Alpert, Review of Scientific Instruments **21** (6), 571-572 (1950).
64. D. Alpert, Journal of Applied Physics **24** (7), 860-876 (1953).
65. S. R. Systems, Operating manual and Programming Reference: Models RGA100, RGA200, and RGA300 Residual Gas Analyzer, 2009, accessed on November 11, 2019, https://www.thinksrs.com/downloads/pdfs/manuals/RGAm.pdf
66. B. A. Joyce, Reports on Progress in Physics **48** (12), 1637-1697 (1985).
67. R. F. Hampson and R. F. Walker, Journal of Research of the National Bureau of Standards-A. Physics and Chemistry **66A** (2) (1962).
68. R. K. Singh and J. Narayan, Physical Review B **41** (13), 8843-8859 (1990).
69. J. C. S. Kools, T. S. Baller, S. T. D. Zwart and J. Dieleman, Journal of Applied Physics **71** (9), 4547-4556 (1992).
70. I. W. Boyd, Ceramics International **22** (5), 429-434 (1996).
71. J. Schou, Applied Surface Science **255** (10), 5191-5198 (2009).

72. A. Caruso and R. Gratton, Plasma Physics **10** (9), 867-877 (1968).
73. J. A. Greer and M. D. Tabat, Journal of Vacuum Science & Technology A **13** (3), 1175-1181 (1995).
74. J. A. Greer, in *Pulsed Laser Deposition of Thin Films*, edited by R. Eason (2006), pp. 191-213.
75. J. A. Greer, M. D. Tabat and C. Lu, Nuclear Instruments and Methods in Physics Research Section B: Beam Interactions with Materials and Atoms **121** (1), 357-362 (1997).
76. Y. G. Kim, P. A. Dowben, J. T. Spencer and G. O. Ramseyer, Journal of Vacuum Science & Technology A **7** (4), 2796-2799 (1989).
77. P. J. Chen, M. L. Colaianni and J. T. Y. Jr., Journal of Applied Physics **72** (7), 3155-3160 (1992).
78. D. Depla, S. Mahieu and J. E. Greene, in *Handbook of Deposition Technologies for Films and Coatings (Third Edition)*, edited by P. M. Martin (William Andrew Publishing, Boston, 2010), pp. 253-296.
79. F. M. Penning, United States Patent No. 2,146,025 (1936).
80. P. J. Kelly and R. D. Arnell, Vacuum **56** (3), 159-172 (2000).
81. J. Kerr, The London, Edinburgh, and Dublin Philosophical Magazine and Journal of Science **3** (19), 321-343 (1877).
82. M. Heidkamp and J. L. Erskine, Review of Scientific Instruments **71** (8), 3141-3147 (2000).
83. E. Beaurepaire, J. C. Merle, A. Daunois and J. Y. Bigot, Physical Review Letters **76** (22), 4250-4253 (1996).
84. U. Tiwari, R. Ghosh and P. Sen, Physical Review B **49** (3), 2159-2162 (1994).
85. M. N. Deeter and D. Sarid, IEEE Transactions on Magnetics **24** (6), 2470-2472 (1988).
86. Z. Q. Qiu and S. D. Bader, Journal of Magnetism and Magnetic Materials **200** (1), 664-678 (1999).
87. SRS, Model SR830 DSP Lock-In Amplifier, 2011, https://www.thinksrs.com/downloads/pdfs/manuals/SR830m.pdf
88. S. Polisetty, J. Scheffler, S. Sahoo, Y. Wang, T. Mukherjee, X. He and C. Binek, Review of Scientific Instruments **79** (5), 055107 (2008).
89. J. C. Gallop and B. W. Petley, Journal of Physics E: Scientific Instruments **9** (6), 417-429 (1976).
90. L. N. Cooper, Physical Review **104** (4), 1189-1190 (1956).
91. R. P. Feynman, R. B. Leighton and M. L. Sands, *The Feynman lectures on physics*. (Addison-Wesley Pub. Co., Reading, Mass, 1963).
92. B. D. Josephson, Physics Letters **1** (7), 251-253 (1962).

93. J. M. Rowell, Physical Review Letters **11** (5), 200-202 (1963).

94. R. C. Jaklevic, J. Lambe, A. H. Silver and J. E. Mercereau, Physical Review Letters **12** (7), 159-160 (1964).

95. Q. Design, *MPMS Hardware Reference Manual*, 1996,

96. N. W. Ashcroft and N. D. Mermin, *Solid State Physics*. (Harcourt College Publishers, 1976).

97. A. A. Bunaciu, E. g. Udriştioiu and H. Y. Aboul-Enein, Critical Reviews in Analytical Chemistry **45** (4), 289-299 (2015).

98. A. Gibaud and S. Hazra, Current Science **78** (12), 1467-1477 (2000).

99. A. Gibaud, M. S. Chebil and T. Beuvier, in *Surface Science Techniques*, edited by G. Bracco and B. Holst (Springer Berlin Heidelberg, Berlin, Heidelberg, 2013), pp. 191-216.

100. J. E. Mahan, K. M. Geib, G. Y. Robinson and R. G. Long, Journal of Vacuum Science & Technology A **8** (5), 3692-3700 (1990).

101. M. A. Herman and H. Sitter, in *Molecular Beam Epitaxy: Fundamentals and Current Status*, edited by M. A. Herman and H. Sitter (Springer Berlin Heidelberg, Berlin, Heidelberg, 1989), pp. 120-158.

102. T. Wagner, G. Richter and M. Rühle, Journal of Applied Physics **89** (5), 2606-2612 (2001).

103. A. D. Polli, T. Wagner, T. Gemming and M. Rühle, Surface Science **448** (2), 279-289 (2000).

104. E. H. Hall, American Journal of Mathematics **2** (3), 287-292 (1879).

105. H. Heidari, E. Bonizzoni, U. Gatti and F. Maloberti, IEEE Transactions on Circuits and Systems I: Regular Papers **62** (5), 1270-1278 (2015).

106. H. Blanchard, F. De Montmollin, J. Hubin and R. S. Popovic, Sensors and Actuators A: Physical **82** (1), 144-148 (2000).

107. P. Daniil and E. Cohen, Journal of Applied Physics **53** (11), 8257-8259 (1982).

108. T. Kosub, M. Kopte, F. Radu, O. G. Schmidt and D. Makarov, Physical Review Letters **115** (9), 097201 (2015).

109. D. Ruzmetov, D. Heiman, B. B. Claflin, V. Narayanamurti and S. Ramanathan, Physical Review B **79** (15), 153107 (2009).

110. W. N. Kang, C. U. Jung, K. H. P. Kim, M.-S. Park, S. Y. Lee, H.-J. Kim, E.-M. Choi, K. H. Kim, M.-S. Kim and S.-I. Lee, Applied Physics Letters **79** (7), 982-984 (2001).

111. O. Bierwagen, R. Pomraenke, S. Eilers and W. T. Masselink, Physical Review B **70** (16), 165307 (2004).

112. K. v. Klitzing, G. Dorda and M. Pepper, Physical Review Letters **45** (6), 494-497 (1980).

113. J. Lindemuth, *Hall Effect Measurement Handbook*. (Lake Shore Cryotronics, Inc., 2020).

114. J.-L. Wang, W. Echtenkamp, A. Mahmood and C. Binek, Journal of Magnetism and Magnetic Materials **486**, 165262 (2019).

115. Y. Ji, J. Miao, Y. M. Zhu, K. K. Meng, X. G. Xu, J. K. Chen, Y. Wu and Y. Jiang, Applied Physics Letters **112** (23), 232404 (2018).

116. L. Fallarino, A. Berger and C. Binek, Applied Physics Letters **104** (2), 022403 (2014).

117. W. Echtenkamp and C. Binek, Physical Review Letters **111** (18), 187204 (2013).

118. L. Landau, Nature **138** (3498), 840-841 (1936).

119. L. D. Landau and E. M. Lifshitz, in *Statistical Physics (Third Edition)*, edited by L. D. Landau and E. M. Lifshitz (Butterworth-Heinemann, Oxford, 1980), pp. 446-516.

120. T. Ashida, M. Oida, N. Shimomura, T. Nozaki, T. Shibata and M. Sahashi, Applied Physics Letters **104** (15), 152409 (2014).

121. C. Shi, M. Street, W. Junlei, W. Jian, Z. Xiaozhe, B. Ch and P. A. Dowben, Journal of Physics: Condensed Matter **29** (10), 10LT01 (2017).

122. T. Nozaki, M. Al-Mahdawi, S. P. Pati, S. Ye, Y. Shiokawa and M. Sahashi, Japanese Journal of Applied Physics **56** (7), 070302 (2017).

123. T. H. O'Dell, The Philosophical Magazine: A Journal of Theoretical Experimental and Applied Physics **7** (82), 1653-1669 (1962).

124. C. Binek, Physical Review B **70** (1), 014421 (2004).

125. K. Zhang, T. Zhao and H. Fujiwara, Journal of Applied Physics **91** (10), 6902-6904 (2002).

126. K. Zhang, T. Zhao and H. Fujiwara, Journal of Applied Physics **89** (11), 6910-6912 (2001).

127. C. Schlenker, S. S. P. Parkin, J. C. Scott and K. Howard, Journal of Magnetism and Magnetic Materials **54-57**, 801-802 (1986).

128. C. Binek, S. Polisetty, X. He and A. Berger, Physical Review Letters **96** (6), 067201 (2006).

129. S. Polisetty, S. Sahoo, A. Berger and C. Binek, Physical Review B **78** (18), 184426 (2008).

130. P. Borisov, A. Hochstrat, X. Chen and W. Kleemann, Phase Transitions **79** (12), 1123-1133 (2006).

131. W. Echtenkamp, M. Street, A. Mahmood and C. Binek, Physical Review Applied **7** (3), 034015 (2017).

132. E. E. Fullerton, J. S. Jiang and S. D. Bader, Journal of Magnetism and Magnetic Materials **200** (1), 392-404 (1999).
133. T. Mukherjee, S. Sahoo, R. Skomski, D. J. Sellmyer and C. Binek, Physical Review B **79** (14), 144406 (2009).
134. P. Nordblad, Nature Materials **14**, 655 (2015).
135. V. Skumryev, S. Stoyanov, Y. Zhang, G. Hadjipanayis, D. Givord and J. Nogués, Nature **423** (6942), 850-853 (2003).
136. S. Parkin, J. Xin, C. Kaiser, A. Panchula, K. Roche and M. Samant, Proceedings of the IEEE **91** (5), 661-680 (2003).
137. S. Yu, F. Toshiaki, O. Hiroto, N. Hayato and N. Ryoichi, Applied Physics Express **3** (11), 113001 (2010).
138. S. Yu, T. Yuichiro, T. Kentaro, N. Yuuta, O. Satoshi, M. Chiharu and N. Ryoichi, Applied Physics Express **6** (12), 123004 (2013).
139. C. Binek, A. Hochstrat and W. Kleemann, Journal of Magnetism and Magnetic Materials **234** (2), 353-358 (2001).
140. S. P. Pati, M. Al-Mahdawi, S. Ye, Y. Shiokawa, T. Nozaki and M. Sahashi, Physical Review B **94** (22), 224417 (2016).
141. L. Wee, R. L. Stamps and R. E. Camley, Journal of Applied Physics **89** (11), 6913-6915 (2001).
142. J.-V. Kim and R. L. Stamps, Physical Review B **71** (9), 094405 (2005).
143. R. Ahmed and R. H. Victora, AIP Advances **7** (5), 055817 (2017).
144. O. G. Udalov and A. A. Fraerman, Journal of Magnetism and Magnetic Materials **514**, 167266 (2020).
145. R. Ahmed and R. H. Victora, Applied Physics Letters **112** (18), 182401 (2018).
146. K. D. Belashchenko, O. Tchernyshyov, A. A. Kovalev and O. A. Tretiakov, Applied Physics Letters **108** (13), 132403 (2016).
147. Y. Shiratsuchi, S. Watanabe, H. Yoshida, N. Kishida, R. Nakatani, Y. Kotani, K. Toyoki and T. Nakamura, Applied Physics Letters **113** (24), 242404 (2018).
148. M. Street, W. Echtenkamp, T. Komesu, S. Cao, P. A. Dowben and C. Binek, Applied Physics Letters **104** (22), 222402 (2014).
149. Y. Kota, H. Imamura and M. Sasaki, Applied Physics Express **6** (11), 113007 (2013).
150. D. Halley, N. Najjari, H. Majjad, L. Joly, P. Ohresser, F. Scheurer, C. Ulhaq-Bouillet, S. Berciaud, B. Doudin and Y. Henry, Nature Communications **5** (1), 3167 (2014).

151. U. Singh and S. Adenwalla, Nanotechnology **26** (25), 255707 (2015).

152. Y. Takagaki, E. Wiebicke, H. Kostial and K. H. Ploog, Nanotechnology **13** (1), 15-17 (2001).

153. A. A. Bukharaev, A. K. Zvezdin, A. P. Pyatakov and Y. K. Fetisov, Physics-Uspekhi **61** (12), 1175-1212 (2018).

154. S. Mu, A. L. Wysocki and K. D. Belashchenko, Physical Review B **87** (5), 054435 (2013).

155. S. Mu and K. D. Belashchenko, Physical Review Materials **3** (3), 034405 (2019).

156. X. Chen, X. Zhang, M. A. Koten, H. Chen, Z. Xiao, L. Zhang, J. E. Shield, P. A. Dowben and X. Hong, Advanced Materials **29** (31), 1701385 (2017).

157. C. Sun, M. Street, R. Jacobs, D. Morgan, P. M. Voyles and C. Binek, Microscopy and Microanalysis **23** (S1), 1584-1585 (2017).

158. S. Ye, Y. Shiokawa, S. P. Pati and M. Sahashi, ACS Applied Materials & Interfaces **12** (26), 29971-29978 (2020).

159. S. Sahoo and C. Binek, Philosophical Magazine Letters **87** (3-4), 259-268 (2007).

160. X. He, W. Echtenkamp and C. Binek, Ferroelectrics **426** (1), 81-89 (2012).

161. T. Komesu, C. Waldfried, H.-k. Jeong, D. Pappas, T. Rammer, M. Johnston, T. Gay and P. Dowben, *Apparatus for spin-polarized inverse photoemission and spin scattering*. (SPIE, 2000).

162. A. Mahmood, W. Echtenkamp, M. Street, J.-L. Wang, S. Cao, T. Komesu, P. A. Dowben, P. Buragohain, H. Lu, A. Gruverman, A. Parthasarathy, S. Rakheja and C. Binek, Nature Communications **12** (1), 1674 (2021).

163. C. Binek, A. Hochstrat, X. Chen, P. Borisov, W. Kleemann and B. Doudin, Journal of Applied Physics **97** (10), 10C514 (2005).

164. B. Tudu, K. Tian and A. Tiwari, Sensors (Basel) **17** (12), 2743 (2017).

165. M. Testa-Anta, B. Rivas-Murias and V. Salgueiriño, Advanced Functional Materials **29** (36), 1900030 (2019).

166. J. Fischer, O. Gomonay, R. Schlitz, K. Ganzhorn, N. Vlietstra, M. Althammer, H. Huebl, M. Opel, R. Gross, S. T. B. Goennenwein and S. Geprägs, Physical Review B **97** (1), 014417 (2018).

167. M. Althammer, S. Meyer, H. Nakayama, M. Schreier, S. Altmannshofer, M. Weiler, H. Huebl, S. Geprägs, M. Opel, R. Gross, D. Meier, C. Klewe, T. Kuschel, J.-M. Schmalhorst, G. Reiss, L. Shen, A. Gupta,

Y.-T. Chen, G. E. W. Bauer, E. Saitoh and S. T. B. Goennenwein, Physical Review B **87** (22), 224401 (2013).
168. T. Shimizu, T. Yokouchi, T. Oikawa, T. Shiraishi, T. Kiguchi, A. Akama, T. J. Konno, A. Gruverman and H. Funakubo, Applied Physics Letters **106** (11), 112904 (2015).
169. D. Lee, H. Lu, Y. Gu, S.-Y. Choi, S.-D. Li, S. Ryu, T. R. Paudel, K. Song, E. Mikheev, S. Lee, S. Stemmer, D. A. Tenne, S. H. Oh, E. Y. Tsymbal, X. Wu, L.-Q. Chen, A. Gruverman and C. B. Eom, Science **349** (6254), 1314-1317 (2015).
170. I. Stolichnov, M. Cavalieri, E. Colla, T. Schenk, T. Mittmann, T. Mikolajick, U. Schroeder and A. M. Ionescu, ACS Applied Materials & Interfaces **10** (36), 30514-30521 (2018).
171. L. Collins, Y. Liu, O. S. Ovchinnikova and R. Proksch, ACS Nano **13** (7), 8055-8066 (2019).
172. V. V. Shvartsman, B. Dkhil and A. L. Kholkin, Annual Review of Materials Research **43** (1), 423-449 (2013).
173. S. Mukherjee, B. M. Andersen, Z. Viskadourakis, I. Radulov and C. Panagopoulos, Physical Review B **85** (14), 140405 (2012).
174. J. M. D. Coey, *Magnetism and Magnetic Materials*. (Cambridge University Press, Cambridge, 2010).
175. S. Foner and M. Hanabusa, Journal of Applied Physics **34** (4), 1246-1247 (1963).
176. C. Kittel, *Introduction to solid state physics*, 8th ed. (John Wiley & Sons, United States of America, 2004).
177. H. Wiegelmann, A. G. M. Jansen, P. Wyder, J. P. Rivera and H. Schmid, Ferroelectrics **162** (1), 141-146 (1994).
178. L. M. Holmes and L. G. Van Uitert, Solid State Communications **10** (9), 853-857 (1972).
179. J. Íñiguez, Physical Review Letters **101** (11), 117201 (2008).
180. G. T. Rado, Physical Review **128** (6), 2546-2556 (1962).
181. R. Hornreich and S. Shtrikman, Physical Review **161** (2), 506-512 (1967).